

NASA CR-120974



(NASA-CR-120974) STUDIES OF OSCILLATORY
COMBUSTION AND FUEL VAPORIZATION Final
Report G.L. Borman, et al (Wisconsin
Univ.) Aug. 1972 99 p

N73-11971

CSCL 21B

G3/33

Unclas
47391

CONTRACTOR REPORT

STUDIES OF OSCILLATORY COMBUSTION AND FUEL VAPORIZATION, FINAL REPORT

by

G. L. Borman, P. S. Myers and O. A. Uyehara



prepared by

NATIONAL AERONAUTICS AND SPACE ADMINISTRATION

August 1972

NASA Grant NGR 50-002-017

Technical Management
NASA Lewis Research Center
Cleveland, Ohio
Chemistry and Energy Conversion Division
Paul R. Wieber

UNIVERSITY OF WISCONSIN
DEPARTMENT OF MECHANICAL ENGINEERING
Madison, Wisconsin

CONTRACTOR REPORT

STUDIES OF OSCILLATORY COMBUSTION
AND FUEL VAPORIZATION, FINAL REPORT

by

G. L. Borman, P. S. Myers and O. A. Uyehara

prepared by

NATIONAL AERONAUTICS AND SPACE ADMINISTRATION

August 1972

NASA Grant NGR 50-002-017

Technical Management

NASA Lewis Research Center

Cleveland, Ohio

Chemistry and Energy Conversion Division

Paul R. Wieber

THE UNIVERSITY OF WISCONSIN
Department of Mechanical Engineering
Madison, Wisconsin

STUDIES OF OSCILLATORY COMBUSTION AND
FUEL VAPORIZATION, FINAL REPORT

BY G. L. BORMAN, P. S. MYERS O. A. UYEHARA

ABSTRACT

A summary of the projects and research results carried out under the grant is given along with an interpretation of the results for applications purposes. Projects reported are: comparisons of experimental and theoretical droplet vaporization histories under ambient conditions such that the droplet may approach its thermodynamic critical point, experimental data on instantaneous heat transfer from a gas to a solid surface under conditions of oscillatory pressure with comparisons to an unsteady one-dimensional model, and droplet size and velocity distribution in a spray as obtained by use of a double flash fluorescent method.

ACKNOWLEDGEMENTS

Although only the names of the principal investigators appear as authors on this final report, the major credit for the results reported must go to the following graduate students who carried out the research: L. D. Alexander, R. W. Goluba, J. F. Groeneweg, D. L. Juedes, J. A. Manrique, J. A. Ricart-Lowe, C. W. Savery, R. E. Sowls, D. W. Wendland. Acknowledgement is also given to the Wisconsin Alumni Research Foundation (WARF) for support in the form of fellowships and computer services.

TABLE OF CONTENTS

	Page
Abstract	i
Acknowledgements	ii
Table of Contents	iii
List of Figures	iv
Nomenclature	vii
Summary	1
Introduction.	2
Droplet Vaporization	5
Unsteady Heat Transfer	19
Distributions in Sprays	27
Summary of Conclusions	32
Applications of Results	36
Reference List	39
Distribution List	80

LIST OF FIGURES

- Figure 1 Calculated vapor-liquid equilibrium isotherms for the carbon dioxide-nitrogen system. (C = critical point of CO₂)
- Figure 2 Pressure-molar volume diagram for the carbon dioxide-nitrogen system at $T/T_{cA} = 0.90$
- Figure 3 Isothermal difference in the partial molal enthalpies of carbon dioxide as a function of total pressure
- Figure 4 Vaporization history of a CO₂ droplet vaporizing in N₂ at 1400°K and 72.9 atmospheres
- Figure 5 Temperature response of a CO₂ droplet vaporizing in N₂ at 1184°K and 112 atmospheres
- Figure 6 Mass vaporization rate and percent-mass-vaporized curves for the same conditions as shown on Figure 5
- Figure 7 Effect of frequency upon the mass vaporization rate
- Figure 8 Response of a CO₂ droplet vaporizing in N₂
- Figure 9 Cross-section of Probe Subassembly for SDA
- Figure 10 Schematic diagram of the falling drop apparatus
- Figure 11 Summary of Freon-13 temperature data for various pressures
- Figure 12 Summary of Freon-13 temperature data, shown vs. pressure for air temperature of 250°F (394°K)
- Figure 13 History of Freon-13 drop vaporizing in air at $1.25 P_c$ and 350°K
- Figure 14 Steady state temperature versus air temperature for CO₂ at two pressures
- Figure 15 Percent-mass-transferred and droplet temperature histories for CO₂ and $0.75 P_c$ and 349°K air
- Figure 16 Gas phase mole fractions for CO₂ and Freon-13 in air versus temperature for various pressures
- Figure 17 Experimental steady state droplet temperatures from the period of oscillation of droplets falling through helium
- Figure 18 Experimental steady state droplet temperatures obtained from the period of oscillation of carbon dioxide droplets falling through helium

- Figure 19 Steady state droplet temperatures calculated from the film theory for .05 cm diameter carbon dioxide droplets falling through helium at a velocity of 120 cm/sec.
- Figure 20 Schematic diagram of experimental apparatus for the PST
- Figure 21 Test section instrumentation for PST
- Figure 22 Pressure shapes at various locations in the tube near the test plate end - X distance measured in inches from the test plate
- Figure 23 Experimental pressure versus crankangle for various cycles of CPD
- Figure 24 Experimental bulk gas temperature for various cycles of CPD
- Figure 25 Variation of wall surface temperature above the base temperature of 276°F versus crankangle for various cycles of the CPD
- Figure 26 Experimental surface temperature and heat flux histories for various cyclic speeds of the CPD
- Figure 27 Experimental gas pressure oscillations PST
- Figure 28 Experimental surface temperature oscillations PST
- Figure 29 Experimental heat flux variation PST
- Figure 30 Gas temperature profiles during the compression stroke of the CPD at 400 RPM
- Figure 31 Gas temperature profiles during the expansion stroke of the CPD at 4000 RPM
- Figure 32 Predicted gas temperature profiles for the PST. Shock arrives at $\tau = 0$
- Figure 33 Positive heat transferred per cycle at three different tube mass flow rates of the PST
- Figure 34 Experimental arrangement for double-exposure fluorescent photography.
- Figure 35 Ideal timing criteria for double exposure photography
- Figure 36 Sampling geometry for spray photography
- Figure 37 Schematic formation-propagation characteristics of mass density functions with no vaporization. Injection into a lower velocity, gas, $v_E > u$

Figure 38 Schematic formation-propagation characteristics of mass density functions with no vaporization. Injection into a higher velocity gas, $v_E < u$

NOMENCLATURE

cmolar density
c_pspecific heat at constant pressure
c_{pi}molar specific heat of component i
Ddroplet diameter
D_{AB}binary diffusivity
\bar{H}_ipartial molal enthalpy of component i
kthermal conductivity
m_ddroplet mass
N_imolar flux of component i with respect to stationary coordinates
P_ccritical pressure
P, ppressure
Rgas constant
rradial distance
r_odroplet radius
Ttemperature
T_ccritical temperature
ttime
ugas velocity in x direction
v_Eliquid velocity at nozzle exit
V_{mO}molar average velocity
wmolar vaporization rate
xdistance coordinate
x_imole fraction of component i
γratio of specific heats
Γ_irandom variable
λperiod of oscillation
ρdensity
ρ_gdensity of gas phase
ρ_ldensity of liquid phase
Superscripts	
lliquid phase
vvapor phase

Abbreviations

CPD.....Cylinder Piston Device

FDA.....Falling Droplet Apparatus

PRG.....ambient pressure divided by vaporizing component critical pressure

PST.....Periodic Shock Tube

SDA.....Suspended Droplet Apparatus

TRG.....ambient temperature divided by vaporizing component critical temperature

TRL.....liquid temperature divided by critical temperature of pure vaporizing component

STUDIES OF OSCILLATORY COMBUSTION AND FUEL VAPORIZATION

FINAL REPORT

BY

G. L. Borman, P. S. Myers, O. A. Uyehara

The University of Wisconsin

SUMMARY

The three areas of research studied were: single droplet vaporization under ambient conditions such that the droplet liquid may approach its thermodynamic critical point, heat transfer from a gas to a solid surface under conditions of oscillating pressure and droplet size and velocity distributions in sprays.

A spherically symmetric droplet vaporization model was constructed to include the effects of high ambient pressure and variable properties through the boundary layer. Calculations using the model were made for carbon dioxide vaporizing in a nitrogen gas atmosphere. The calculations were compared to the results from film theory and to calculations using mean properties and low pressure approximations. Major results show that the effects of high pressure on properties cannot be neglected. Film theory properties must in particular be corrected for the effect of pressure on vapor pressure and heat of vaporization. For any given ambient pressure above the critical the model predicts an ambient temperature above which the entire droplet history will be unsteady.

Experiments were conducted to measure the size and temperature histories of liquid-heptane, Freon-13 and carbon dioxide droplets suspended in a flowing stream of high pressure heated air. Experimental histories were compared to film theory calculations with mean film properties corrected for pressure. Comparisons show reasonable agreement between calculated and experimental steady state droplet temperatures, but calculated mass transfer rates were 30 to 50% lower than the experimental values.

Experiments were conducted to measure size and position histories of droplets falling in a stagnant high pressure, high temperature inert gas. Most data was taken for carbon dioxide droplets falling in helium gas. Droplet temperatures were estimated from experimental values of the period of vibration of the droplet. Observed regimes of droplet break-up and droplet shedding indicate that for supercritical pressures increasing gas temperature causes droplets to reach a point where droplet break-up seems related to the surface layer reaching the critical mixing temperature.

Experimental measurements of the instantaneous heat transfer at a solid surface exposed to a gas undergoing pressure oscillations were performed and comparisons were made with calculations using a one-dimensional energy equation for the gas. Large amplitude, low frequency (15 to 58 Hz) sinusoidal type oscillations were produced by a piston-cylinder device. The effects of repetitive (500 to 800 shocks per second) shock waves impinging on the end wall of a tube were investigated by use of a siren shock wave generator. Results show that rate-of-change of pressure is an important parameter in determining heat transfer under the conditions studied. It is also shown that the mechanism of turbulence is very important in determining net heat flux, but that laminar models may be used to predict phase relationships.

Droplet size and velocity distributions were experimentally measured in a spray by use of double-exposure fluorescent photography. Results show that droplet velocity in a spray is a statistically distributed variable the knowledge of which is equally important to droplet size distribution.

INTRODUCTION

Although all of the research conducted under the grant was related to the problem of understanding combustion in rockets, the phenomena investigated have been concerned with the physical aspects of the propellant spray rather than the chemical aspects of combustion itself. Motivation for this approach was provided by the attempts of Priem (1) and others to model the combustion chamber on the basis of droplet vaporization and combustion. In such models a detailed knowledge of the spray formation, droplet size distribution, droplet dynamics, droplet vaporization and droplet burning are required. Much of this information is lacking. In particular, droplet vaporization under ambient conditions of high pressure and temperature and droplet vaporization under conditions of large amplitude ambient pressure variations had not received detailed experimental study at the start of this grant.

Three areas of research were studied under the grant. The three areas are: single droplet vaporization under ambient conditions such that the droplet liquid may approach its thermodynamic critical point, heat transfer from a gas to a solid surface under conditions of oscillating pressure, and droplet size and velocity distribution in sprays. Although the oscillating pressure heat transfer study was conducted under conditions of zero mass transfer, it was felt the study would nevertheless provide a background for future investigations of vaporization subject to similar ambient conditions. The relationship of each of these projects to the state-of-the-art existent at the initiation of the grant

is given briefly below. More detailed literature reviews are given in the various reports which resulted from the grant research.

The problem of modeling a vaporizing and subsequently burning spray is of practical importance in many devices and has received a tremendous amount of serious study over the years. Such studies associated with spray modeling may be divided into three phases. First is the problem of understanding the formation of the spray, i.e., the atomization process. After initial breakup additional droplet formation processes may continue in the form of droplet collisions which may result in coalescence, and in the form of droplet shattering caused by interaction of the drops and the surrounding gas stream. The problem of droplet collisions is of minor importance in the usually dilute spray of rockets, turbines and oil burners. The problem of droplet shattering after the initial formation process is also relatively unimportant except for cases where shock or detonation waves are traveling through the spray (2). An exception may occur in sprays where some of the droplets heat up to their critical point. Under such conditions the vanishing of the surface tension at the critical point may cause additional breakup. The second phase of the spray modeling problem is that of spray propagation prior to combustion. To model this phase of the spray phenomena, models for droplet vaporization and droplet drag coefficients must be used. These models for single droplet behavior must be incorporated into a statistical description of the spray (3). The third phase of the spray modeling problem is that of droplet ignition and combustion. In addition to all of the phenomena which occur in the precombustion phase, we now have the complexities of chemical kinetics, flame spreading through premixed zones of fuel and oxidizer, single droplet burning models, and for fossil fuels the radiant heat flux created by the carbon particles in the diffusion flames. For purposes of relevance to the present research the subsequent discussion will be limited to the second phase of spray propagation without combustion.

In order to model the vaporization phase of the spray propagation, initial distribution data for droplet size and velocity should be available. Previous work tended to emphasize droplet size (mass) distributions without regard to the velocity distribution. In cases where droplet velocity was measured the data were interpreted on the supposition that drops of a given size all move with the same velocity at a given axial location. The general statistical formulations based on adaptation of statistical mechanics did not take any restrictive assumptions about the velocity distribution. However, applications of the theory reverted to simple assumptions because experimental data was lacking. Thus a clear need existed to establish a better understanding of the distribution functions which are necessary to initializing the propagation problem. Specific goals of the spray distribution research were: (I) to assess the physical justification for treating velocity as a random variable in a manner similar to drop size;

(II) to determine the implications of such a model for (a) interpretation of previous size measurements, (b) the design of future experiments, and (c) the analytical simulation of sprays; (III) to extend the statistical treatment to include droplet temperature as a random variable. In order to accomplish these goals it was necessary to devise an experimental method of simultaneously measuring size and velocity in a spray.

Given the initial distribution functions for a spray and the model equations properly formulated, it seems possible to calculate the subsequent behavior of the spray. To overcome the formidable numerical difficulties a third generation computer of high speed and large capacity would be required. Such calculations are, however, dependent on accurate models for single droplet vaporization and drag. Although experiments had established adequate theories for vaporization under conditions of atmospheric pressure (4) experimental verification of the models at high pressures had not been achieved. In particular, calculations based on low pressure theory (5) showed that droplets in rocket engines might reach the critical point of the liquid. Similar calculations also showed that critical point vaporization may occur in diesel engines. Because of the complicated nature of the droplet physical properties near the thermodynamic critical point, both a qualitative and quantitative description of vaporization in this region were lacking. The fact that surface tension approaches zero at the critical point also raised questions about the droplet dynamics in this region. Specific goals of the droplet critical point vaporization research were: (I) to investigate the theory of droplet vaporization in the critical region in order to (a) establish an appropriate model for the boundary conditions at the droplet surface, (b) establish the importance of property variations in the boundary layer under near critical conditions and (c) compare calculations based on a spherically symmetric, variable property boundary layer model with various film theories; (II) to experimentally obtain droplet temperature and size histories under conditions where the droplet might be expected to reach its critical point and to compare such histories with film theory calculations; (III) to experimentally obtain droplet size and velocity histories under conditions of high ambient temperature and pressure in order to establish drag coefficients or possible breakup behavior in the critical region.

In addition to modeling steady-state spray vaporization, models of a similar nature have been used to investigate the phenomena of oscillatory combustion (6). In such models the effects of pressure waves on droplet vaporization are of prime importance. In particular, the phasing between the pressure wave and the instantaneous mass and heat transfer to the drop may provide a key to instability (7). Because of the complicated nature of this problem, it was felt that experiments might well begin with heat transfer in the absence of mass transfer in order to establish a qualitative understanding of the effects of large pressure oscillations on the thermal boundary layer. Previous experimental studies in reciprocating engines had already established anomalous

phase behavior between heat flux and bulk gas temperature (8). Available experimental studies of heat transfer to the side walls of a tube through which periodic shock waves were traveling (9) had shown very complicated phenomena due to flow reversals and turbulence in the boundary layer. Thus the geometry used for the research here was chosen to correspond to stagnation point flow in the hope that a one-dimensional unsteady heat transfer model could be used to analytically correlate the experimental data. The specific goals of the research on the effects of pressure oscillations on heat transfer were: (I) to experimentally obtain instantaneous rates of heat transfer at a solid surface under conditions of, (a) large pressure ratio sinusoidal type gas pressure oscillations, (b) high frequency repetitions of shock waves in the gas; (II) to establish a theoretical model which would explain the boundary layer phenomena under the experimental conditions and provide a foundation for future studies of vaporization under similar conditions. In addition to these goals it was felt that theoretical calculations of the effects of pressure variations on mass transfer using the spherically symmetric critical point model would be helpful in planning future work and in interpreting the usefulness of the previous film theory calculations.

In the following body of the report each of the areas of research conducted under the grant are detailed in individual sections. Each of these sections gives a brief description of the experiment and/or theory and the major conclusions. Readers interested in details of the methods and results are directed to the individually cited reports. Because the main thrust of the research was concerned with the critical point vaporization phenomena, this research is presented first. Following sections outline the heat transfer research and spray distribution research in turn. Two final sections then reiterate the major conclusions resulting from the grant studies and give an interpretation of these conclusions in terms of applications. Readers interested in only an overall view of the results may wish to read only these last two sections.

DROPLET VAPORIZATION

Two experimental and one theoretical project dealing with the vaporization of droplets under high pressure ambient conditions were conducted under the grant. In the theoretical project (10) a model was formulated for the spherically symmetric vaporization of a droplet under conditions where the ambient pressure may exceed the thermodynamic critical pressure of the droplet liquid. Calculations were carried out using this model for the case of stationary liquid carbon dioxide droplets vaporizing in nitrogen gas. In the first of the experimental studies (11,12) a droplet was suspended on a thermocouple bead and subjected to an upward flow of heated high pressure air. Experimental liquid temperature and mass histories for n-heptane, Freon-13

and carbon dioxide were compared with histories computed from film theory equations. In the second experimental study (13) liquid droplets were allowed to fall through a high temperature, high pressure stagnant gas. Droplet position and size were measured as a function of time. Most of the data collected were for carbon dioxide droplets falling in helium or nitrogen gas.

In the following section the basic theory and results for the theoretical work are reviewed followed by a description of the experimental methods and results. The final section compares the theoretical and experimental results.

Boundary Layer Model

In order to determine the importance of physical property variations at high pressures and to formulate the proper boundary conditions for droplets at near critical conditions a spherically symmetric vaporization model was hypothesized. This means that gravitational and hydrodynamical effects were neglected. The entire liquid droplet was assumed to be at a uniform temperature. Chemical reactions, viscous dissipations, radiant energy exchange, and the Dufour energy flux were also neglected. With these assumptions the properties in the liquid are functions of radial distance and time.

The most general problem posed was that of unsteady vaporization where the ambient pressure and temperature varied with time in some prescribed manner. The total pressure was assumed to vary only with time and not distance. The governing equations for the boundary layer which extends from the droplet surface to infinity are then as follows. Equation of continuity of the vaporizing species A:

$$c \frac{\partial x_A}{\partial t} + c V_{MO} \frac{\partial x_A}{\partial r} = \frac{1}{r^2} \frac{\partial}{\partial r} \left(r^2 c D_{AB} \frac{\partial x_A}{\partial r} \right) \quad (1)$$

Equation of the continuity of the mixture:

$$\frac{\partial c}{\partial t} + \frac{1}{r^2} \frac{\partial}{\partial r} \left(r^2 c V_{MO} \right) = 0 \quad (2)$$

Equation of energy:

$$\begin{aligned} c x_A \frac{\partial \bar{H}_A}{\partial t} + c x_B \frac{\partial \bar{H}_B}{\partial t} + N_A \frac{\partial \bar{H}_A}{\partial r} + N_B \frac{\partial \bar{H}_B}{\partial r} \\ = \frac{1}{r^2} \frac{\partial}{\partial r} \left(r^2 k \frac{\partial T}{\partial r} + \frac{dP}{dt} \right) \end{aligned} \quad (3)$$

Equation of state:

$$c = c(x_A, P, T) \quad (4)$$

The molar fluxes of species A and B may be expressed in the form

$$c = c(T, P, x_A) \quad (5)$$

$$N_A = c_A V_{AO} = c x_A V_{MO} - c D_{AB} \frac{\partial x_A}{\partial r} \quad (6)$$

The partial molal enthalpy of each component \bar{H}_A and \bar{H}_B , the thermal conductivity of the mixture, k , and the binary diffusivity, D_{AB} , are taken as functions of temperature, pressure and composition. For the liquid droplet of radius $r_0(t)$, an energy and a mass balance give

$$4\pi r_0^2 k \left. \frac{\partial T}{\partial r} \right|_{r=r_0} = m_d C_{PA}^l \frac{dT^l}{dt} + w (\bar{H}_A^v - \bar{H}_A^l) \quad (7)$$

$$w = - 4\pi r_0^2 c_A^l \frac{dr_0}{dt} - \frac{4}{3}\pi r_0^3 \frac{dc_A^l}{dt} \quad (8)$$

$$w = \left\{ 4\pi r_0^2 c x_A \frac{dr_0}{dt} - \frac{c D_{AB}}{1 - x_A} \frac{\partial x_A}{\partial r} \right\}_{r=r_0} \quad (9)$$

The boundary conditions at $r=\infty$ are easily determined if one assumes that the ambient temperature, $T(\infty, t)$ is given and that the mole fraction of component A is zero at $r=\infty$. The temperature in the mixture at the droplet surface is taken equal to the droplet temperature $T^l(t)$. The boundary condition for determining $x_A(r_0, t)$ is more difficult to determine and requires some further assumptions. If we assume negligible departures from equilibrium at the surface the mole fraction, X_A , may be calculated as a function of T^l and P from vapor-liquid equilibrium relationship. At low total pressures x_A may be approximated by use of the vapor pressure of pure component A. At high pressures, however, a significant amount of species B may be dissolved in liquid A, thus causing large departures from the pure component vapor pressure. Even if a fictitious state is assumed for which no B is absorbed in liquid A, the total pressure will cause x_A to differ from the mole fraction calculated from the ratio of vapor pressure to total pressure. If complete equilibrium absorption is assumed a second question arises concerning the diffusion of B in the liquid droplet system. Calculation of the gradients of concentration of B in liquid A would require appropriate diffusion concentrations

(which are unavailable) and a knowledge of a liquid motion in the droplet.* If one assumes that the penetration of B into liquid A is confined to a very thin layer at the surface, then the droplet bulk properties may be assumed to be those of pure component A . The amount of B absorbed is approximately balanced by release of B into the vapor state as the droplet vaporizes. This hypothesis also allows one to assume that the velocity of B relative to the droplet surface is zero.

Calculation of the equilibrium mole fraction at the droplet surface was carried out by equating the vapor and liquid state fugacities of species A and B respectively. The fugacities were calculated using the Redlich-Kwong two parameter equation of state. Figure 1 shows mole fraction versus pressure for two isotherms of a carbon dioxide and nitrogen system. The dashed lines show the mole fraction predicted from the carbon dioxide vapor pressure. The most notable feature of Figure 1 are the points marked D and E . The lower side of the isotherm gives the mole fraction of carbon dioxide in the gas phase. The mole fraction first decreases and then increases with total pressure until the limiting point (D or E) is reached. Figure 2 is a pressure-molar volume diagram for the $T/T_{cA} = 0.90$ isotherm of Figure 1. As can be seen, the point E represents a critical point for the mixture. For pressures above that corresponding to point E , the two phases of the mixture cannot be distinguished. Critical points such as D and E will be called "critical mixing points" and the locus of such points on a temperature-pressure plot will be called the "critical mixing line".

Figure 3 is a plot of heat of vaporization, $(\bar{H}_A^v - H_A^l)$, for two isotherms of the mixture. The heat of vaporization is zero at the critical mixing points. Figure 3 also gives the latent heats of vaporization for pure carbon dioxide at the two temperatures. From these figures it can be understood that if a droplet reaches the critical mixing point by means of an unsteady vaporization process it will continue to heat up until the drop reaches the ambient temperature or is completely vaporized. Thus if the ambient pressure is higher than the critical mixing point pressure and the ambient temperature is sufficiently high to reduce the heat of vaporization, droplet histories will not exhibit a steady state vaporization regime.

Calculations for carbon dioxide droplets in nitrogen gas were performed by integrating the equations of change numerically. Three vaporization model regimes were investigated; a steady state model with surface regression neglected, an unsteady model with

* Although the present model assumes a totally quiescent environment, application to any real system entails the concept of a droplet moving relative to the ambient gas and subsequently liquid motion within the droplet. This is the implicit assumption used in taking T^l to be a function of time only.

constant ambient conditions, and an unsteady state model with ambient pressure and temperature varying sinusoidally. In addition, a few calculations were performed in which it was assumed that no nitrogen was absorbed in the liquid carbon dioxide.

In order to assess the effects of property variations with pressure, calculations were performed with and without correction for high pressure.

The major results of the steady state model calculations in addition to the general conclusions discussed above were:

- (1) The constant mean properties are used in the calculations the droplet temperature is unaffected but the vaporization rate is substantially higher (~35%) than for variable property calculations.
- (2) The assumption of unidirectional diffusion in the steady state becomes less valid as the ambient temperature is decreased and the total pressure is increased.
- (3) Use of simplified low pressure physical property assumptions for calculations at high pressures is not justified in view of the large effects of pressure on heat of vaporization and interface mole fraction (vapor pressure). At sufficiently high pressures the low pressure property assumptions can give two solutions or no solution indicating that these assumptions are unrealistic. At high pressures the low pressure model under predicts mass transfer rates at low ambient temperatures and over predicts them at higher ambient temperatures. The crossover point is about 800°K for a total pressure of 72.9 atmospheres.
- (4) If the assumption of equilibrium absorption at the liquid surface is replaced by one of insolubility of nitrogen in carbon dioxide the steady state droplet histories are not substantially modified. In general the effect is to increase the mole fraction of CO_2 in the vapor state at the droplet surface. The assumption of insolubility does however prevent the prediction of the point of transition between the two phases and single (indistinguishable) phase states.

Unsteady Calculations

The unsteady vaporization equations for the case of constant ambient temperature and pressure gave histories of droplet radius, mass and temperature as a function of time. The initial boundary layer profiles (time zero) were obtained by application of quasi-steady assumptions and artificially holding the droplet temperature constant at the initial value. Since the profiles quickly

revise themselves, the initial choice of profiles was not critical.

Two types of histories can be observed. If the droplet temperature reaches a steady-state temperature lower than the critical mixing point a history of the shape illustrated in Figure 4 results. If the critical mixing point is reached no steady state is possible and a history of the type shown in Figures 5 and 6 results. It should be noted that the rate of vaporization decreases as the critical mixing point is crossed.

The following conclusions may be drawn from the unsteady analysis:

- (1) The unsteady heating-up period is most important in the vaporization process of single droplets under high pressure environmental conditions. Furthermore, it is observed that the ratio of heating-up to steady-state periods is directly proportional to the ratio $(c_{pA}/k)^{1/2}$. Although the specific heat as well as the thermal conductivity of a pure substance increase with pressure, the specific heat increases much faster in the critical region than the thermal conductivity. Hence, the unsteady heating-up period is most important at high pressures.
- (2) A vaporizing droplet can indeed reach and exceed its thermodynamic critical temperature, thus becoming a dense mass of vapor, at supercritical pressures by an intrinsically unsteady process. Under high enough ambient temperatures and a supercritical pressure, a droplet very rapidly reaches its critical temperature.
- (3) Initial values for the mass vaporization rate are largely enhanced as the ambient temperature increases, for the same initial droplet conditions.
- (4) Inclusion of the effects associated with dense mixtures, the effect of total pressure on vapor pressure and enthalpy of vaporization, as well as the pressure effect upon the thermophysical properties, cannot be disregarded in high pressure vaporization analyses.
- (5) Large density variations are exhibited in a small radial distance surrounding a vaporizing droplet. Temperature and composition gradients in the vapor phase at the droplet surface are appreciable.
- (6) Slight departures from the square law dependence in the variation of the droplet's lifetime with radius were found.
- (7) Vaporization times may be estimated by the quasi-steady film theory of Reference 4 over a wide range of temperatures and pressures, provided the vapor pressure and enthalpy of

vaporization are properly corrected under high density conditions. Without corrections, the theory of the reference predicts too long vaporization times under high pressures and low ambient temperature conditions.

Unsteady Cyclical Calculations

A few calculations were performed in which the ambient pressure was varied sinusoidally. The ambient temperature was obtained by assuming an isentropic relationship between ambient temperature and pressure. Only very small pressure ratio fluctuations were assumed (pressure amplitudes of a few percent of the average pressure) and the variation in total pressure with distance was neglected. For the high frequencies of interest (>500 Hz) the variation in liquid temperature at the droplet surface can be shown to be negligible small. At low ambient temperatures ($\sim 400^\circ K$) and supercritical pressures, the pressure and mass vaporization oscillations were out-of-phase (negative response factor as defined by Reference 7). At higher temperatures, however, the mass transfer rate and pressure were found to be in phase as shown in Figure 7. Similar results were found for droplets vaporizing in the supercritical mixing point region as is shown in Figure 8. Not all results were this simple however, and cases were found in which the phase relationship progressed from in-phase to out-of-phase as the droplet heated up. The general conclusion can be drawn from the analysis that response factors may be positive at high pressure and frequency conditions, but that the situation is so complex that extensive calculations should be performed for a given liquid-gas system before drawing any specific conclusions.

Film Theories

The film theory vaporization equations used for calculations in Reference 14 neglect corrections for surface regressions and use mean film properties uncorrected for high pressure. From the theory discussed above it was found that at conditions of high ambient density a correction of the vapor pressure and latent heat for pressure effects would substantially improve the theory. Thus the experimental data obtained under the grant were compared with film theory equations with only these two properties corrected for pressure. In addition an approximate correction for surface regression was made.

Experimental Apparatus

Both experimental rigs were designed to study droplet vaporization at ambient pressures up to 100 atmospheres. The suspended drop apparatus (SDA) has an upper limit of air temperature

of about 300°F while the falling drop apparatus (FDA) can provide temperatures up to 1500°F but is limited to non-oxidizing ambient gases.

The SDA consists of an air heater, a test section with thermocouple probe and optical windows, a test liquid feed system, and a shadowgraph optical system. Details of the original design concepts are to be found in the thesis of Ricart-Lowe (16); the final system used is described in detail in Reference 11.

Basically, the air from a bank of high pressure bottles is regulated and flowed through the heater and through a one inch diameter nozzle designed to give a flat velocity profile. The nozzle is at the bottom of the test section housing which contains the probe and is provided with windows for viewing the probe tip. Upon exiting from the nozzle the heated air flows over the thermocouple probe, which supports the droplet, and exits at the top of the housing. The probe thermocouple bead is at the end of the thermocouple wires which extend back through a teflon tube which also carries the test liquid. Figure 9 shows a cross section of the probe subassembly. By regulating the flow of test liquid with a valve the test fluid could be made to flow down along the thermocouple wires and form a droplet on the thermocouple bead. A Shadowgraph image of the drop and bead with a magnification of 6x was formed on a ground glass and photographed with a 16 mm movie camera at 64 fps. Most of the data were obtained using 40 gauge (.003" diameter) constantan-chromel thermocouple wires with a 343 μ bead. Because of the low surface tension of liquids in the near critical region a teflon collar was added to the bead for most of the runs. The collar which helped to support the droplet consisted of a thin cylinder of teflon with about the same diameter as the thermocouple bead. This, plus upward air flow adjustment, prevented the droplet from falling off the thermocouple.

The FDA consists of a droplet forming and release device, an oven which provides the heated high pressure gas environment for the falling droplets, and an optical system for photographing the droplets during their passage through the oven. A schematic diagram is shown on Figure 10.

The drop forming device is a water cooled pressure vessel containing a vertically mounted hypodermic needle. Single droplets are formed by allowing liquid to accumulate on the needle tip until it becomes heavy enough to fall off. Groups of droplets can be formed by extruding a short jet of liquid which breaks up into a number of droplets. The droplet sizes so formed ranged from 0.2 to 0.8 mm diameter for liquid carbon dioxide in helium gas. After leaving the needle the droplet passes through a 1/4 inch diameter hole and enters the hot gas cavity of the oven.

The hot gas in the oven cavity consists of a one inch diameter by 3.25 inch long cavity with two diametrically opposed 1/4

inch wide fused quartz windows running along its length. The side wall of the cavity consists of a 1/2 inch thick layer of insulating material. This inner cavity is completely contained by a pressure vessel which has water cooled walls and a second set of vertical windows. The inner cavity is heated electrically. Figure 10 shows a schematic diagram of the apparatus.

A one to one image of the falling droplet is formed on the film of a drum camera by use of a strobotac light source. The apparatus was run to give 200 to 2000 pictures per second. Each film contained about 110 exposed frames.

Droplet size and position histories were determined by using a specially constructed projector. Droplet size measurements were made with a 175.9 magnification and position was measured by direct comparison with the image of an ellipse of variable size major axis and variable eccentricity. The major and minor axis dimensions of the ellipse which best fit each droplet outline were recorded.

Experimental Results

The experimental results obtained with the suspended droplet apparatus will be discussed first, followed by the results of the falling droplet apparatus. In both cases the results will be compared with film theory calculations.

The SDA was used to obtain about 90 n-heptane, 50 Freon-13 and 30 carbon dioxide droplet histories. The range of conditions for heptane (in terms of the critical properties of pure heptane $T_c = 772^\circ\text{R}$, $P_c = 27$ atmospheres) was: reduced pressures from 0.056 to 3.71, reduced liquid steady-state temperatures from 0.57 to 0.69. Reynolds numbers ranged from 150 to 600 for initial droplet diameters of 1275 to 2025 microns. The range of conditions for Freon-13 ($T_c = 544^\circ\text{R}$, $P_c = 38.2$ atmospheres) was: reduced pressures from 0.75 to 1.0 and reduced steady-state liquid temperatures from 0.79 to 0.95. Reynolds numbers ranged from 240 to 450 with initial droplet diameters from 980 to 1200 microns. The range of conditions for carbon dioxide ($T_c = 548^\circ\text{R}$, $P_c = 72.9$ atmospheres) was: reduced pressures of 0.75 and 1.0 and reduced steady-state liquid temperatures from 0.76 to 0.82. Reynolds numbers ranged from 140 to 350 for initial droplet diameters from 680 to 1150 microns. Typical runs allowed observation of droplet histories up to the 50 percent mass vaporized point. Estimates of experimental uncertainties using standard techniques for combining independent errors showed error limits of $\pm 7.5^\circ\text{C}$ in droplet temperature and $\pm 25\%$ in mass transfer rate resulting from uncertainties in measured values of temperature, flow pressure and drop size.

The experimental conditions for heptane correspond to low ambient gas temperature because the maximum air temperature of 300°F is less than critical temperature of pure n-heptane. Under

these conditions, film theory both corrected and uncorrected for high pressure gave steady-state droplet temperatures which agreed to within 5°F of the experimental values. Film theory corrected for high pressure predicted mass transfer rates to within ±25% of the measured values. The uncorrected theory gave similar accuracy up to 5 atm pressure, but at the highest pressure (100 atm) predicted mass transfer rates were 80% lower than the experimental values.

A summary of the Freon-13 experimental steady-state liquid temperatures is shown in Figure 11 which is a plot of liquid versus air temperatures for various pressures. The effect of pressure at 250°F air temperature is shown in Figure 12. Figure 12 also shows values of steady-state temperature computed with and without pressure-corrected properties. Computation over the entire range of data showed the high pressure theory to give temperatures 10 to 15°F lower than the experimental values. This lack of agreement was reflected in comparisons of experimental and Ranz-Marshall correlation Nusselt numbers. The correlation Nusselt numbers were about 30% below the experimental values.

Typical experimental and calculated percent mass transferred and temperature histories for Freon-13 are shown in Figure 13. The mass transfer rates predicted by the high pressure film theory were from 35 to 50 percent too low with the error increasing systematically with increasing pressure. The theory using low pressure property values gives errors approximately twice as large as the high pressure theory.

At reduced pressures above 1.5 the experimental droplet temperature histories gave increasingly shorter steady-state histories. Because the droplet histories could not be followed beyond the 50% mass vaporized point no firm conclusions can be drawn. However, comparison of the point of transition between histories with and without plateau temperatures showed that this transition point was very close to the calculated critical mixing point.

Figure 14 shows steady-state (plateau) temperatures for carbon dioxide droplets. The data for both pressures fall around the high pressure theory values exhibiting a maximum difference from the theory of ± 5°F. The low pressure theory lies above the experimental values. If the theory is calculated assuming no absorption of air in the liquid the resulting values fall below the experimental data.

Figure 15 shows a typical experimental and calculated histories for carbon dioxide. Again as in the case of Freon-13, the high pressure theory underestimated the rate of mass transfer by 30 to 40% with the better agreement being at the lower pressure. Some of the data show relatively good agreement in rate values at the steady-state conditions but all data show the calculations

underestimating the rates during the unsteady portion of the histories.

In comparing the calculated and experimental histories for all of the data it should be noted that the calculated value of the vapor mole fraction at the liquid surface is very critical. In particular, Freon-13 calculations were unsupported by experimental thermodynamic values and thus may be in error. A comparison of CO₂-air and Freon-13-air gas phase mole fractions are shown in Figure 16. Such an error in the calculated mole fraction could easily explain the larger disagreement in liquid temperatures for Freon-13. It is also possible that the assumption of equilibrium absorption at the liquid surface is incorrect. For example, it is not difficult to imagine that the assumption of no absorption may hold during the early (high mass transfer rate) part of the history while the equilibrium absorption assumption is essentially correct during the later portion of the history. In addition, it must be remembered that the spherically symmetric theoretical model solutions show that mean property values as used in the film theory can result in sizable differences in calculated mass transfer rates.

In conclusion, it should be pointed out that the above discussed data were taken at relatively low air temperatures. For higher ambient temperatures all of the properties used in the film theory should be corrected for high pressure effects.

Exploratory photographs using the falling drop apparatus (FDA) were taken at 200 frames per second of carbon dioxide droplets falling through argon, nitrogen and helium. Table 1 gives the ambient gas conditions for which these photographs were taken. The ambient gas pressure and temperature in Table 1 are divided by the respective critical properties of carbon dioxide. Photographs were not taken for argon and nitrogen at higher temperatures because convection currents in the oven interfered with the droplet images too strongly.

For the conditions in Table 1 where the gas symbol is given without an asterisk the photographs show the more normal case of material leaving a droplet's surface only as vapor. A careful examination of these photographs for droplets vaporizing in helium gives the following impressions. Most droplets are oscillating about some average shape which usually resembles a spheroid flattened in the direction of travel. For given ambient conditions the volume of liquid removed from a droplet depends strongly (almost linearly) on the volume of gas the droplet sweeps out in its passage. For given ambient conditions larger droplets fall faster and are more distorted. For a fixed ambient temperature droplets of a given size fall more slowly and are more distorted as the ambient pressure is increased. For a fixed ambient pressure droplets of a given size fall more rapidly and become slightly more distorted as the temperature is increased. For a fixed ambient density droplets of a given size fall slightly more slowly,

become slightly more distorted, and vaporize more rapidly as the ambient pressure and temperature are increased together.

At the conditions in Table 1 where the symbol for the gas carries an asterisk the photographs showed droplets which scattered or shed streamers or chunks of liquid or liquid-like material. Droplets which shed streamers or globules grow progressively smaller. Droplets which shatter usually appear to swell up, as if being blown up like a balloon, then break up into a number of smaller fragments. In some cases the discharge of liquid-like material seems to be continuous, in others it seems to have a nearly regular period, that of the oscillation of the droplet. The manner in which this material leaves a droplet suggests that the properties of the material near its surface are quite different than those of the material in its core. It seems likely that this variation in properties is due to differences in composition as well as differences in temperature.

At a given pressure the threshold for shedding from carbon dioxide droplets falling in nitrogen and argon is at a much lower ambient temperature than in helium. At a given pressure the critical mixing point also occurs at a much lower ambient temperature in the nitrogen-carbon dioxide and argon-carbon dioxide systems than in the helium-carbon dioxide systems. These observations appear compatible with the assumption that shedding occurs when the liquid near a droplet's surface approaches its critical mixing state.

Photographs taken at higher framing rates permitted an estimation of the droplet period of oscillation. Theoretically (17) the period of oscillation is related to droplet temperature by

$$\lambda \rho_l / (.25\pi D^{1.5}) = ((\rho_l + 2\rho_g/3)\sigma) \cdot^5 \quad (10)$$

where the period, λ , is related to the diameter, D , the liquid density, ρ_l , the vapor density, ρ_g , and the surface tension, σ .

To determine if the period could be used to calculate droplet temperature, tests were made by photographing droplets falling through a CO₂-He gas mixture for which the dew point temperature was equal to the droplet temperature while the dry bulb temperature was a little higher.

The results of these tests indicated that the period of oscillation is sufficiently independent of distortion and internal circulation to be useful for estimating droplet temperature and that the effect of helium on carbon dioxide surface tension is small for the conditions studied.

On the basis of available surface tension data for mixtures containing helium (18,19) it was assumed that for a given tempera-

TABLE 1
 AMBIENT CONDITIONS OF EXPLORATORY FDA PHOTOGRAPHS

PRG	<u>TRG</u>									
	1.00	1.25	1.50	1.75	2.00	2.50	3.00	3.50		
2.00	He	-	-	-	He*	He*	-	-	-	-
1.75	Ar*, N ₂ *, He	-	-	He	He	He*	He*	He*	He*	He*
1.50	Ar*, N ₂ *, He	-	He	-	He	-	-	-	He*	.
1.25	Ar, N ₂ , He	N ₂ , He	-	-	He	He	-	He	-	He
1.00	Ar, N ₂ , He	-	-	-	N ₂ , He	-	-	-	-	-
.875	-	-	-	He	He	-	-	-	-	-
.75	Ar, N ₂ , He	-	N ₂ , He	-	He	-	He	He	He	He
.625	-	N ₂ , He	-	-	He	He	-	He	-	-
.50	Ar, N ₂ , He	-	-	-	He	-	-	-	-	He

*Shows conditions for which droplet shedding or shattering occurred

ture the phase equilibrium values of surface tension for pure carbon dioxide (20) and He-CO₂ would be nearly the same.

Using 2000 frame per second data for CO₂ in He the average values of $\lambda/ (.25\pi D^{1.5})$ were determined for as many cycles of each droplet history as possible. These results are given in Figure 17 where additional analysis of the data indicates they are steady-state droplet temperatures. Most of these droplets were from 0.5 mm to 0.7 mm for the portions of their histories which were measured. For the droplets much smaller than 0.5 mm the amplitude of the oscillation was usually too small to measure reliably. Due to the very large amount of labor required each of these temperatures was determined from measurement of only a single droplet history. The evident scatter is attributed mostly to the effect of rotation on its apparent period of oscillation. A line is shown on Figure 17 that indicates conditions at the threshold for shedding. This threshold indicates the highest pressure for a given ambient temperature where histories will show a steady-state part.

Figure 18 is a plot of the experimental steady-state droplet temperature against reduced ambient temperature for lines of constant reduced pressure. Extrapolating the general trends of the data to a reduced liquid temperature of 1.0 produces the wiggly line on Figure 17. Interestingly, below this line droplets that were shedding vaporize more normally when they become small enough while above it they continue to disintegrate until they are gone. This indicates that below the line droplets reach a steady-state condition while above it they do not.

Steady-state temperatures were calculated for carbon dioxide droplets evaporating in a helium atmosphere according to the film theory presented by Savery, Juedes and Borman (12). The equations were solved for steady-state temperatures of 0.5 mm diameter droplets with a velocity of 120 cm/sec for all the ambient pressures and temperatures at which experimental droplet data was taken. Figure 19 shows the resulting values as liquid temperature versus ambient gas temperature for lines of constant pressure. Temperatures and pressures are reduced by dividing by the critical properties of carbon dioxide.

Property values for the film theory calculations were taken from published experimental values where possible. Equilibrium mole fractions (21) were used directly and also to calculate the partial molal enthalpy of CO₂ in the vapor phase. For all pressures used in the experiments and all liquid temperatures less than 290°K the calculated enthalpy of vaporization was smaller and less than 15% different than the latent heat of pure carbon dioxide. Reference 22 gives experimental values of density for both phases of the He-CO₂ equilibrium system. No experimental values for viscosity, thermal conductivity or diffusivity of He-CO₂ at high pressures were found. Because corresponding state theory was believed to be unreliable for the He-CO₂ combination, low pressure mixture values were used.

The droplet temperatures in Figures 18 and 19 for a given ambient condition show the same trends but differ by as much as 20°C between the two figures. Additional development of the experimental technique and better physical property values could reduce this difference considerably.

For a pressure lower than the critical pressure of carbon dioxide (< 72.87 atm, $PR < 1$) the steady-state droplet temperature isobar would be expected to asymptotically approach the corresponding vapor-liquid phase equilibrium temperature of pure carbon dioxide as the ambient temperature is increased indefinitely. Asymptotic behavior of the steady-state droplet temperature isobars is suggested in Figure 18 in spite of the evident scatter, and is quite apparent in Figure 19.

For a pressure equal to or greater than the critical pressure of carbon dioxide (≥ 72.87 atm, $PR \geq 1$) an upper limit of ambient temperature for which a droplet temperature history will show a steady-state part is expected (10,12). This upper limit should occur when the vapor-liquid interface just reaches its critical mixing point.

If a droplet approached its critical mixing point simultaneously throughout, its enthalpy of vaporization and surface tension would both become zero and, it would become a puff of dense gas. A droplet usually begins as a pure liquid at a lower temperature and is subject to aerodynamic drag forces. It cannot approach a critical mixing point simultaneously throughout since molecules from the gas phase and thermal energy must diffuse from its surface into its core. The tangential component of aerodynamic drag tends to move the surface material toward the rear of a droplet. If this surface material approaches its critical mixing point it detaches from the droplet because of its very small surface tension.

UNSTEADY HEAT TRANSFER

Two different experimental rigs were used to measure the instantaneous heat transfer at a solid surface which was exposed to a gas undergoing large amplitude pressure oscillations. In both cases the major component of gas velocity was normal to the solid surface and the heat flux was obtained by measuring the fluctuations in surface temperature of the solid wall. In the first rig (23) a piston and cylinder was used to generate the pressure oscillations. In the second rig (24) air flow was chopped by a siren to produce steep fronted pressure waves in a tube. The two experimental rigs are described below, followed by a summary of the experimental results and comparisons with theory.

Experimental Apparatus

The cylinder and piston apparatus consisted of a 2.3125 inch bore cylinder with a flat 0.5 inch thick cast iron head and flat

piston. The piston stroke was 1.5625 inches with a 10.06 compression ratio and a 4.42 inch connecting rod. Teflon piston rings and an oil free crankcase were used to prevent the problem of oil contamination of the cylinder gas. Frequencies of 15 to 58 Hz (915 to 3452 RPM) were obtained. The average pressure swing was about 365 psi. Because of blowby past the teflon rings it was necessary to supply a small amount of make-up air toward the end of each cycle. This was accomplished by drilling two 1/8 inch diameter holes in the sleeve and connecting them to a constant pressure air tank. The holes were uncovered by the piston at 38 crank degrees before BDC and remained uncovered until the piston covered them again on the upstroke.

The principle quantities measured were gas pressure, head surface temperature, gas temperature and driving frequency. The gas pressure was obtained by use of a piezoelectric pressure transducer located at the outer edge of the head. Driving frequency and piston crankangle position were measured by use of an Electromagnetic pickup excited by a set of grooves in the crankshaft flywheel. The cylinder side surface temperature of the cast iron head was measured by use of an iron-constantan Bendersky-type thermocouple. The junction was thus formed by a one micron thick constantan layer plated on the annular surface of the iron sheath. The temperature on the exterior side of the head was measured by forming a junction at the exterior surface directly above the thin film couple. In this way both the steady-state (time averaged) component of heat flux and the unsteady state flux could be measured simultaneously. The gas temperature was measured by use of a 3.81 micron diameter tungsten wire used as a resistance thermometer. The wire was from 1/8" to 5/8" long and supported so that it was parallel to the head and 3 mm from the head surface. At 3 mm from the head the wire was outside of the thermal boundary layer and thus measured a bulk gas temperature. At the high end of the frequency range (50 to 60 Hz) such resistance wire measurements apparently lag the gas temperature by a few crankangle degrees. It should be noted that in the above described device the major component of gas velocity is induced by the piston and should thus be perpendicular to the head surface. Other components of velocity were possible, however, because of flows induced by the make-up air flow and by leakage around the piston rings. In addition, thermal gradients could be induced by cold walls and by the action of the piston rings on the sleeve boundary layer. The effects of these three-dimensional flows could be expected to be minimum at the higher driving frequencies. In the experiments performed the swing in cylinder side surface temperature of the head was about 2°F per cycle while the temperature drop through the head was of the order of 200 to 300°F. The time average flux through the head was thus about 10^4 BTU/hr-ft² while the instantaneous peak heat flux at the inside surface was typically 5 to 10 times larger than the average heat flux.

Turning next to the shock tube experiment, Figure 20 shows a schematic view of the apparatus. High pressure air from a bank of

storage tanks flowed through a regulating valve and was then chopped by a rotating siren disk. The siren disk was driven at four different rotational speeds to produce pressure pulses of 479, 694, 881 and 1080 Hz. The pulsed air from the siren flowed through a 0.968 inch internal diameter tube. The tube length was adjustable from 20 to 117 in. The air flowed from the tube (at the far end from the siren) by passing through a thin circumferential slit formed by the end of the tube and an end wall perpendicular to the tube axis. An expanded view of this geometry is shown in Figure 21 which also shows the arrangement of the instrumentation. With the small gap at the exit end of the tube the resonant frequency of the tube could be calculated approximately as for a closed end tube. By experimental adjustment the tube could thus be run under resonant conditions. At a resonant length the pressure waves at the end wall were steep fronted (shock waves) followed by an expansion wave. Traveling upstream from the end wall the waves slowly changed to double the frequency with approximately half the amplitude of the waves at the end wall. Going farther upstream a second antinodal wave similar to the end wall wave was observed. A diagram of these wave shapes is shown in Figure 22. The waves at the end wall had amplitudes of up to 175 psi peak-to-peak. Average tube pressures from 40 to 190 psia were obtained. Flow visualization studies using a surface oil technique showed that the flow at the end wall was radially outward from the center of the wall with a center section in which no directed flow could be detected.

A particular operating point was fixed by the values of the siren frequency, tube length, end wall gap width and pressure upstream of the siren. Quantities measured were average tube pressure, instantaneous pressure at the end wall, average mass flow and instantaneous surface temperature at the center of the end wall. In addition, a 0.003 inch bead thermocouple located at the tube axis 1/2 inch from the end plate was used to monitor the "average gas temperature" at that point. The end wall surface temperature was measured by a platinum thin film resistance sensor mounted on Pyrex. The sensor was 0.062 inch long by 0.02 inch wide and 1000 A thick. The sensor was located at the center of a one inch diameter Pyrex disk mounted in the end plate. Under typical test conditions the oscillations in surface temperature ranged from 0.5 to 2°F in amplitude. Because of the low conductivity of Pyrex the time average component of heat transfer through the end wall was small compared to the fluctuating component of heat flux. The time average component could not be measured accurately, but was estimated to be from 0.05 to 0.40 BTU/ft²-sec.

Experimental Results

In considering the experimental data from the two heat transfer projects it is important to recognize the fundamental differences in the data regimes. The cylinder and piston device (CPD) gave high pressure ratio, low frequency, continuous pressure

oscillations while the periodic shock tube (PST) gave relatively low pressure ratio, high frequency, shock-fronted pressure oscillations. In addition, the CPD had a large time average heat flux while the PST time average heat was essentially zero.

Turning first to the CPD data, Figures 23, 24, 25 show typical pressure, gas temperature and wall surface temperature histories. Gas pressure histories showed only slight cycle-to-cycle variations with most of the variation being during the time when make-up air was flowing. The pressure swing was 365 ± 0.8 psi for all data with the peak pressure at 2.5 crank degrees BTDC. The bulk gas temperature showed moderate cycle-to-cycle variations especially in the region of TDC. The shape of the gas temperature histories was essentially the same at all frequencies (9 to 58 Hz) except for a slight shift in position of temperature maximum and an increase in amplitude of temperature swing from 560°F at the lowest frequency to 630°F at the highest frequency. The wall surface temperature histories showed considerable cycle-to-cycle variations. For this reason several cycles were recorded at each speed and the cycles averaged for interpretation. Figure 26 shows the trends of surface temperature and surface heat flux with crankangle for various frequencies. At low frequencies (up to 15 Hz) the peak wall temperatures came well after TDC while at the higher frequencies the peak was very close to TDC. At intermediate frequencies two maxima in surface temperature were observed.

Measurements of surface temperature and gas temperature at nine different locations on the head gave very similar results for all positions. In order to investigate the effects of possible secondary flows in the chamber, experiments were conducted with the make-up air ports blocked and with a fine nylon mesh screen parallel to and 0.12 inches from the head surface. Neither experiment showed any dramatic change in the experimental trends.

Typical experimental curves of pressure, surface temperature and heat flux as a function of time as obtained in the periodic shock tube are illustrated by Figs. 27, 28, and 29. As can be seen, the discontinuous rise in pressure (shock front) was accompanied simultaneously by a similar jump in surface temperature. The instantaneous heat flux would have to be infinite for a true step change in surface temperature. The heat flux curve can be generally characterized by the value of the normalized time at the zero flux point, τ_c , and by the magnitude of the total heat transferred during the positive heat flux portion of the cycle, Q_{pos} . In all of the data shown the small component of time average heat transfer to the wall has been neglected so that the integral of the heat flux over one cycle is zero.

For a fixed pressure wave shape the PST experimental parameters were frequency, pressure ratio, average tube pressure and average mass flow rate. The effect of mass flow rate was found to be negligible for all of the data. Values of Q_{pos} were found to

be proportional to the square root of average tube pressure and inversely proportional to the square root of frequency. For constant frequency and average pressure, Q_{pos} was found to increase almost linearly with pressure ratio. The time average flux during the positive portion of the flux curve can be compared to the time average flux during the negative portion by knowing τ_c . For a given pressure wave shape, τ_c was constant. Values of τ_c for all of the tests ranged from 0.34 to 0.24 so that the average positive flux was two to three times as large as the average negative flux.

Theoretical Model

The same basic modeling approach was used for both the CPD and PST data. The basic assumptions were that the flow is one-dimensional and in a direction normal to the heat transfer surface and that the pressure can be assumed to be a function of time only. With these assumptions one can write the equations of mass and energy conservation as

$$\frac{\partial \rho}{\partial t} + \frac{\partial \rho u}{\partial x} = 0 \quad (11)$$

$$\rho c_p \left[\frac{\partial T}{\partial t} + u \frac{\partial T}{\partial x} \right] = \frac{\partial}{\partial x} \left(k \frac{\partial T}{\partial x} \right) + \frac{dp}{dt} \quad (12)$$

with the ideal gas equation of state

$$P = \rho RT. \quad (13)$$

In these equations the following nomenclature is used:

- t = time
- x = distance measured from and normal to the heat transfer surface
- ρ = fluid density
- u = fluid density in x direction
- c_p = fluid constant pressure heat capacity
- T = fluid temperature
- k = thermal conductivity of fluid
- p = pressure
- R = specific gas constant

For both sets of experiments the wall surface temperature variation was small compared to the variation in gas temperature so that the wall temperature could be assumed constant. Thus the

boundary conditions at the wall surface, $x = 0$, were

$$u(0, t) = 0 \quad (14)$$

$$T(0, t) = T_{wall} \quad (15)$$

Similarly, a periodic solution is sought in both problems so that the condition of periodicity on all dependent variables replaces the need for initial values. Application of appropriate boundary conditions at the outer (gas side) boundary are more difficult to formulate. Considering the CPD conditions first, the velocity and temperature at the piston surface are known and can thus be used as boundary conditions. If one further assumes that the head and piston are at the same temperature then the temperature distribution at any instant should be symmetric around a moving adiabatic plane which is parallel to and equidistant from the head and piston.

The gas side boundary condition for the PST is more difficult to formulate. For the particular case of zero net heat transfer to the wall we may assume that the temperature gradient at the edge of the boundary layer is zero. In that case the gas at the edge of the boundary layer is undergoing an adiabatic compression and expansion. For small pressure ratios across the shocks one may approximate the relationship between pressure and temperature at the outer edge by the isentropic expression

$$T = T_o (p/p_o)^{(\gamma-1)/\gamma} \quad (16)$$

One must be careful however in such an approximation because although the difference between shock and isentropic temperature jump is small per cycle there are many cycles per second. If the same gas is shocked continuously this added energy dissipation could be important. Because the outer flow is actually turbulent, not simply one-dimensional, the outer flow can act as a sink for the extra energy added by the shock.

It should be clear from the model assumptions that neither of the experiments are completely modeled by Eqs. 11, 12, 13, and 16. First, both experiments probably have transport of energy in other than the x-direction by both flow and conduction. Secondly, the transport of energy by turbulence is neglected in the model. For the CPD experiment the model neglects the mass and energy effects of the make-up air flow and the energy flow to and from the cylinder sleeve and thus cannot correctly predict the pressure. Nevertheless, the model does explain the basic mechanisms and is useful in correlating the variables.

Solutions of the basic model equations were obtained in both projects by numerical methods. Since completion of these projects Weast and Burmeister (25) have shown that an analytical solution can be obtained if one assumes that the temperature at the gas side boundary is given by Eq. 16 and that the gas thermal conductivity is proportional to the absolute temperature. These conditions correspond to the PST model with zero net heat transfer at the wall. Both the numerical and analytical methods require that the pressure-time history be given from the experimental data. The value of the reference temperature T_0 can be determined by combining the condition of zero net heat transfer per cycle and the experimental value of the wall temperature. The solution for the CPD model follows the same procedure if one uses the experimental pressure and assumes that the center core of gas is a closed adiabatic system. Wendland (23) however chose to predict the pressure variation from the known volume-time relationship and the assumption of a closed system with heat exchange only at the head surface. While this procedure has the advantage of not requiring experimental pressure data as input it has the disadvantage of introducing an inaccurate pressure-time relationship.

Neither experiment gave detailed instantaneous temperature profiles in the gas so exact comparisons of theory and experiment were impossible. In the following section comparisons are made between measured and theoretical instantaneous heat flux at the wall. Before discussing these comparisons however it is instructive to examine the theoretical results in terms of the qualitative behavior of the heat exchange process. Figures 30 and 31 show calculated temperature profiles at various times during the compression and expansion stroke of the CPD. Figure 32 gives similar curves from the PST model calculations. In both cases the qualitative explanation is similar although the large difference in rate-of-compression between the two experiments causes the profiles to be different in shape. In both cases it can also be seen that local extremum values of gas temperature appear near the wall.

To understand the appearance of these "humps" it is necessary to think about the compression work which is added to slabs of gas at various distances from the wall. The gas at the wall undergoes an essentially isothermal process while the gas at the outer boundary undergoes an adiabatic compression process. Figure 32 shows the effects of this dramatically. Just before the shock ($\tau = 0.99$) the gas temperature decreases monotonically with distance from the wall. Just after the shock ($\tau = 0.001$) the gas to the right of the maximum temperature point has been compressed approximately adiabatically (and exactly so at the maximum point and at the far right boundary) from its temperature at the time just prior to the shock while the gas to the left of the maximum shows a steep gradient because of heat transfer to the wall. The same phenomena shows up in Figure 30, however the peaks are much lower because the compression is relatively slow and heat transfer

by conduction has time to spread out the energy. As expansion occurs the cooler gas near the wall may cool below both the wall and the outer boundary temperature (see +40° curve of Figure 31). Under this condition the wall transfer heat to the gas while the wall temperature is lower than the outer boundary (bulk gas) temperature. Obviously, if one tries to apply a conventional heat transfer coefficient definition under this condition the coefficient will be negative (or infinite if the wall and outer boundary temperatures just match). A similar phenomenon may occur during compression if the hump in gas temperature causes heat transfer to the wall before the bulk gas temperature rises above the wall temperature.

Comparisons of Theoretical and Experimental Results

Comparisons of theoretical predictions of q_{pos} and the fluctuating component of heat flux at the wall surface with experimental PST data showed excellent agreement. No comparisons of time-averaged heat transfer could be made because the model assumptions were made for an assumed zero value and the small experimental component could not be accurately measured. Variation of the average mass flow rate from 0.13 to 0.48 lb_m/sec did not influence the experimental results as can be seen from Figure 33. This confirms the theory hypothesis that during one cycle the gas next to the center of the end wall is essentially stagnant except for one-dimensional compression and expansion effects.

Comparisons of calculated and experimental heat fluxes for the CPD data showed good agreement in shape and phasing for the higher frequencies. The double hump shape at lower frequencies was not predicted by the model. The causes of the unpredicted shape of the low frequency data heat flux histories were unresolved. Similar shapes have been observed in internal combustion engines where the phenomena is thought to be related to turbulence and three-dimensional flows. The predicted values of time-average heat transfer and peak heat flux were about one-half of the experimental values. Recent studies which introduce a turbulent conductivity into the model equations give much better agreement with the experimental results indicating that turbulence plays a predominant role in calculating the net heat transfer rates.

The results of the heat transfer studies show the importance of pressure work in modeling heat transfer under conditions of large pressure oscillations. The agreement between theory and experiment is encouraging and suggests that future work which includes the effects of two-dimensional flow and turbulence would be profitable. The extension of the work to unsteady mass transfer under flow conditions similar to those reported here would be very useful in helping to understand vaporization phenomena during oscillatory combustion.

DISTRIBUTIONS IN SPRAYS

The study of droplet size and velocity distributions in sprays conducted under this grant (26) was a continuation of research sponsored from other sources over a period of some six previous years (27,28). The experimental methods used were thus modifications of the method previously developed at Wisconsin.

Experimental Method

The key feature of the technique of droplet spray photography used in the study was the addition of fluorescent dye (0.5% by weight) to the liquid being sprayed. Upon excitation by an intense light source, the dye absorbs in one wavelength band and emits in another making each drop a radiator which exposes the photographic film. A shaped beam of light directed perpendicular to the camera axis was used to illuminate a thin rectangular volume (0.16 x 0.16 x 0.008 inches) for a duration of about 2 milliseconds. Figure 34 shows the experimental arrangement. The spray was formed by a swirl atomizer spraying into room air. Because each droplet image consists of an exposed spot on an unexposed background it is possible to flash the light source a number of times and thus obtain multiple samples of the illuminated volume. Size resolution of droplets was $10\mu \pm 10\%$ as determined by static calibration.

In the original developmental work prior to the present study, the plane of the light sheet was perpendicular to the spray axis. Spatial droplet size distributions were obtained by using a flying spot scanner (drop size counter) to measure the image sizes on the film. Such distributions are weighted by the droplet velocities which are not equal. Furthermore the data cannot give any information about the velocity distribution. Because of this limitation the light plane in the present investigation was formed parallel to the spray axis. Two specially constructed spark light sources were used to obtain two consecutive samples with a preset time interval between flashes. The time interval was variable between 9.5 and 74 milliseconds respectively (see Figure 35). If the time interval between flashes is short enough the film will show two images of each droplet. By measuring the distance traveled in the known time interval the droplet velocity can be calculated. Ideal flash duration and time interval were estimated to be 0.1 milliseconds and 10 milliseconds respectively (see Figure 35). Because the spark flash source gave much longer than ideal flash duration, the droplet images were blurred for the small fast moving droplets. Feasibility experiments with a laser light source (29) indicated that such a source would greatly extend the range of drop velocities that could be successfully measured. However, no laser source which would give repeatable control of the duration between flashes was available. Repeatability of the time duration between flashes using the spark gaps was ± 0.2 milliseconds.

Ethyl alcohol containing fluorescein was injected at room temperature through the swirl atomizer which was nominally rated at 0.175 gallon/hour at 100 psig for fuel oil and had a minimum orifice diameter of 0.009 inch. The spray was sampled radially at various axial positions as shown in Figure 36. Raw data records consisted of over 200 films each of which had up to 200 pairs of drop images. The droplet images had a magnification of 25x on the film and an additional magnification of 18.1x was achieved by viewing the films through a microcard reader. Each film was divided into 1/2 inch square grid of blocks which each contained about six droplet pairs. Measurements of droplet diameter, angle of path and distance between droplet pairs were accomplished by manual readings using a transparent scale and protractor. A total of 32,000 pairs of drop images were measured.

Experimental Results

Bivariate, size-velocity density functions were constructed as a function of position from the raw data. Quantities calculated from the experimental density functions included: (a) bivariate mass densities, (b) marginal* mass densities as a function of size, (c) marginal mass densities as a function of velocity, (d) mass flux as a function of size, (e) one-dimensional forms of all these density functions (obtained by integration over the spray cross-section), (f) profiles of mean spray quantities (obtained by integrating over size and velocity), and (g) spray vaporization and drag terms using the single drop expressions. Quantitative plots of these quantities can be found in Reference 26. Rather than repeating these plots here, only a schematic representation of the results will be summarized.

The situation existing in the study where the mean velocity at the exit of the atomizer, v_E , was greater than the ambient air velocity, u ; is illustrated in Figure 37. Each contour plot of the mass density surface in the size-velocity plane is accompanied by the marginal density functions of diameter or velocity alone obtained by integration over one of the two variables. The mass density as a function of diameter is the traditional spatial drop size distribution measured by photographic methods, while the counterpart as a function of velocity has not been measured previously. The relationship between the size distributions is also noted for each case. Since no vaporization is considered, the mass flux as a function of drop size must propagate unchanged.

Immediately after formation one large "hill" forms the mass density surface. It is slightly distorted at smaller sizes and velocities by the deceleration process which has already begun for the oldest of the smaller droplets. Droplet mass per unit spatial volume is definitely distributed with respect to velocity to as

*The term marginal indicates that the integration over at least one of the variables is not carried out.

great a degree as with respect to size. Note that the mass average velocity is less than injection velocity due to dissipation in the break-up process. The expected value of velocity at any size is approximately constant. This means that the mass flux distribution is simply this constant times the mass density.

At an intermediate condition where considerable gas drop interaction has occurred, selective deceleration according to size has divided the original "hill" into two peaks connected by a ridge. Consequently, the marginal densities are bimodal. The original single formation mode has diminished; the spatial density of small drops has increased with respect to larger drops; and a sharp peak has formed at the gas velocity. Average values of drop velocity at any size now vary greatly with size. In fact, the shape of the $\langle v | D \rangle$ curve* is exactly the form that will transform the bimodal spatial mass distribution back into the original unimodal mass flux distribution.

Finally, if the gas velocity is nearly constant, a location far downstream may be found where the spray and gas are near velocity equilibrium. Nearly all of the drops have approached gas velocity forming a long, narrow and very high peak. Since $\langle v | D \rangle \approx u$, the flux distribution differs from the spatial distribution by simply this constant multiplier.

Reasoning from Figure 37, the corresponding curves for the case of injection into a higher velocity gas stream can be constructed as shown in Figure 38. Since measurements were not made on a spray under these conditions, some details may be missing; but the overall behavior is illustrated. The situation is one of acceleration during propagation; and as always, small drops are the most responsive. Contours of the mass density are inverted with respect to the velocity axis compared to Figure 37. At the intermediate condition the spatial density of small drops decreases compared to large drops which continue to move more slowly.

When substantial vaporization is present, removal of liquid mass, which is greatest in the low-to-medium size range, will distort the entire picture; and the flux distribution no longer propagates unchanges.

Profiles of mean quantities, of course, reflect in a gross manner the detailed behavior just reviewed. However, in the case of bimodal density functions, it becomes very difficult to extract the physical picture from the single set of means representing combined characteristics.

* $\langle v | D \rangle$ is the expected value of v given D .

Analytical Description of Spray Situations

In Reference 26 the statistical mechanics approach to the spray propagation problem which was formulated in References 3 and 30 is extended to include droplet internal energy (droplet temperature) as a random variable. The key construction of such analysis is the density function $f(\Gamma_i, t)$, where the Γ_i are randomly distributed and the time, t , is a parameter. Reasonable choices for the Γ_i are size D , position \underline{x} , velocity \underline{v} and temperature T_L . The function f has characteristics of both physical density (number of drops per unit Γ_i), and a probability density since it represents the probable number of drops in the range $d\Gamma_i$ about Γ_i at a time t . The development and resulting spray transport equation and gas dynamic equations of change to be found in Reference 26 will not be repeated here for sake of brevity.

In its present stage of analytical development, the primary usefulness of the statistical mechanical formalism is as a conceptual aid to organizing the attack on spray problems. The reduction of the general spray transport equation to equations of change provides a unified treatment of the gas and liquid phase dynamics. Resultant mean spray quantities defined on a physical basis can then be associated with the traditional statistical moments defined strictly in terms of mathematical operations.

Two barriers to realistic solutions of spray propagation problems exist. Mathematically, the available solutions to transport similar to the one posed by the spray equation are few and of very restricted form. Numerical methods appear to be a necessary resort since analytically simplifying assumptions such as Stokes Law drag or stagnant vaporization cannot represent many spray situations of practical interest. The other impediment is the ignorance of initial conditions in the form of the spray density function in the case of the general spray equation or the mean quantities in cases where integrated equations of change are used.

Conclusions

Drop velocity in a spray is a statistically distributed variable the knowledge of which is equally important to drop size. Without such information to fix the dynamic state of the spray, little insight into formation or propagation mechanisms can be gained. For example, the processes which produce bimodal density functions can only be conjectured; and calculations of liquid mass or momentum transport rest on questionable, assumed values of mean velocity.

The characteristics of the bivariate, size-velocity density function are strongly dependent on position with the key feature determining the variations being the amount of droplet-gas inter-

action that has occurred. An extremely wide range of shapes and modal conditions of the spatial distribution can be found in the same spray simply by sampling at different locations. Unless the sampling conditions are clearly specified, no basis for the comparison of spatial drop size data exists.

In many cases the differences in the shape and modal characteristics of spatial and flux distributions are large. Only in very special situations where the spray approaches velocity equilibrium with the gas are photographic and collection data equivalent. The flux distribution implicitly contains drop velocity information although it is not readily extractable without some additional data on spatial densities. In cases where vaporization is negligible, the shape of the one-dimensional flux distribution indicates whether or not drops were actually formed with more than one mode with respect to size.

Failure to recognize the significance of velocity, the degree of spatial dependence, and the distinction between densities and fluxes has led to much confusion in interpreting spray data. It is understandable that no general agreement exists as to the most useful empirical equation to fit measured distributions. If data representing a myriad of spray situations are lumped together to obtain a general correlation, the most versatile equation (usually the one with the largest number of parameters) is bound to give the best fit. The actual generality and usefulness of such a correlation are questionable. Statistical sampling uncertainties are always present, but all inconsistencies in data should not be assigned to this catch-all excuse. Basic differences in the physical situations which the data represent are factors which deserve equal scrutiny.

Suggestions for Future Experiments

The significance of the spray density function measured at the surface of formation justified further experimental efforts to measure it for a wider range of injection parameters. In addition to providing initial conditions for propagation calculations, such information is necessary for new efforts to develop a theory of spray formation. More quantitative criteria for locating the surface of formation are desirable extensions of past breakup length studies.

Methods of measuring spray droplet temperatures need to be developed so that its inclusion as a random variable in the spray density function can be verified.

The characterization of gas properties in a spray deserves more attention. Reliable values of local gas velocities and temperature are required before definite conclusions can be drawn about the ability to calculate local vaporization rates and droplet concentrations.

Time variations in the spray properties remain largely unexplored. Unsteady spray density functions, even for size alone, have rarely been measured; and a knowledge of continuous time histories under steady-state conditions would shed light on the ergodic problem and the possible excitation of resonant phenomena by spray fluctuations.

At present, the general spray density function is too difficult to measure and contains more information than can be readily handled in practical applications. Use of the mean spray properties in the form of overall macroscopic balanced obtained from the equations of change seems to be a more expedient design or development approach. However, such methods can only be implemented if experimental techniques are developed to measure mean spray properties, such as the spray density, directly without resorting to individual drop measurement.

The problem of obtaining reliable experimental estimates of statistical quantities suggests the development of more automated data collection and reduction techniques so that larger samples can be obtained. It should be realized, however, that complex hardware may tend to obscure the familiar difficulties. Television cameras have recording thresholds and exposure characteristics affecting the apparent particular size just as film does. Flying-spot film scanners require careful monitoring of signal clipping levels to realize the possible, but not automatic, advantage of consistency over manual measurements. At times it may be preferable to sacrifice quantity and rapidity for the sake of directly examining an additional droplet variable.

SUMMARY OF CONCLUSIONS

In the preceding sections a brief description is given of the experimental and theoretical projects conducted under the grant and the major conclusions. In this section the major conclusions are reiterated for those readers who wish to obtain only a capsulated view of the research results.

Droplet Vaporization

(A) A spherically symmetric droplet vaporization model was constructed to include the effects of high ambient pressure and variable properties through the boundary layer. The calculations using this model gave the following conclusions.

- (1) Using mean rather than continuously variable properties through the boundary layer can cause mass transfer rates to shift by as much as 35%.

- (2) The effects of high ambient pressures on properties cannot be neglected. In particular the heat of vaporization and mole fraction of the vapor at the droplet surface are greatly affected by pressure.
 - (3) For ambient pressures greater than the critical pressure of the liquid a critical point for the mixture exists at temperature substantially below the pure liquid critical temperature. For a given ambient pressure there will exist an ambient temperature above which the droplet will not reach a steady-state (wet bulb) temperature. In such cases the droplet history will be completely unsteady. The droplet will continue to heat up to the pure liquid critical temperature.
 - (4) Vaporization times may be estimated by the quasi-steady film theory over a wide range of ambient conditions provided that the vapor pressure and heat of vaporization are properly corrected for the effect of total pressure.
 - (5) At high temperatures and pressures the vaporization rate is in phase with small sinusoidal variations in ambient pressure.
- (B) Experiments were conducted to measure the size and temperature histories of liquid-heptane, Freon-13 and carbon dioxide droplets suspended in a flowing stream of high pressure heated air. Experimental histories were compared to film theory calculations. The following conclusions were obtained:
- (1) Droplet histories at supercritical pressures and liquid temperatures up to 95% of the pure liquid critical temperature could be obtained by the suspended drop technique.
 - (2) For n-heptane droplets with ambient temperatures low compared to the liquid critical temperature and ambient pressures up to 3.7 times the critical pressure, the film theory with heat of vaporization and mole fraction corrected for pressure predicted experimental steady-state temperatures to within 25% ($\pm 6^\circ\text{F}$).
 - (3) For Freon-13 droplets with ambient temperatures up to 1.5 times the critical and pressures up to 1.75 times the critical, corrected film theory predicted steady-state temperature 10 to 15 $^\circ\text{F}$ lower than the experimental values and mass transfer rates 35 to 50% lower than the measured values. The divergence between experimental and measured rates increased with total pressure.

- (4) For carbon dioxide droplets with ambient temperatures up to 1.3 times the critical and pressures of 0.75 and 1.0 times the critical, the corrected film theory steady-state temperatures were within 5°F of the experimental values and the mass transfer rate within 30 to 40%. Again the highest error in mass transfer predictions came at the highest pressure.
 - (5) Correcting the vapor pressure and heat of vaporization for pressure greatly improved the agreement between theory and experiment. However, Nusselt numbers obtained from low pressure experiments appear to be 30 to 40% too low for the conditions tested here.
 - (6) Calculations at high pressures require dependable thermodynamic data for mixture properties at high pressures. Theoretical property values unsupported by data may give substantial errors when applied to the film theory for vaporizing droplets.
- (C) Experiments were conducted to obtain photographic histories of carbon dioxide droplets falling through inert environments. Pressures from 0.5 to 2.0 times the critical of carbon dioxide were used. For nitrogen and argon ambient temperatures of 1.0 and 1.25 times the critical of carbon dioxide were used. Ambient temperatures for helium were from 1.0 to 3.5 times the critical of carbon dioxide. The following conclusions were obtained.
- (1) The steady-state temperature of a carbon dioxide droplet falling in helium can be estimated from its size and period of oscillation. Experimental droplet temperatures of up to 95% of the critical temperature of carbon dioxide were estimated using this technique.
 - (2) For a constant subcritical pressure the experimental steady-state temperature of carbon dioxide droplets falling in helium appear to approach an asymptote as ambient temperature is increased. The logical asymptote is the phase equilibrium temperature for pure carbon dioxide at that pressure.
 - (3) For a given supercritical pressure the experimental data for carbon dioxide droplets falling in helium show an upper limit of ambient temperature for which steady-state droplet temperatures are observed. For ambient temperatures above this limit streamers or globules of dense liquid like material are detached from a droplet by the aerodynamic drag force. This removal of material appears to be primarily due to a difference in properties between a droplet's surface

and its core. This is different than the cases usually discussed in the literature where the material removal is primarily due to a sudden increase in drag force or to a progressive increase in the amplitude of droplet oscillation to the point of instability.

- (4) For a given supercritical pressure dense liquid-like material detaches from a carbon dioxide droplet falling through nitrogen or argon at a much lower ambient temperature than from one falling through helium. For a given pressure the critical mixing lines of nitrogen-carbon dioxide and argon-carbon dioxide systems occur at a much lower temperature than the critical mixing line of the helium-carbon dioxide system. The assumption that liquid-like material detaches when the liquid near a droplet's surface approaches its critical mixing state appears compatible with these observations. Simultaneous thermal and molecular diffusion inward from a droplet's surface needs to be studied in order to better understand the approach of material near its surface to a critical mixing state.

Experimental measurements of the instantaneous heat transfer at a solid surface exposed to a gas undergoing pressure oscillations were performed and comparisons were made with calculations using a one-dimensional energy equation for the gas. Large amplitude, low frequency (15 to 58 Hz) sinusoidal type oscillations were produced by a piston-cylinder device. The effects of repetitive (500 to 800 shocks/sec) shock waves impinging on the end wall of a tube were investigated by use of a siren shock wave generator. The following conclusions were obtained.

- (1) In addition to thermal conductive and capacitive effects in the boundary layer the effect of rate-of-change of pressure is an important parameter in determining heat transfer under the conditions studied. The rapid compression of the boundary layer by the arrival of a shock wave causes the temperature profile to have a maximum value within the thermal boundary layer a short distance from the wall resulting in a large peak heat flux. A lower rate of pressure rise would allow more time for conduction and would give a lower peak and thus lower peak heat flux.
- (2) Both the model and experiment showed that for periodic shock wave impingement the instantaneous heat flux is proportional to the square root of the product of time-averaged pressure and frequency. The heat flux was also found to increase with an increase in pressure ratio across the shock.

- (3) For the shock wave studies the temperature rise of the solid surface was in phase with the pressure waves. Similarly, for the piston-cylinder data at frequencies of 30 to 60 Hz the wall surface temperature was found to lag the pressure by only a few crank degrees.
- (4) For the sinusoidal type pressure oscillations the time-average heat transfer to the wall was large. The one-dimensional laminar flow model under-predicted this time-average heat transfer by as much as 50%. For the repetitive shock experiments with a low conductivity wall the net heat transfer was very small and the one-dimensional laminar model predicted the instantaneous heat flux correctly. The results thus indicate that the mechanism of turbulent heat transfer is important in determining net heat flux, but that laminar models may be used to predict the phase relationships.
- (5) For unsteady heat transfer with pressure oscillations the temperature difference between the wall and bulk gas does not always correctly predict the direction of the heat flux at the wall. Thus the definition of an instantaneous convective heat transfer coefficient based on the instantaneous temperature difference between wall and bulk gas can give negative or even infinite coefficients.

Distribution in Sprays

Droplet size and velocity distributions were experimentally measured in a spray by use of double-exposure fluorescent photography. The following conclusions were obtained.

- (1) Droplet velocity in a spray is a statistically distributed variable the knowledge of which is equally important to droplet size.
- (2) The form of the bivariate, size-velocity density functions is strongly dependent on position with the key feature determining the variations being the amount of droplet-gas interaction that has occurred.
- (3) Bimodal density functions are formed during propagation by selective deceleration of drops according to size.
- (4) In many cases the differences in the shape and modal characteristics of spatial and flux drop size distributions are large.

APPLICATIONS OF RESULTS

The main applications of the research carried out under this grant apply to heterogeneous combustion devices such as rockets,

diesel engines, gas turbines and stationary oil burners. The work on high pressure vaporization is of course of interest to chemical engineers as well as rocket and diesel designers. The heat transfer experiments may have applications in heat exchangers in addition to the problem of rocket instability. This section of the final report thus indicates some of the implications of the research results for applications and suggests areas which need more study.

Although sprays have been the source of countless researches the models for analysis remain relatively crude. As in the theory of gases one can either study the behavior of individual particles or study the behavior of the bulk properties by use of statistical techniques. In either case the velocity distribution of the droplets at the initial cross section where calculations are to begin has been shown to be important for the swirl type atomizer studied under this grant. Application to rockets or diesels would require new information giving the velocity and size distributions. Recent developments in laser technology may make the fluorescent technique developed here more attractive, however the problem of data reduction would remain time consuming. Given the distribution functions, the methods using distribution equations given in Reference 26 seem more attractive than the single droplet approach.

For a given spray model one must still use correlations for droplet break-up or shedding and correlations for droplet vaporization. The study of suspended droplet vaporization at high pressure shows that film theory even when corrected for high pressure properties underestimates mass vaporization rates by as much as 50%. The data taken at high temperatures and pressures for falling drops is less conclusive but indicates that corrected film theory may underestimate vaporization rates for carbon dioxide vaporizing in helium. Based on these results only tentative suggestions can be made for calculation of vaporization in rocket efficiency studies. Our suggestion is to correct all properties if possible for pressure assuming an equilibrium mixture at the droplet surface and to use these properties in the film theory equations of Reference 12. Such calculations would predict the point at which the critical mixture is formed at the droplet surface. The falling droplet study indicates that if the critical mixture point is reached droplet shedding and break-up may make the effective vaporization rate very high. A speculative technique would be to assume instantaneous vaporization of the remaining mass at the time the critical mixing point is reached. Considering the very rapid rates which would occur after this point even without breakup the suggested procedure seems reasonable. The effect of such behavior on instability in rockets is difficult to judge. If burning starts prior to reaching the critical mixing point no data from the grant study applies. If essentially instantaneous vaporization of some droplets takes place prior to combustion the burning rates will be controlled by mixing and chemical kinetics. Diesel engines are believed to

exhibit premixed type combustion during the initial stages of heat release. This premixed burning is believed to be the cause of the high rate of pressure rise which is typical in diesels. A similar effect in rocket engines could be a factor in combustion instability.

The response of vaporizing droplets to pressure oscillations was briefly treated for the spherical boundary layer model. Calculations at high frequencies and very small pressure ratio variations showed a positive response factor with negligible relaxation time for the boundary layer. The latter implies that film theory corrected for pressure might be used to predict response factors for such cases. The effect of large amplitude pressure oscillations was not explored however and may change the results considerably. Looking at the results of the heat transfer with pressure oscillations one sees that for pressure variations with substantial pressure ratios and higher frequencies the pressure and heat transfer are in phase and the rate of heat transfer is greatly enhanced. The implications of this for a vaporizing fluid have not been worked out under the grant, but the results imply a potential for greatly increased vaporization rates.

In summary, it is clear that additional work is required if accurate predictions are to be expected for spray and instability models. Additional work is needed on properties at high pressure even if only to apply the current theory. Additional falling droplet work including more realistic combinations such as liquid oxygen in a hydrogen atmosphere with better control of the initial droplet temperature would help to determine accuracy of the film theory. The experimental work on heat transfer in an oscillating pressure field should be expanded to include mass transfer from the surface.

REFERENCES

1. Priem, Richard J.; and Heidmann, Marcus F.: Propellant Vaporization as a Design Criterion for Rocket Engine Combustion Chambers. NASA TR R-67, 1960.
2. Ranger, A. A.; and Nicholls, J. A.: Aerodynamic Shattering of Liquid Drops. AIAA J., Vol. 7, No. 2, Feb. 1969, pp. 285-290.
3. Williams, F. A.: Theoretical Studies in Heterogeneous Combustion. Ph.D. Thesis, Calif. Inst. of Tech., 1958.
4. Priem, R. J.; Borman, G. L.; El-Wakil, M. M.; Uyehara, O. A.; and Myers, P. S.: Experimental and Calculated Histories of Vaporizing Fuel Drops. NACA TN 3988, 1957.
5. Wieber, Paul R.: Calculated Temperature Histories of Vaporizing Droplets to the Critical Point. AIAA J., Vol. 1, No. 12, December 1963, pp. 2764-2770.
6. Priem, R. J.; and Guentert, D. C.: Combustion Instability Limits Determined by a Nonlinear Theory and a One-Dimensional Model. NASA TN D-1409, 1962.
7. Heidmann, M. F.; and Wieber, P. R.: Analysis of n-Heptane Vaporization in Unstable Combustor with Traveling Transverse Oscillations. NASA TN D-3424, May 1966,
8. Overbye, V. D.: Variation of Instantaneous Wall Temperature Heat Transfer, and Heat Transfer Coefficients in a Spark Ignition Engine. Ph.D. Thesis, University of Wisconsin, M. E. Dept., 1960.
9. Harrje, David T.: Heat Transfer in Oscillating Flow, Final Report, ONR, 483g, Contract USN-Nonr 1858 (29), NR 094-200, Princeton University, 1967.
10. Manrique, J. A.: Theory of Droplet Vaporization in the Region of the Thermodynamic Critical Point. NASA CR-72558, June 1969. See also: Calculations of Steady State Droplet Vaporization at High Ambient Pressures. Int. J. Heat Mass Transfer, Vol. 12, 1969, pp. 1081-1095.
11. Savery, C. William: Experimental Studies of the Vaporization of Droplets in Heated Air at High Pressures. NASA CR-72574, August 1969.
12. Savery C. W.; Juedes, D. L.; and Borman, G. L.: n-Heptane, Carbon Dioxide, and Chlorotrifluoromethane Droplet Vaporization Measurements at Supercritical Pressures. Ind. Eng. Chem. Fundam., Vol. 10, No. 4, 1971, pp. 543-553.

13. SOWLS, Richard E.: An Experimental Study of Carbon Dioxide Droplets Falling Through an Inert High Pressure High Temperature Environment. Ph.D. Thesis, Dept. of Mech. Engr., University of Wisconsin, Madison, 1972.
14. El-Wakil, M. M.; Uyehara, O. A.; and Myers, P. S.: A Theoretical Investigation of the Heating-up Period of Injected Fuel Droplets Vaporizing in Air. NACA TN 3179, 1954.
15. Heidmann, M. F.; and Wieber, P. R.: Analysis of Frequency Response Characteristics of Propellant Vaporization, NASA TN D-3749, 1966.
16. Ricart-Lowe, Jaime, A.: Design of an Apparatus for Studying The Vaporization of Droplets in the Region of Their Critical Point. M. S. Thesis, University of Wisconsin, 1966.
17. Lamb, Sir Horace: Hydrodynamics, 5th edition. Dover Publications, New York, 1945, Article 276, pp. 473-475.
18. Gielessen, J.; and Schmatz, W.: Die Oberflächenspannung von Flüssigkeiten unter Fremdgasdruck bis zu 1000 kp/cm². Zeitschrift für Physikalische Chemie Neue Folge, Bd. 27, 1961, pp. 157-170.
19. Slowinski, E. J.; Gates, E. E.; and Waring, C. E.: The Effect of Pressure on the Surface Tensions of Liquids. J. Phys. Chem., Vol. 61, 1957, pp. 808-810.
20. Handbook of Chemistry and Physics. Chemical Rubber Company, 1971, p. F-31.
21. Mackendrick, R. F.; Heck, C. K.; and Barrick, P. L.: Liquid-Vapor Equilibria of the Helium-Carbon Dioxide System. Journal of Chemical and Engineering Data, Vol. 13, No. 3, July 1968, pp. 352-353.
22. Burfield, D. W.; Richardson, H. P.; and Guereca, R. A.: Vapor-Liquid Equilibria and Dielectric Constants for the Helium-Carbon Dioxide System. A.I.Ch.E. Journal, Vol. 16, No. 1, Jan. 1970, pp. 97-100.
23. Wendland, D.W.: The Effect of Periodic Pressure and Temperature Fluctuations on Unsteady Heat Transfer in a Closed System. NASA CR-72323, March 1968,
24. Goluba, Raymond W.: The Effect of Periodic Shock-Fronted Pressure Waves on the Instantaneous Heat Flux at the End-Wall of a Tube. NASA CR-72443, August 1968. See also: The Effect of Periodic Shock-Fronted Pressure Waves on Instantaneous Heat Flux Rates. Int. J. Heat and Mass Transfer, 12, pp. 1281-1293, 1969.

25. Weast, T.; Burmeister, L.: Heat Transfer From a Pressurized Gas to a Temperature Sensor. 1970 Heat Transfer Conference, Preprint MT1.9, Versailles, France.
26. Groeneweg, J. F.: The Statistical Description of a Spray in Terms of Drop Velocity, Size, and Position. Ph.D. Thesis, M. E. Dept., U. W., Madison, 1967. See also: NASA TMX52355.
27. Benson, G. M.; El-Wakil, M. M.; Myers, P. S.; and Uyehara, O. A.: Fluorescent Technique for Determining the Cross-Sectional Drop-Size Distributions of Liquid Sprays. ARS J., Vol. 30, No. 5, May 1960, pp. 447-454.
28. Rice, Edward J.: The Effect of Selected Fluid Parameters on Spatial Drop Size Distribution. Ph.D. Thesis, University of Wisconsin, 1966. See also: NASA TMX52381.
29. Groeneweg, H.; Hiroyasu, H.; Sowls, R.: Fluorescent Photography of Droplets in a Spray Using a Q-Switched Laser as a Light Source. British J. Applied Physics, Vol. 18, pp. 1317-1321, 1967.
30. Williams, F. A.: Progress in Spray Combustion Analysis. Eighth(International) Symposium on Combustion, Williams and Wilkins, 1962, pp. 50-69.

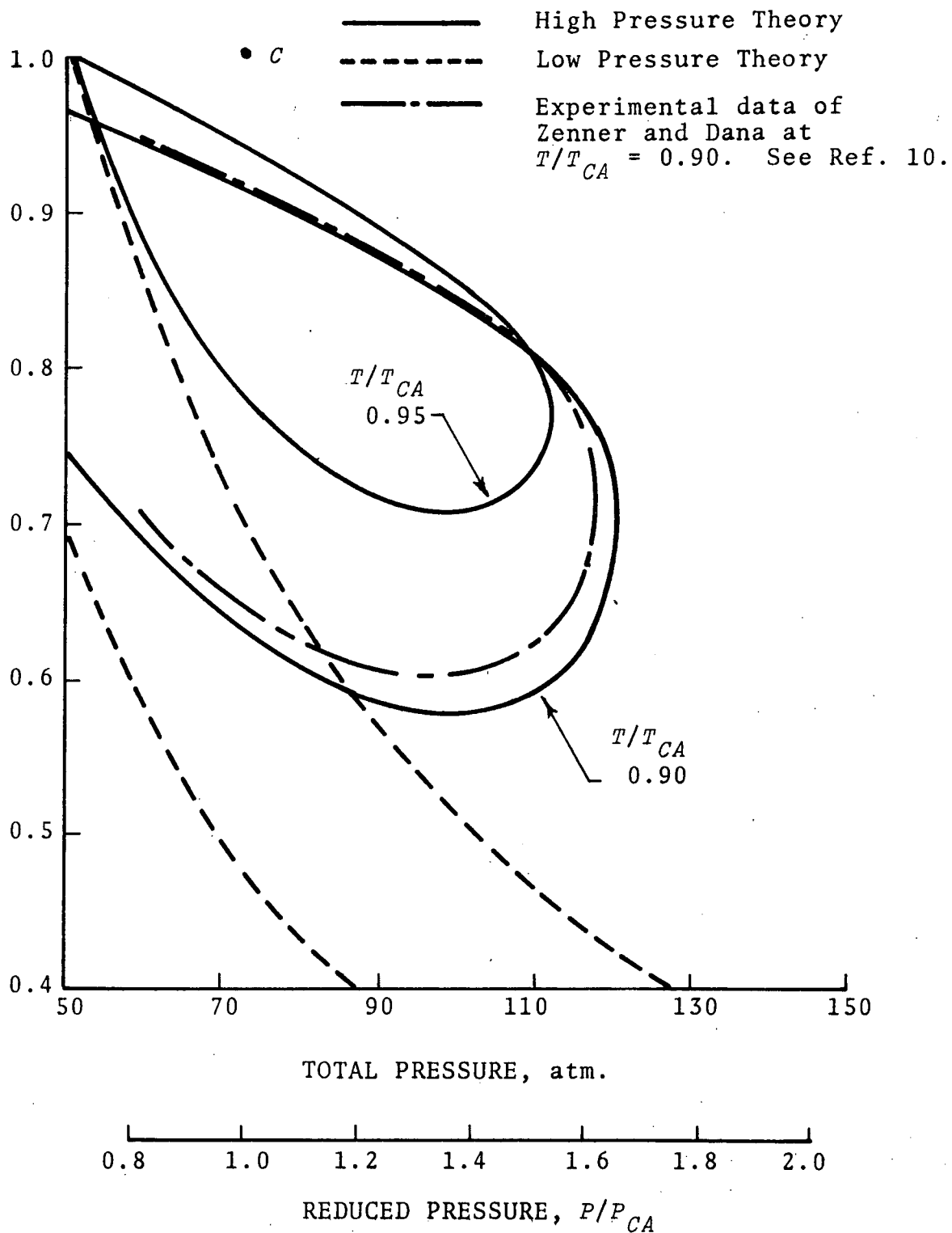


Figure 1. Calculated vapor-liquid equilibrium isotherms for the carbon dioxide-nitrogen system. (*C* = critical point of CO₂).

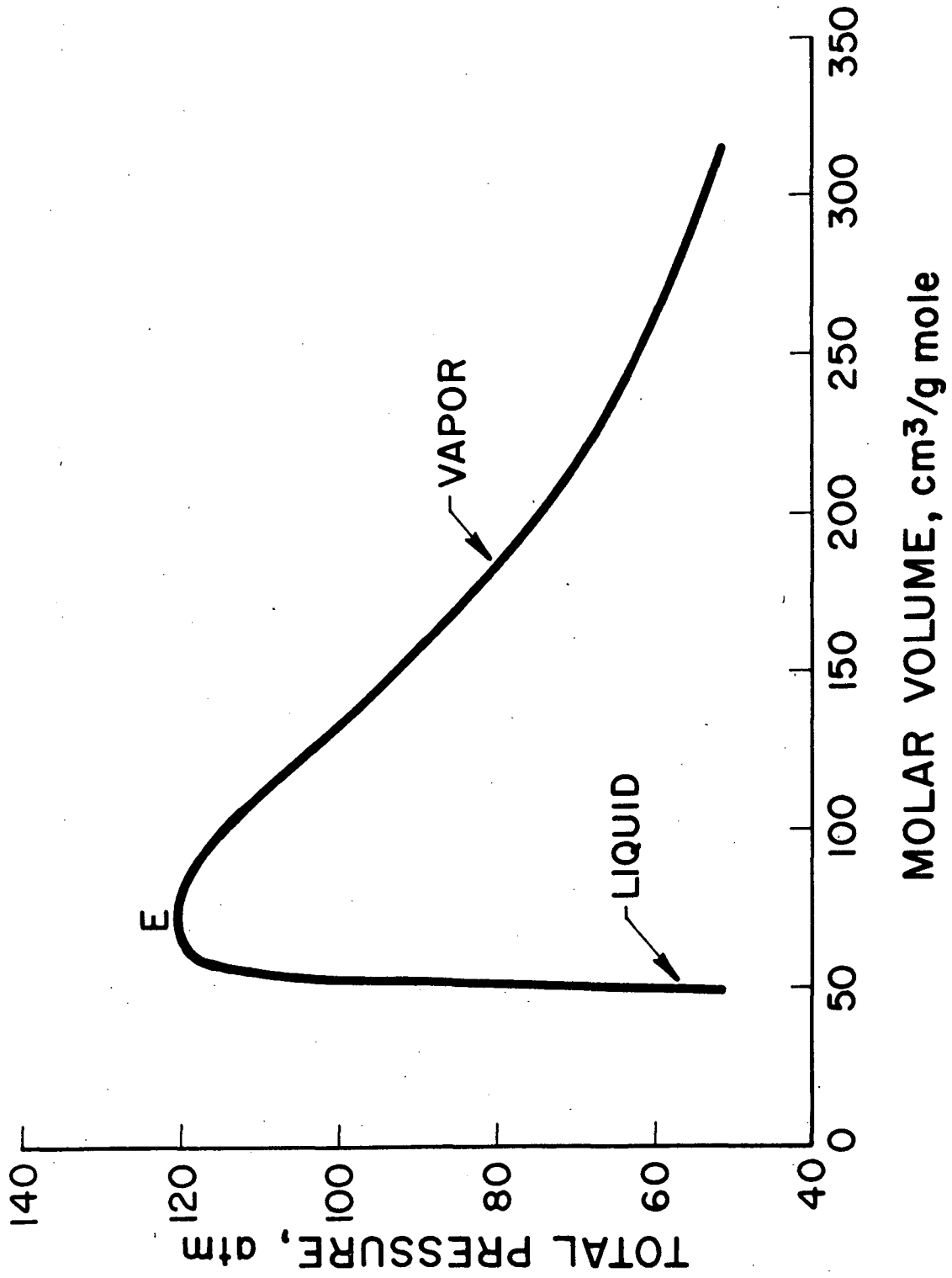


Figure 2. Pressure-molar volume diagram for the carbon dioxide-nitrogen system at $T/T_{cA} = 0.90$.

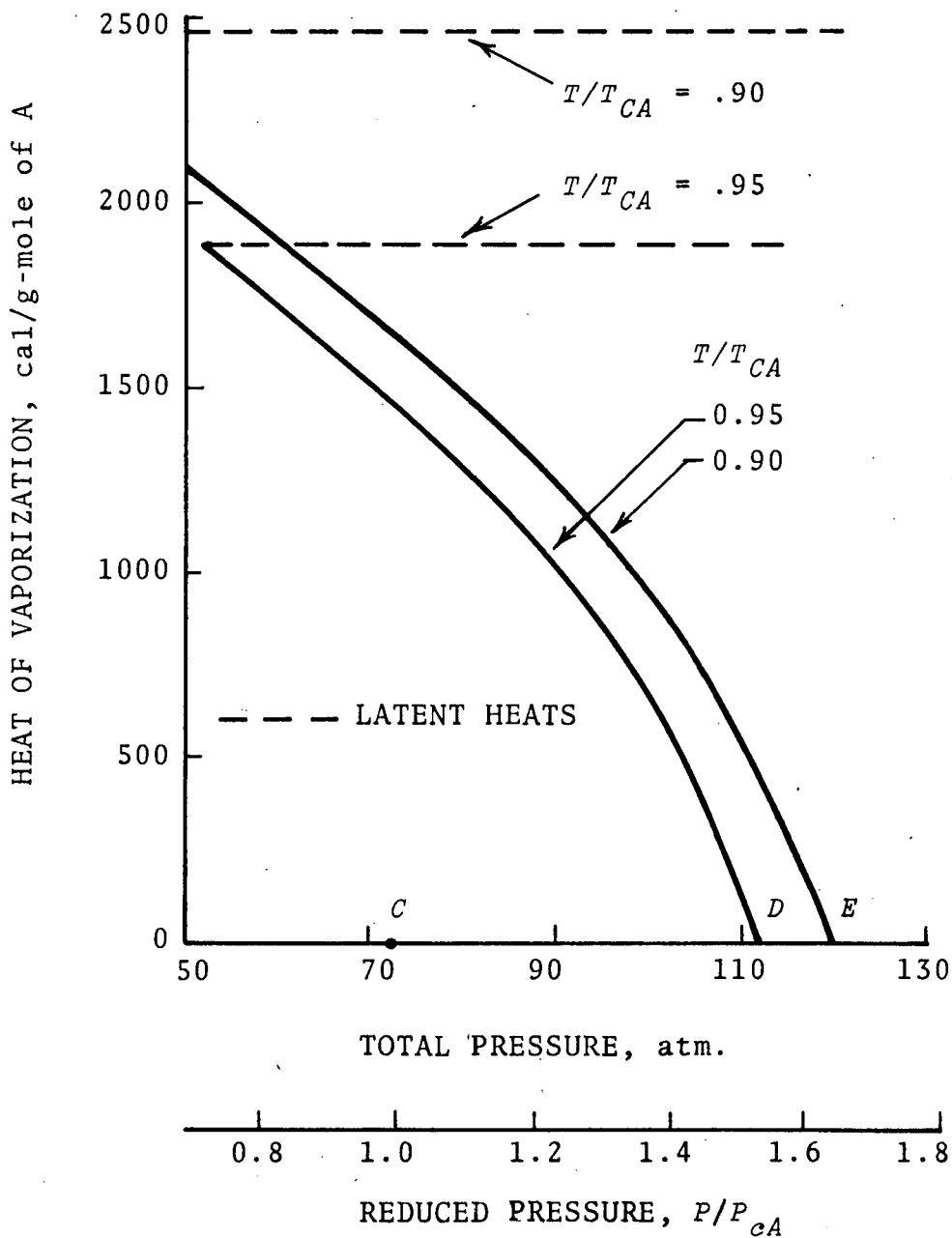


Figure 3. Isothermal difference in the partial molal enthalpies of carbon dioxide as a function of total pressure.

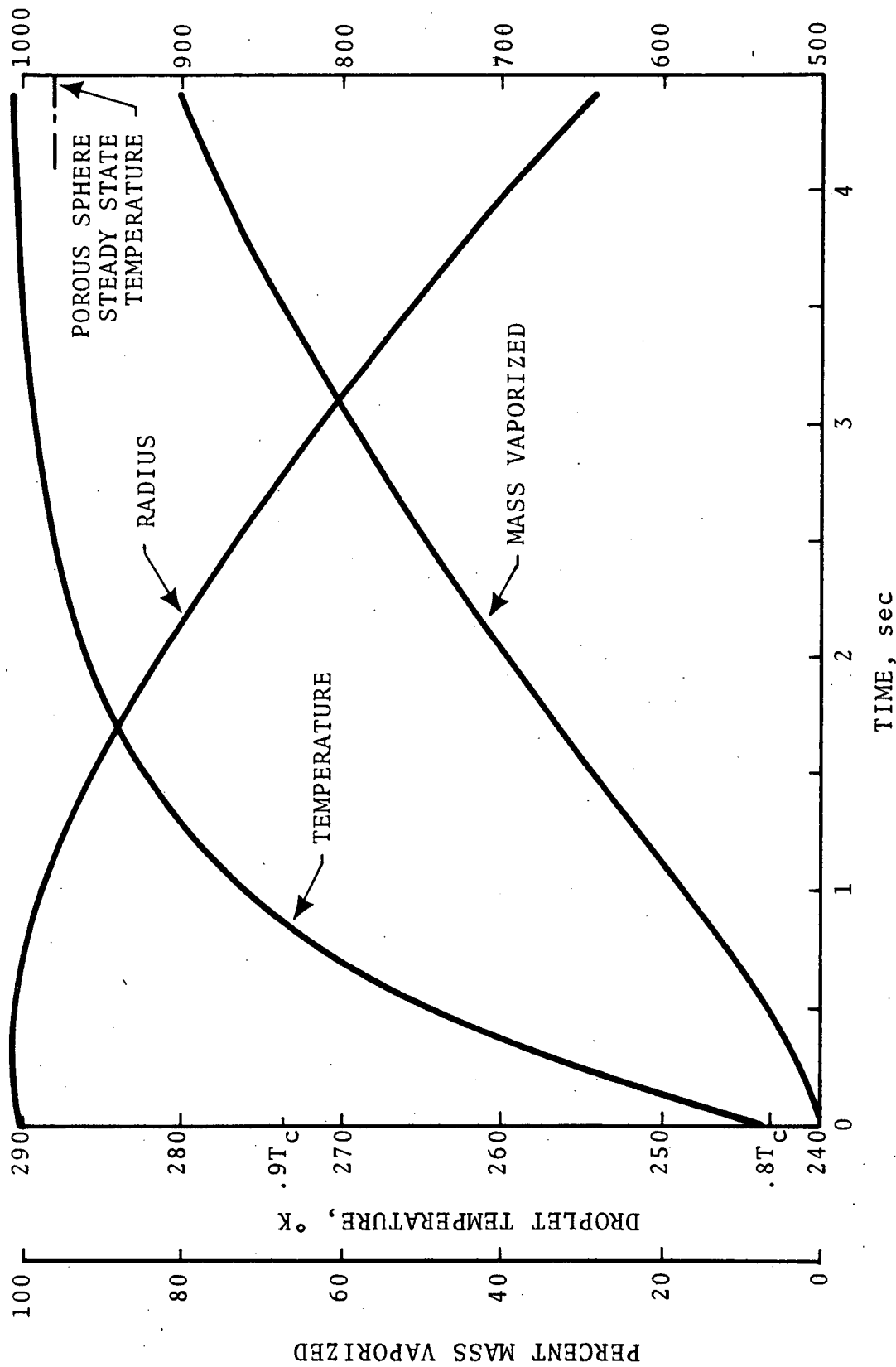


Figure 4. Vaporization history of a CO₂ droplet vaporizing in N₂ at 1400°K and 72.9 atm; $T_{\infty} = 1400^{\circ}\text{K}$, $P_{CA} = 72.9 \text{ atm}$.

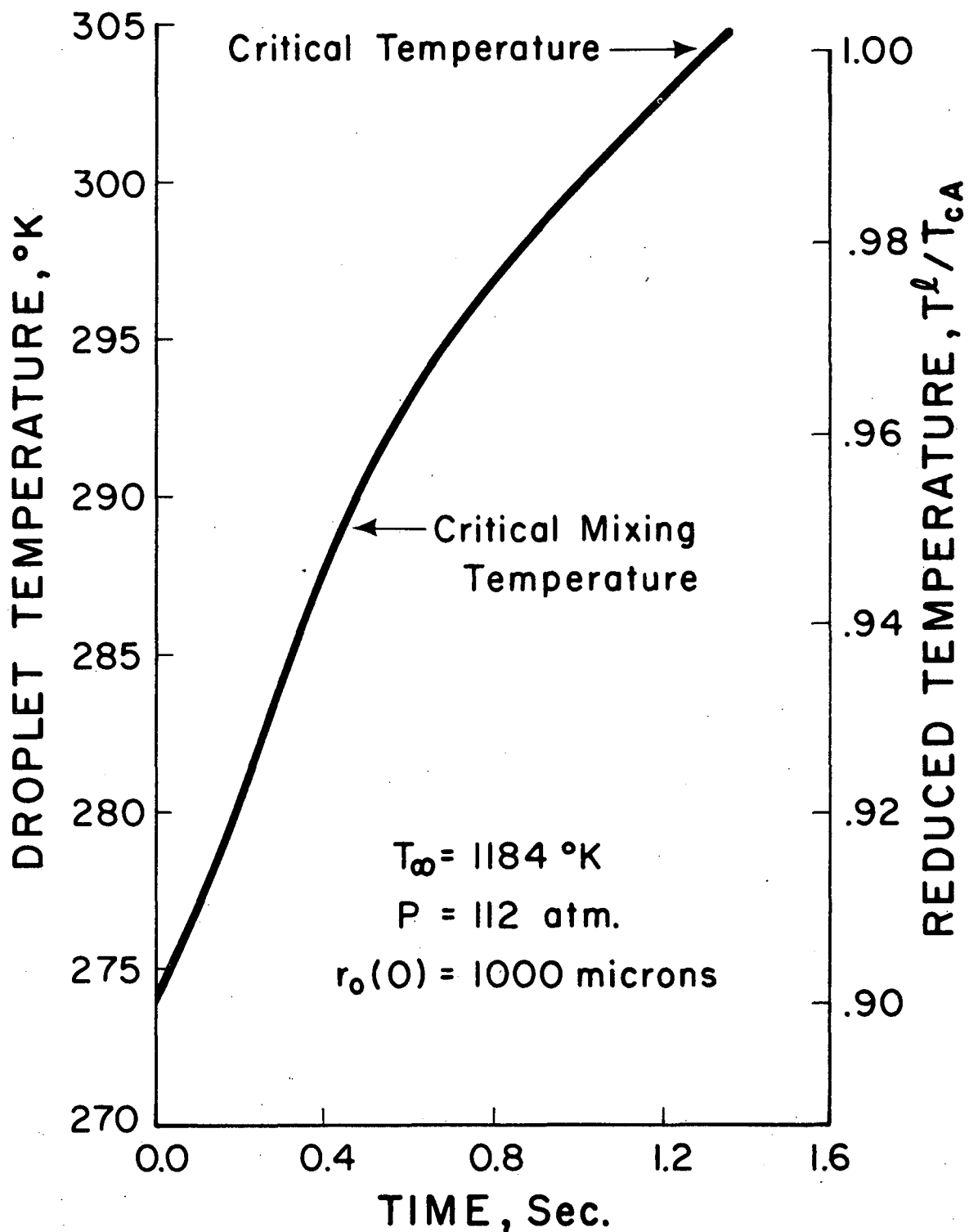


Figure 5. Temperature response of a CO_2 droplet vaporizing in N_2 at 1184°K and 112 atmospheres.

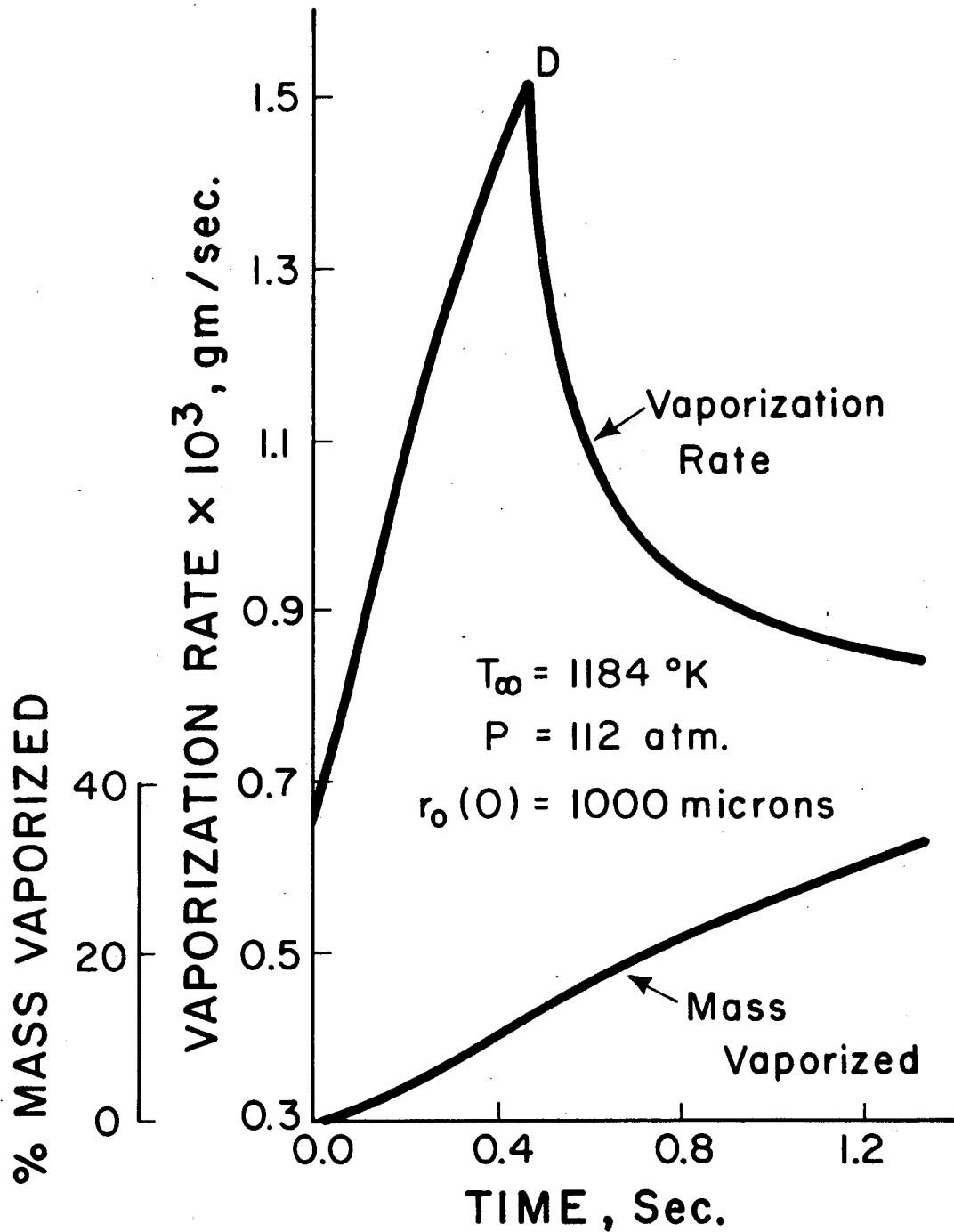


Figure 6. Mass vaporization rate and percent-mass-vaporized curves for the same conditions as shown on Figure 5.

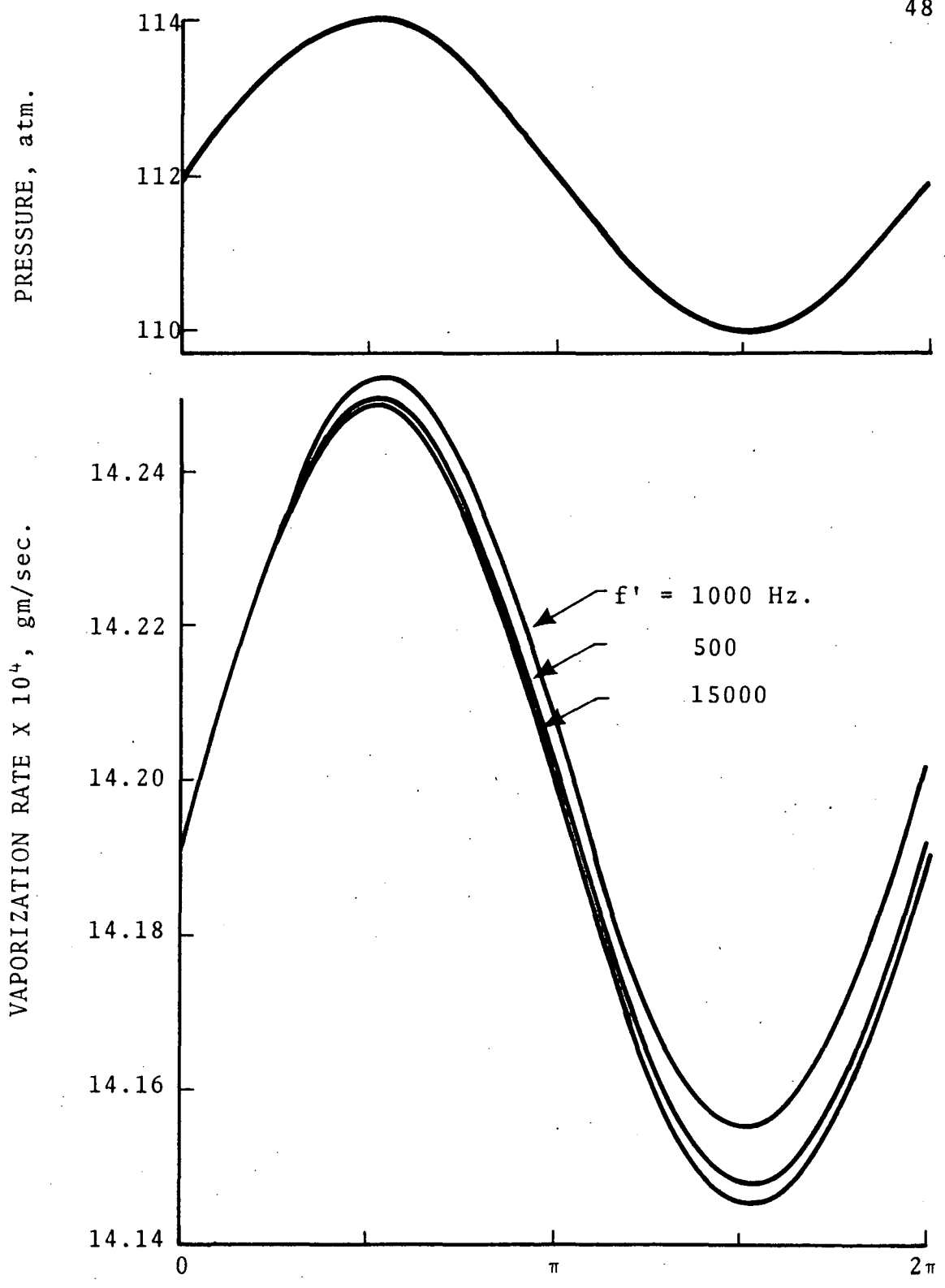


Figure 7. Effect of frequency upon the mass vaporization rate $T^l = 287^\circ K$, $\bar{T}_\infty = 1184^\circ K$, $r_o = 994\mu$.

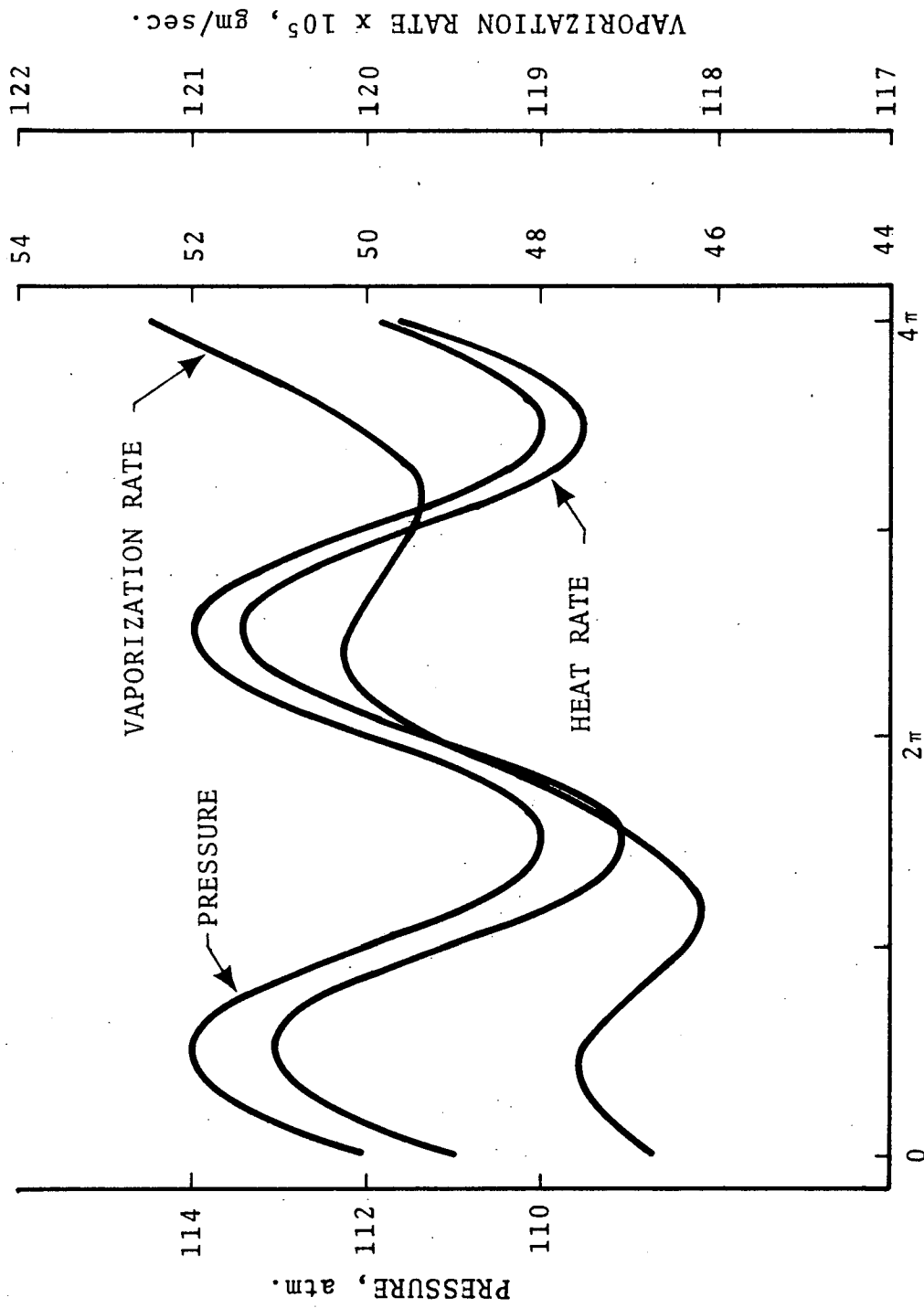


Figure 8. Response of a CO_2 droplet vaporizing in N_2 . $T^\infty = 291.8^\circ\text{K}$, $f' = 1000$ Hz, $\bar{T}_\infty = 1184^\circ\text{K}$, $r_0 = 986$ microns.

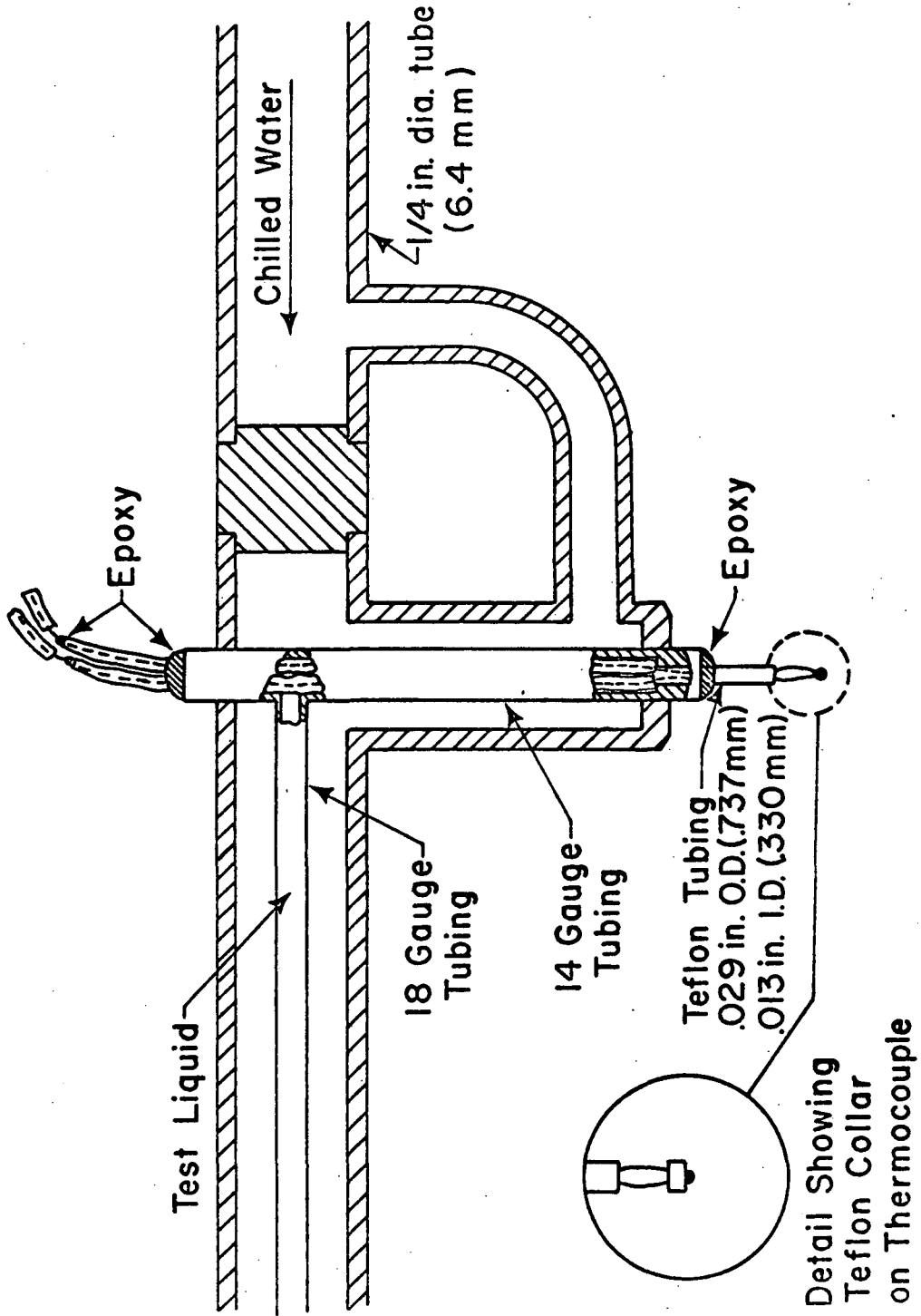


Figure 9. Cross-section of probe subassembly for SDA.

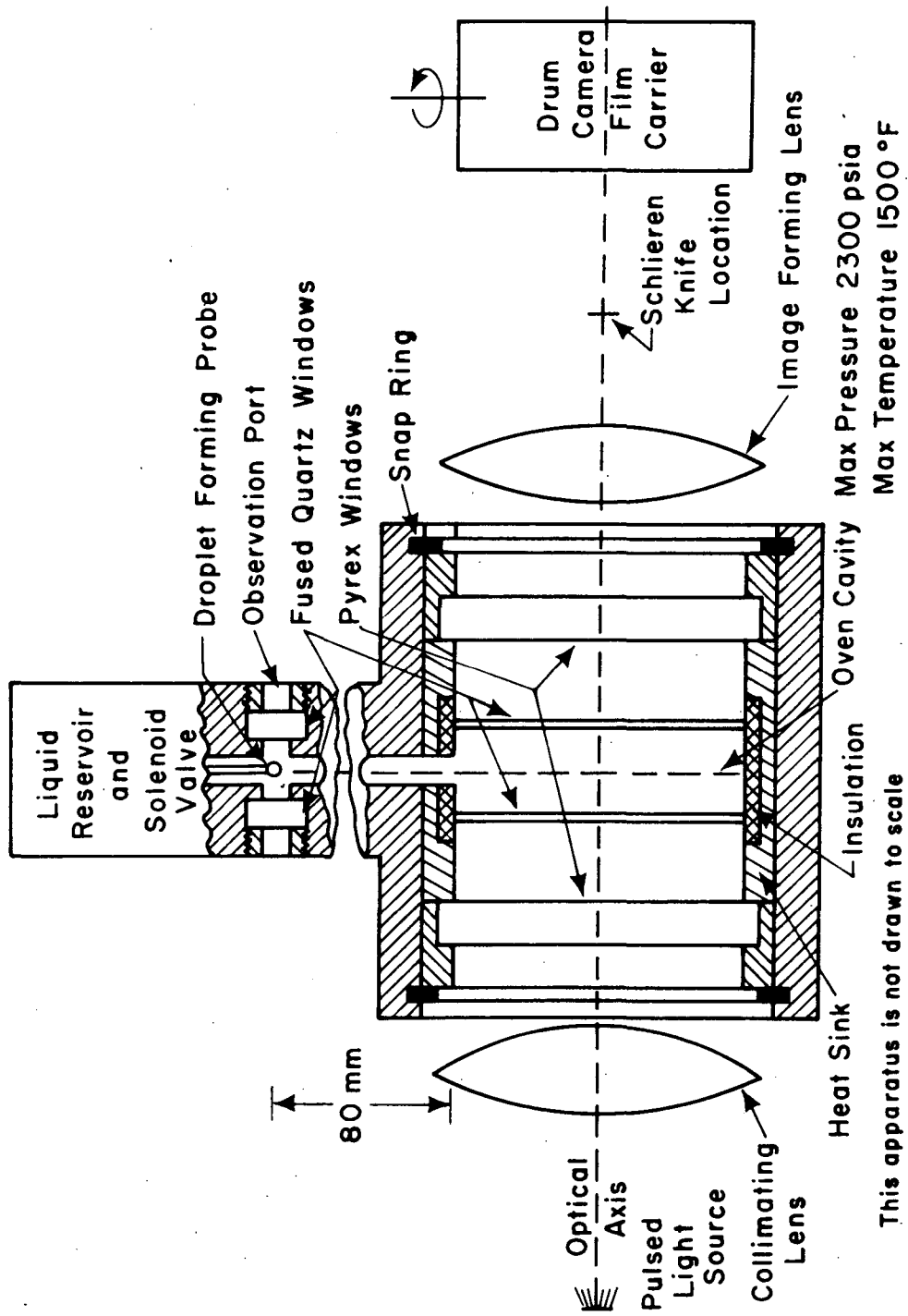


Figure 10. Schematic diagram of the falling drop apparatus.

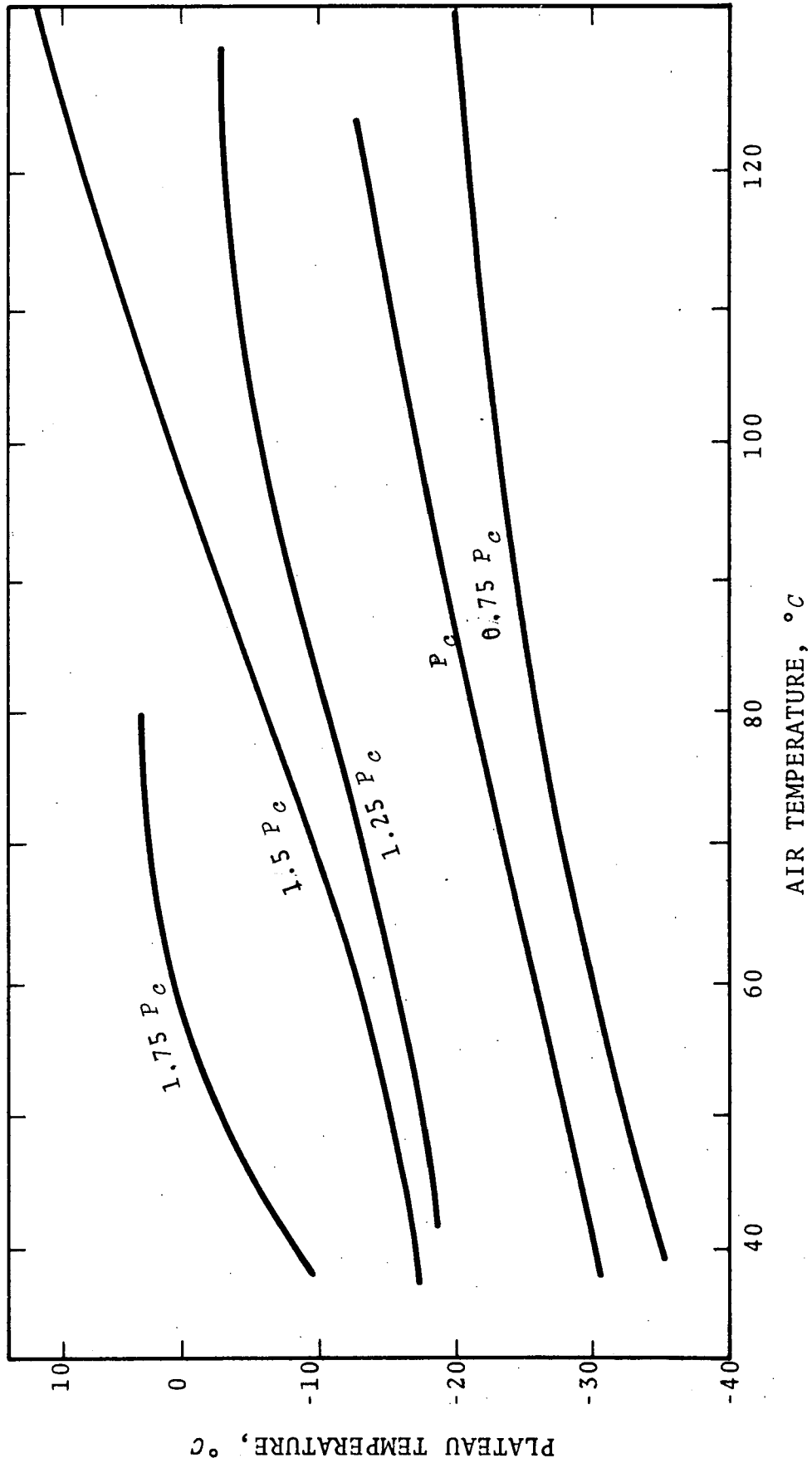


Figure 11. Summary of Freon-13 temperature data for various pressures.

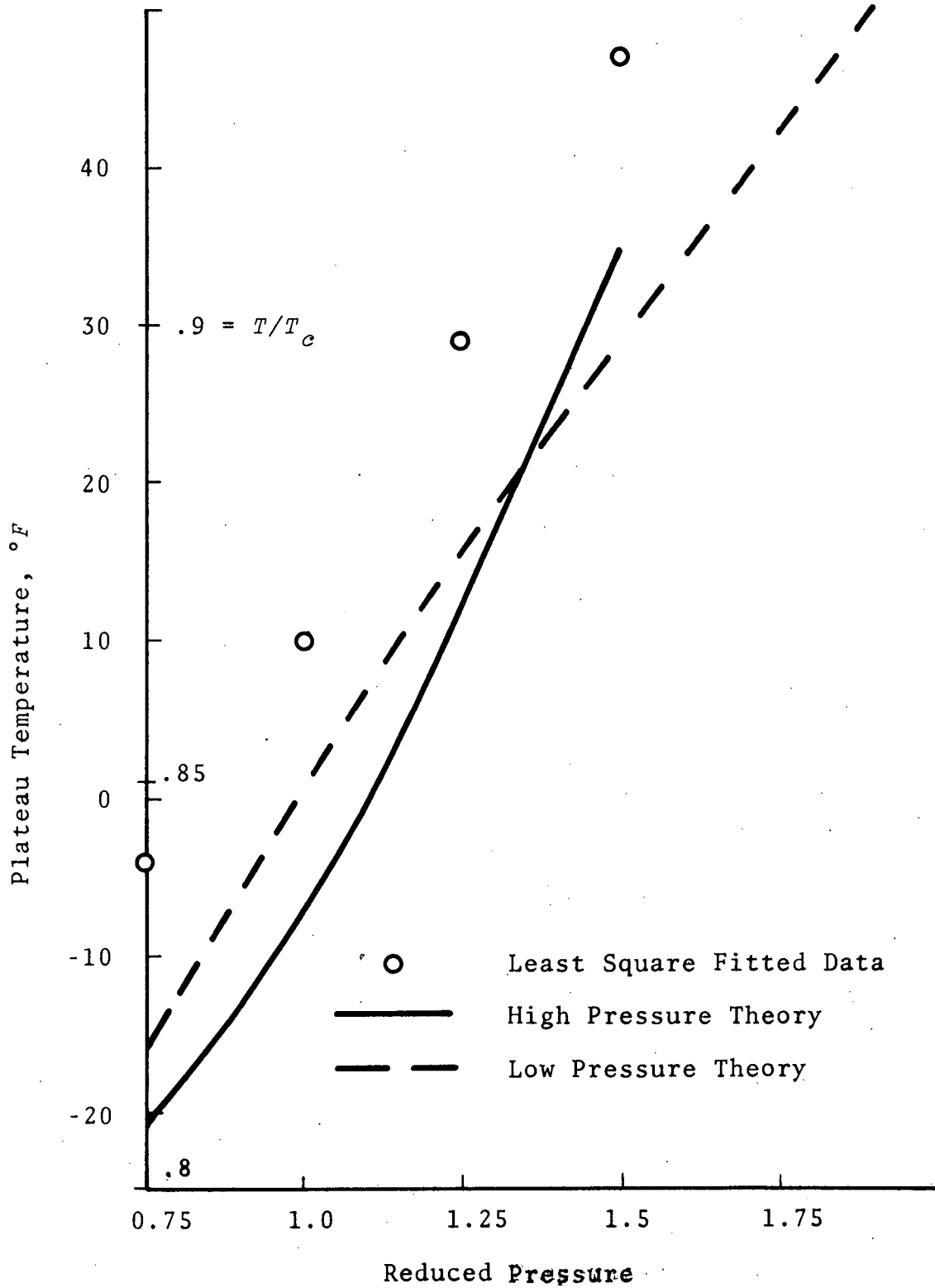


Figure 12. Summary of Fr-13 Temperature Data. Shown vs. pressure for air temperature of 250°F (394°K).

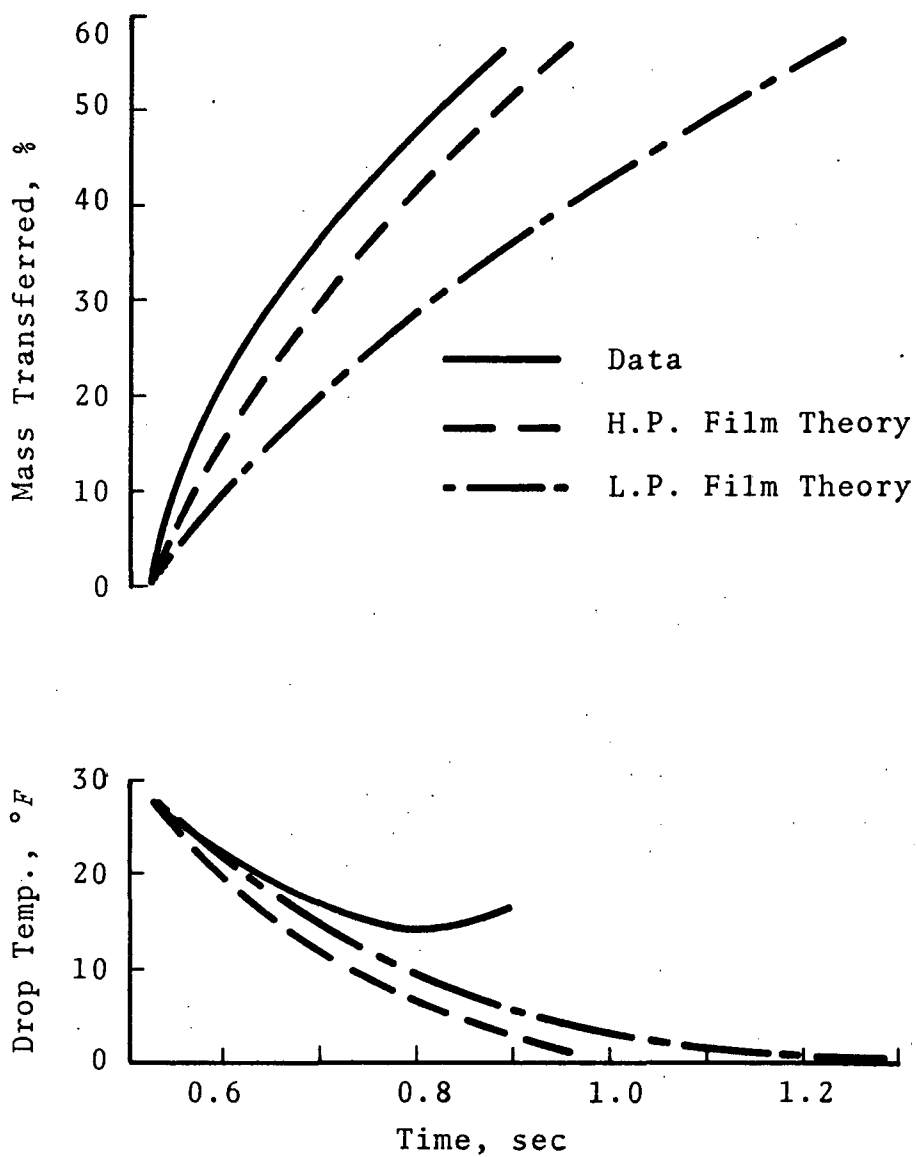


Figure 13. History of Fr-13 drop vaporizing in air at $1.25 P_c$ and $171.5^\circ F$ ($350^\circ K$). Air velocity = 3.37^c in./sec., initial mass = 2.4×10^{-6} lbm.

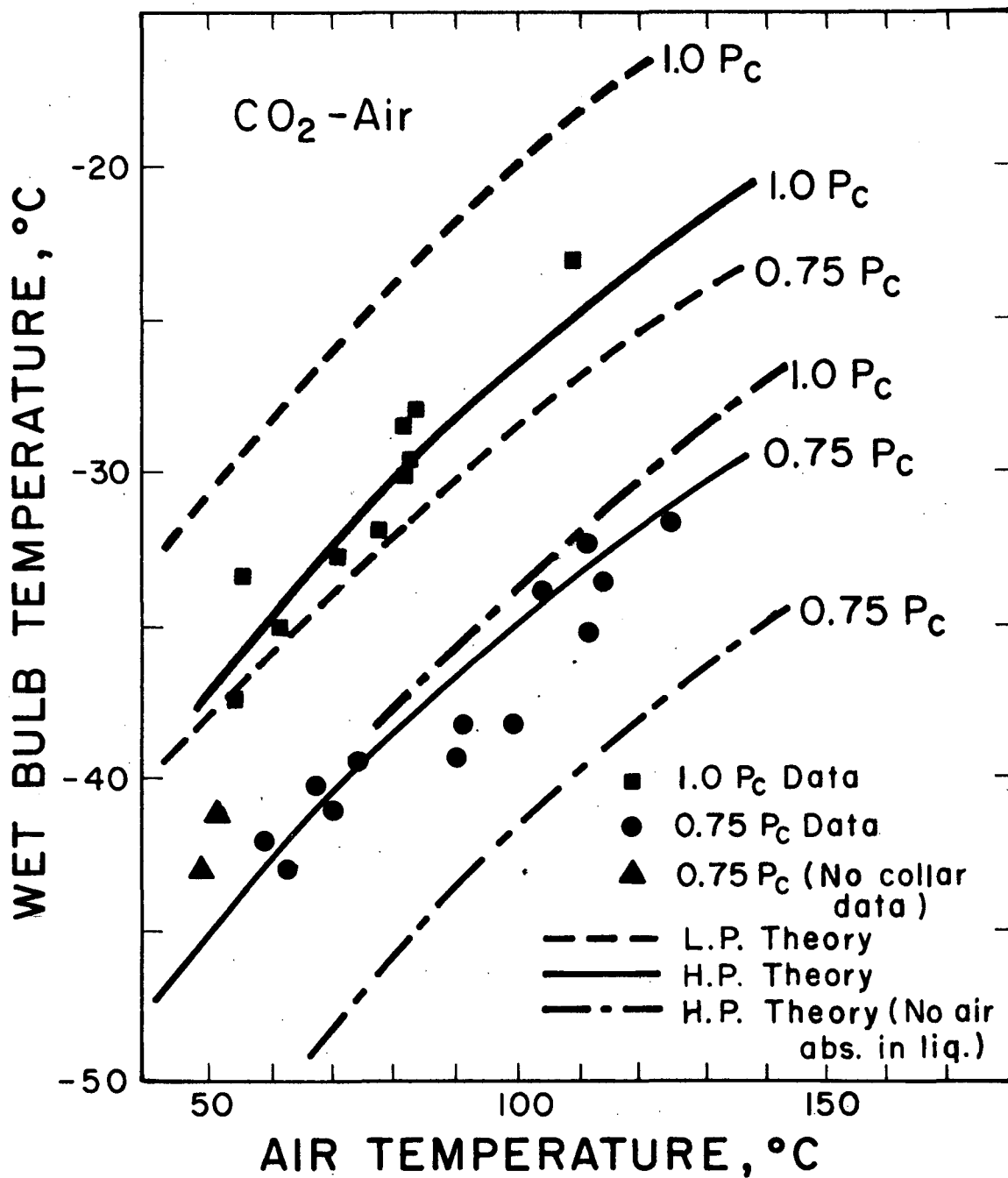


Figure 14. Steady state temperature versus air temperature for CO₂ at two pressures.

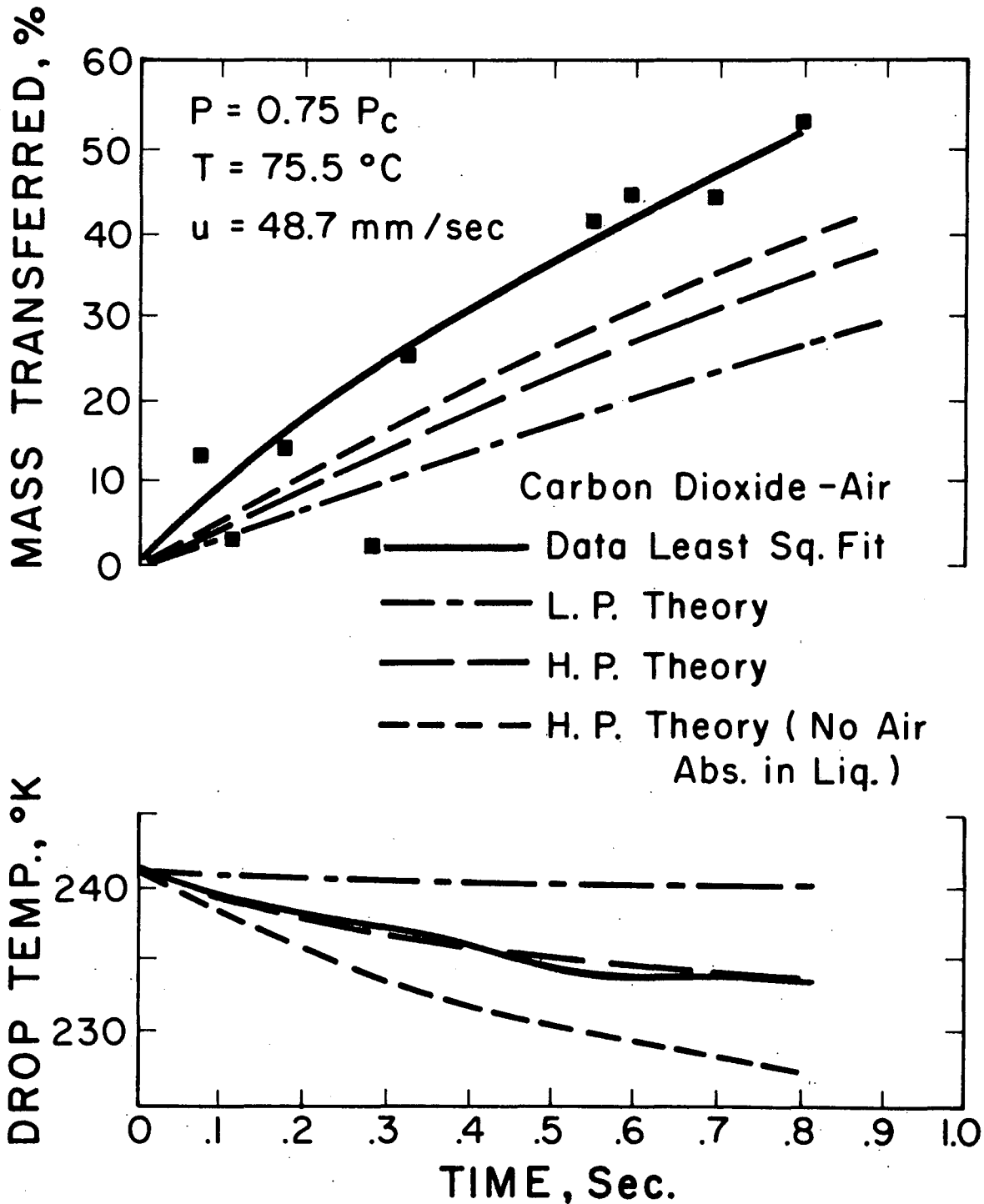


Figure 15. Percent-mass-transferred and droplet temperature histories for CO₂ and 0.75 P_c and 349°K air.

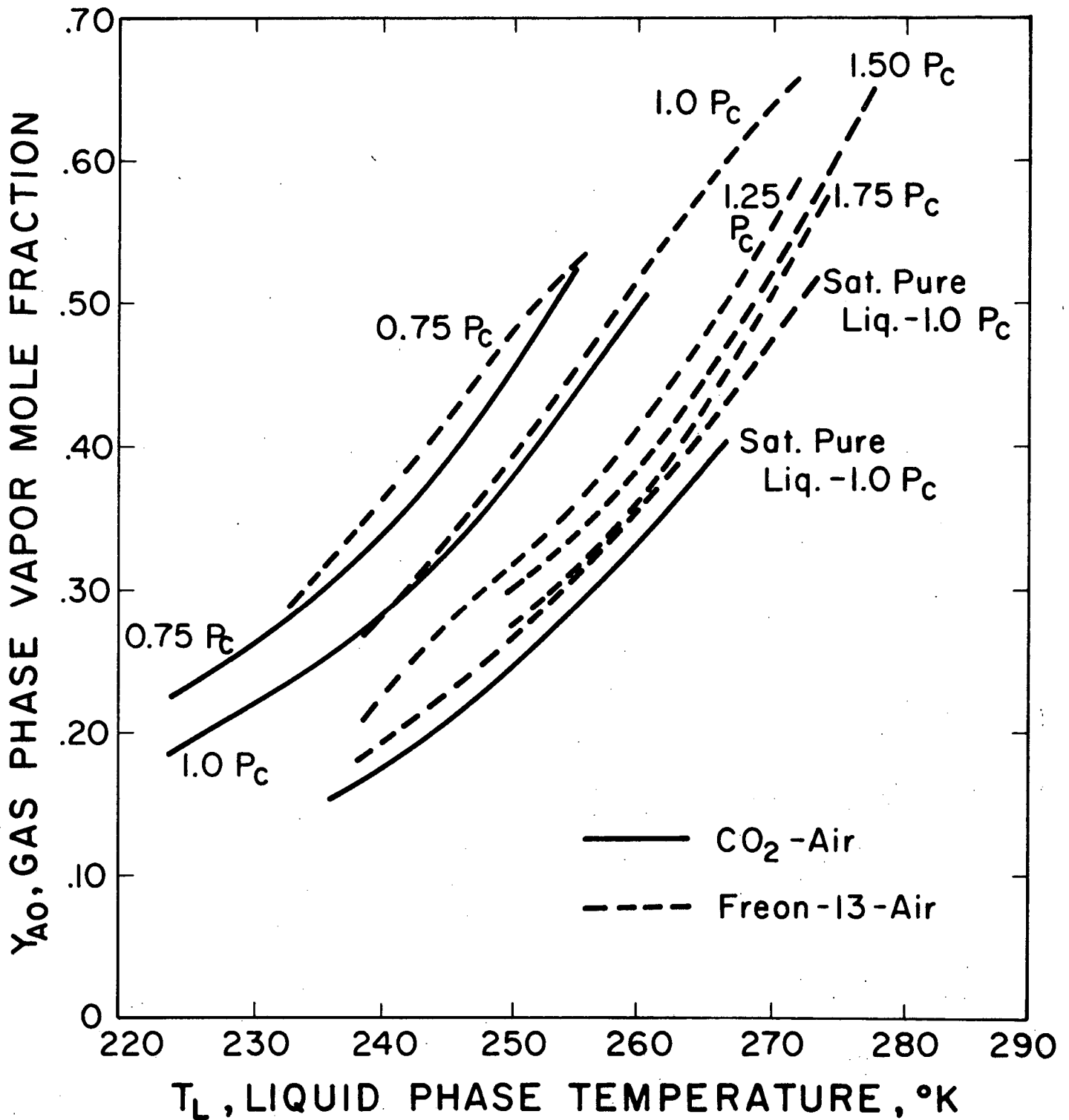


Figure 16. Gas phase mole fractions for CO_2 and Freon-13 in air versus temperature for various pressures.

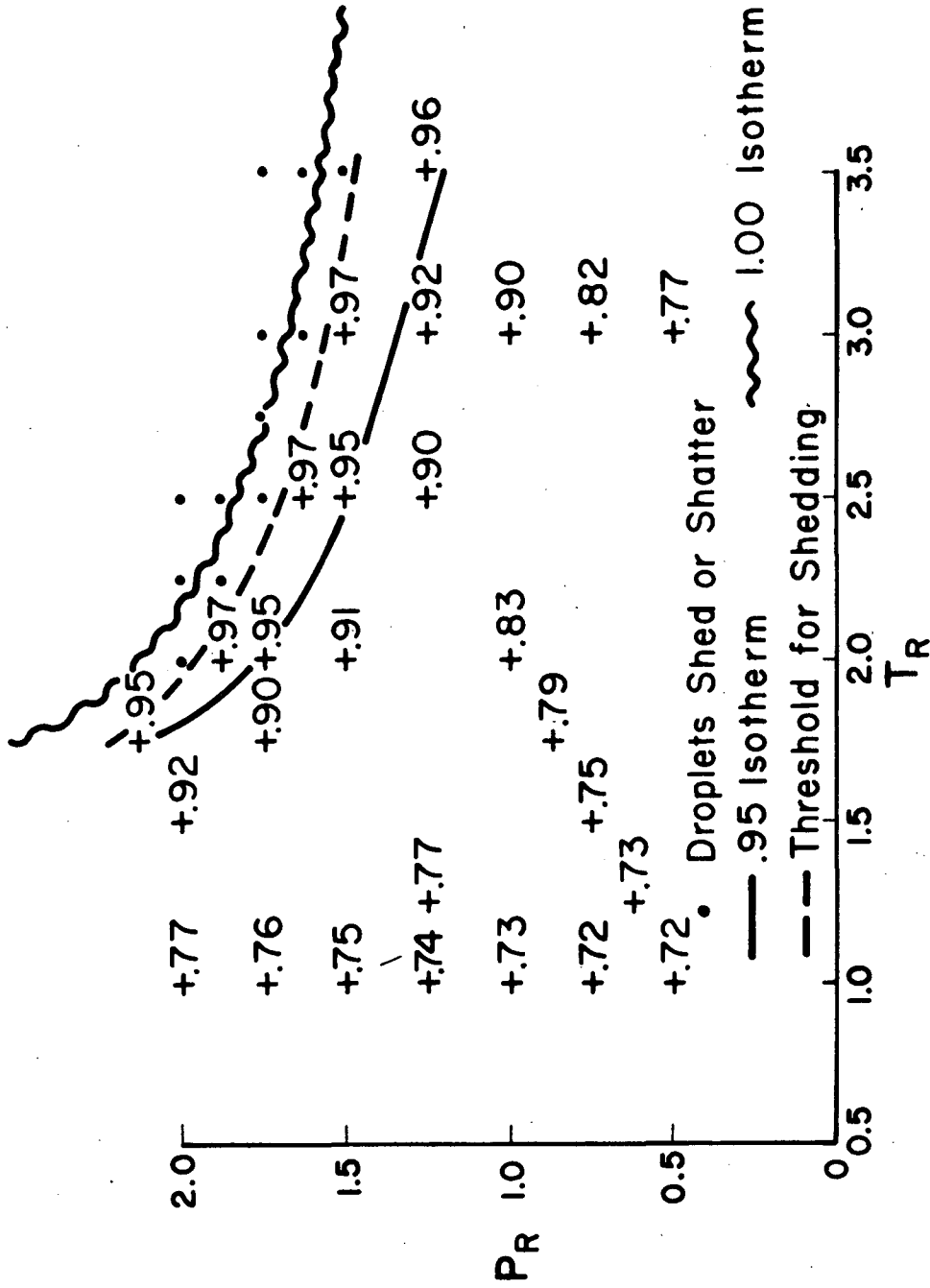


Figure 17. Experimental steady state droplet temperatures from the period of oscillation of droplets falling through helium.

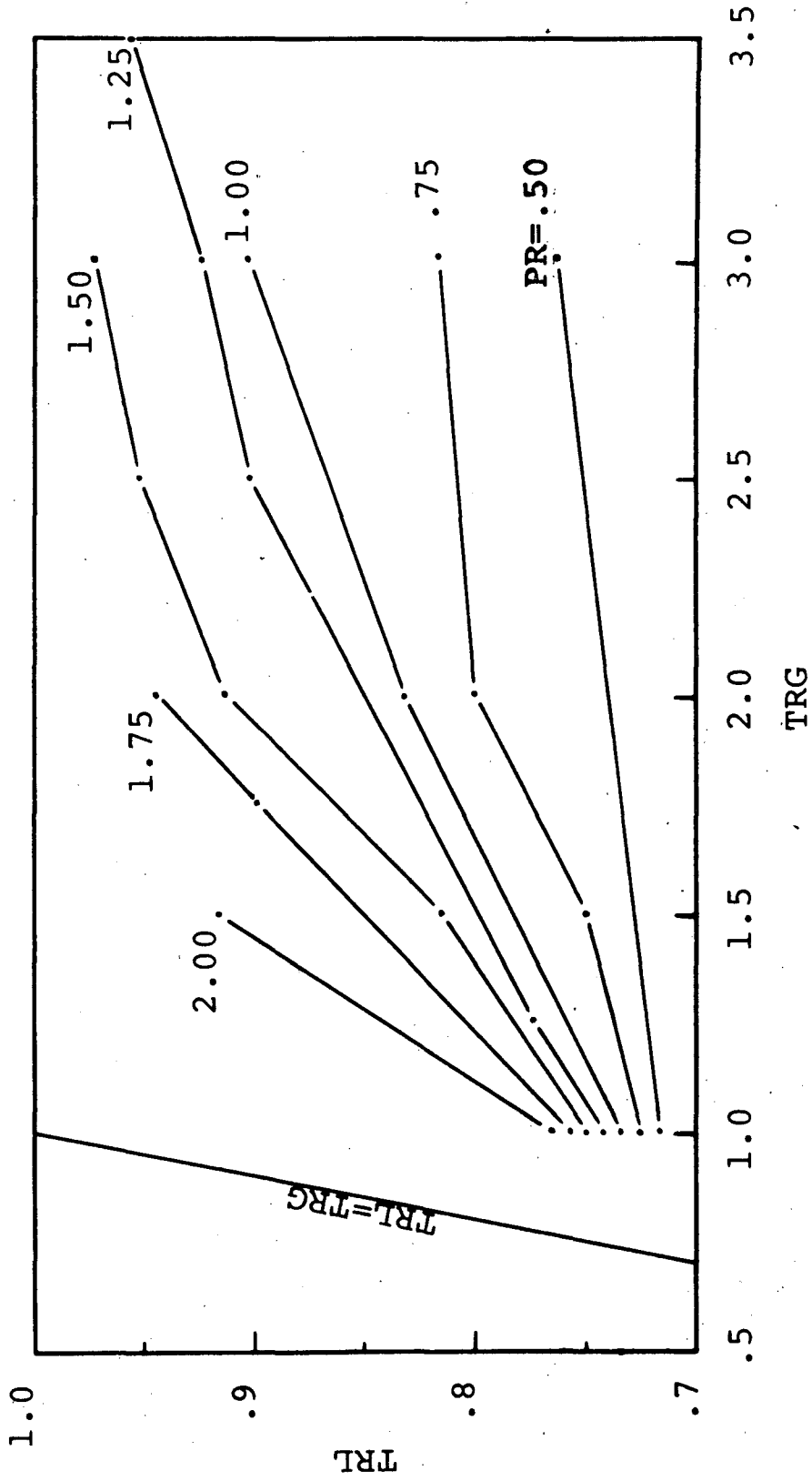


Figure 18. Experimental steady state droplet temperatures obtained from the period of oscillation of carbon dioxide droplets falling through helium.

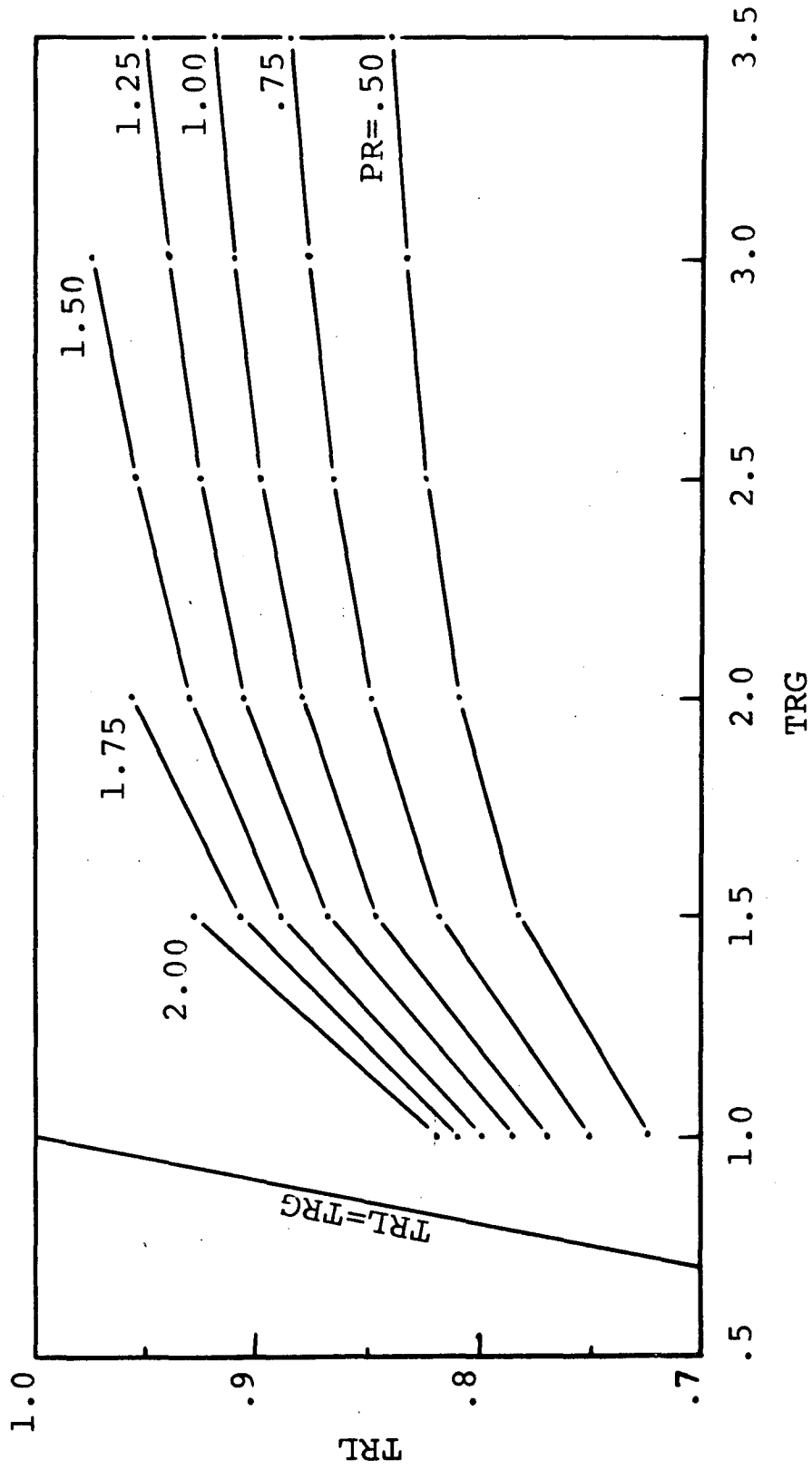


Figure 19. Steady state droplet temperatures calculated from the film theory for .05 cm diameter carbon dioxide droplets falling through helium at a velocity of 120 cm/sec.

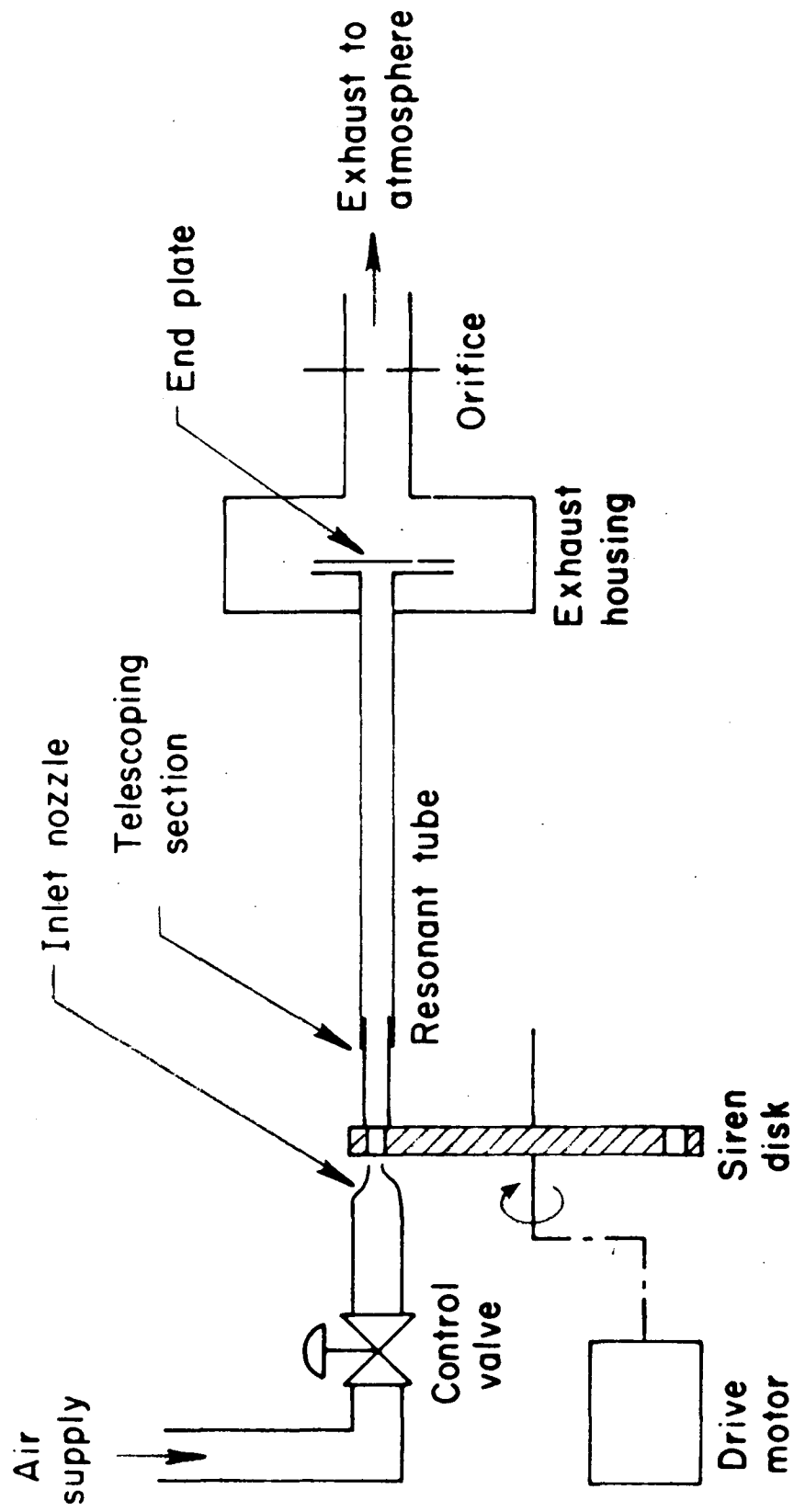


Figure 20. Schematic diagram of experimental apparatus for the PST.

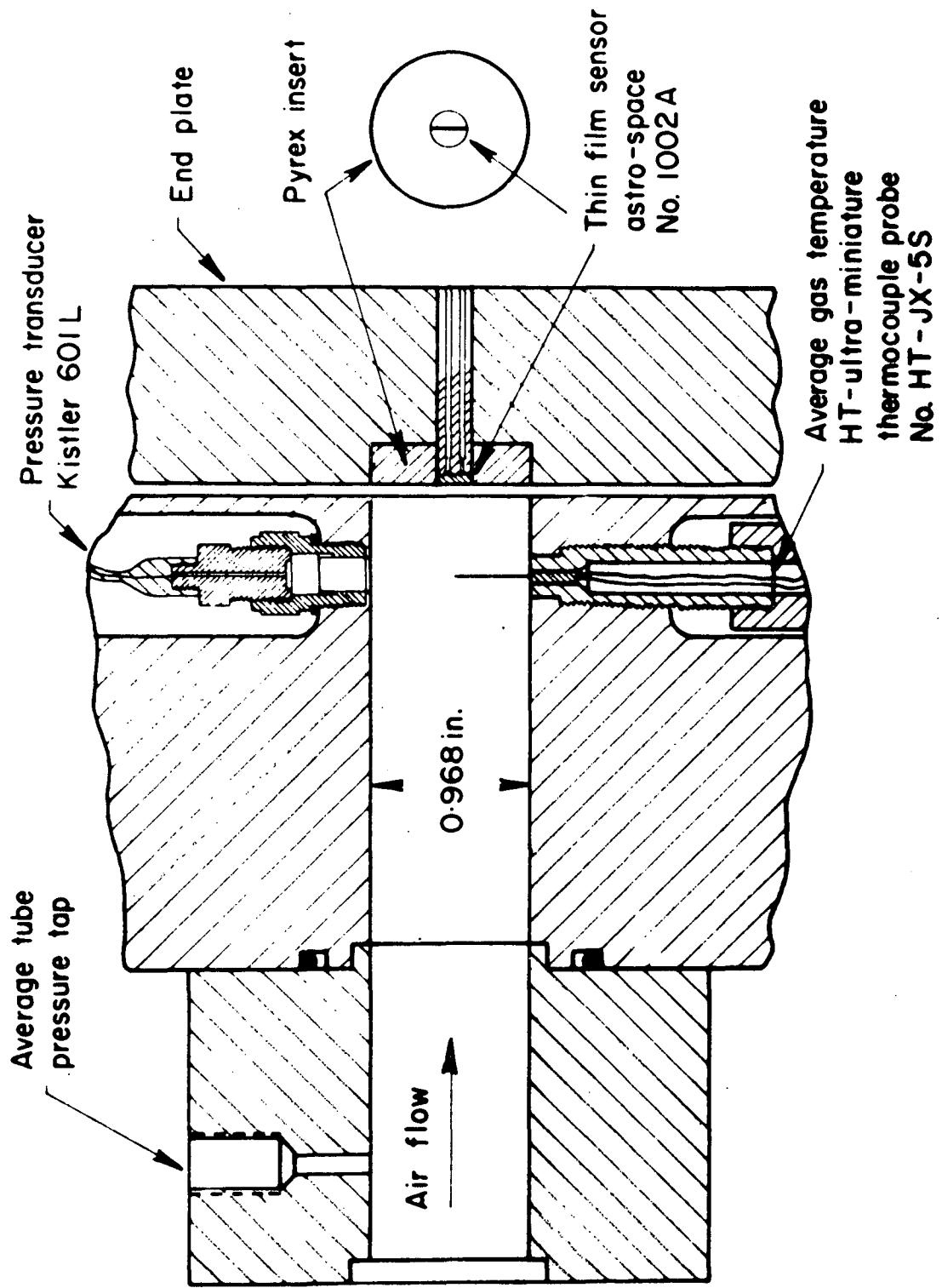


Figure 21. Test Section Instrumentation for PST.

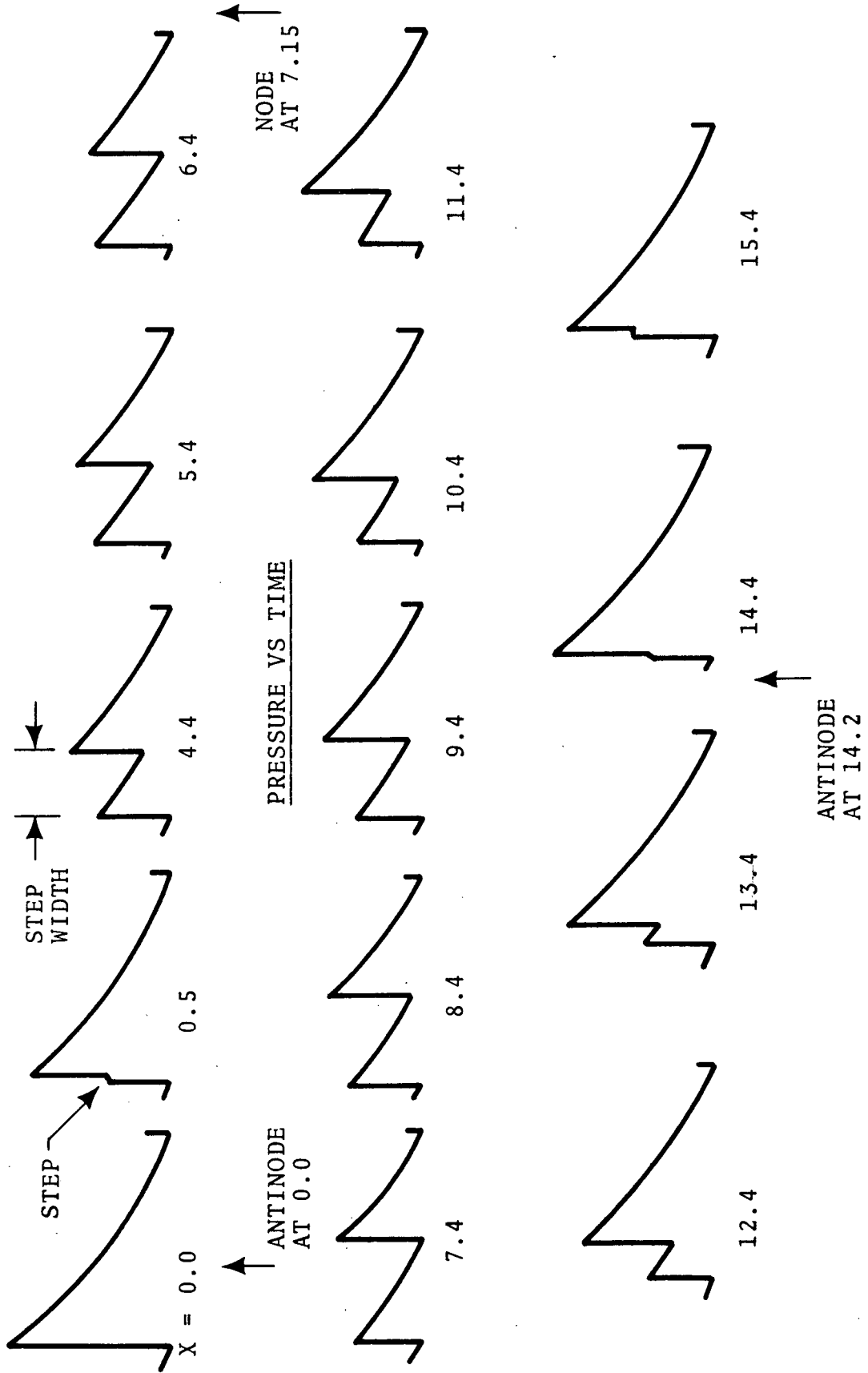


Figure 22. Pressure shapes at various locations in the tube near the test plate end - X distance measured in inches from the test plate.

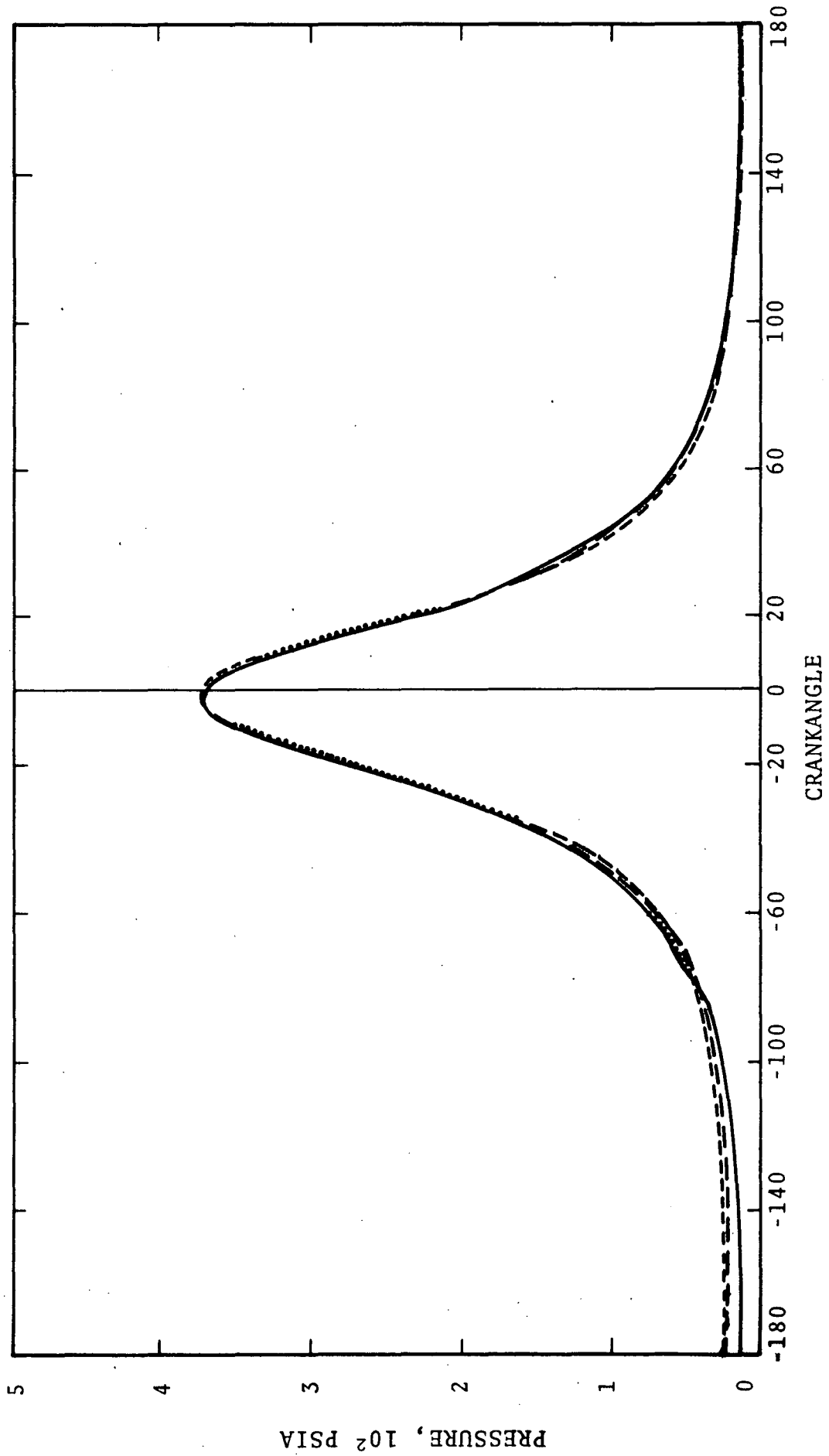


Figure 23. Experimental pressure vs. crankangle for various cycles of CPD at 3452. RPM
(57.5 Hz).

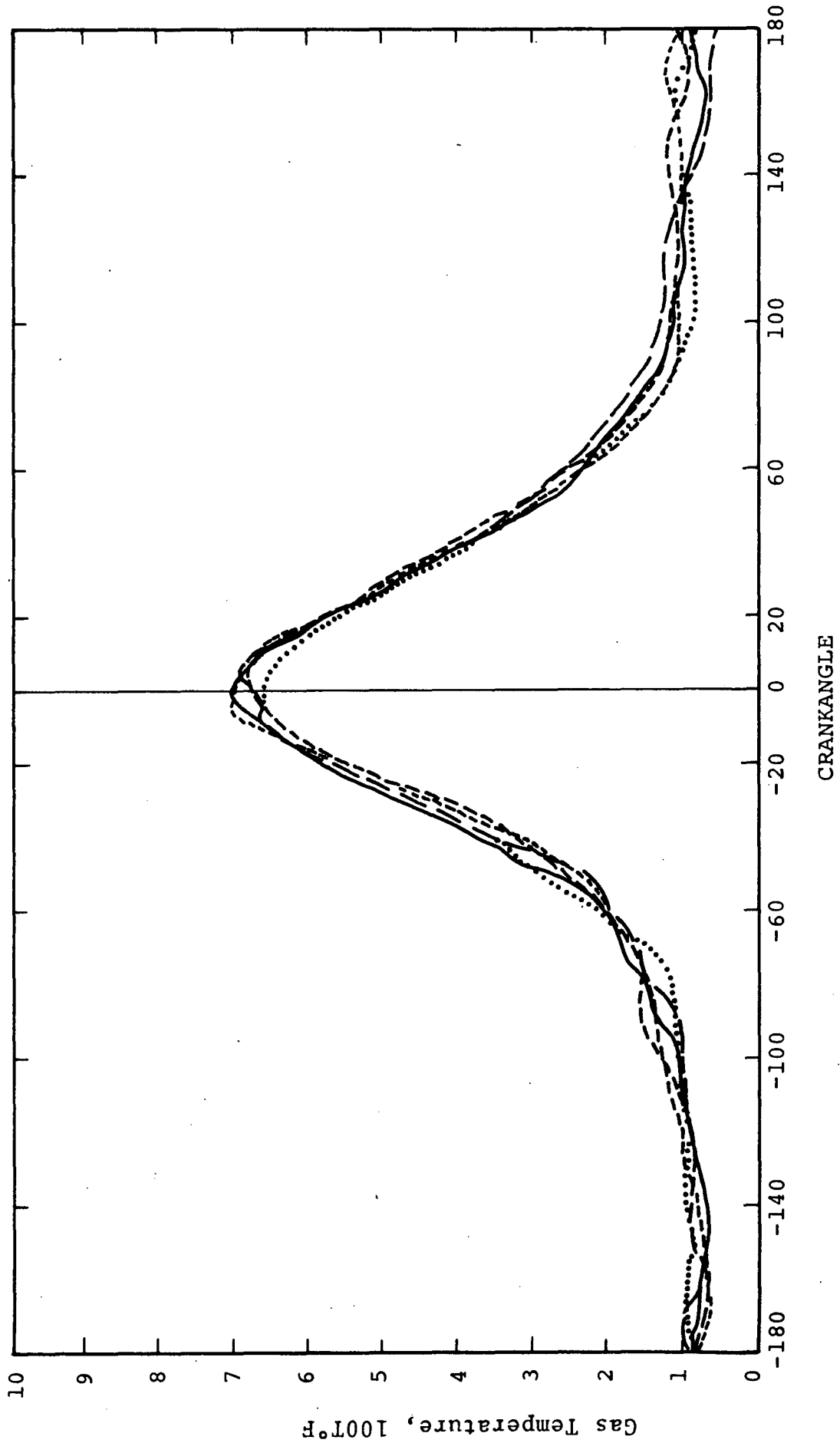


Figure 24. Experimental bulk gas temperature for various cycles of CPD at 3452 RPM (57.5 Hz)

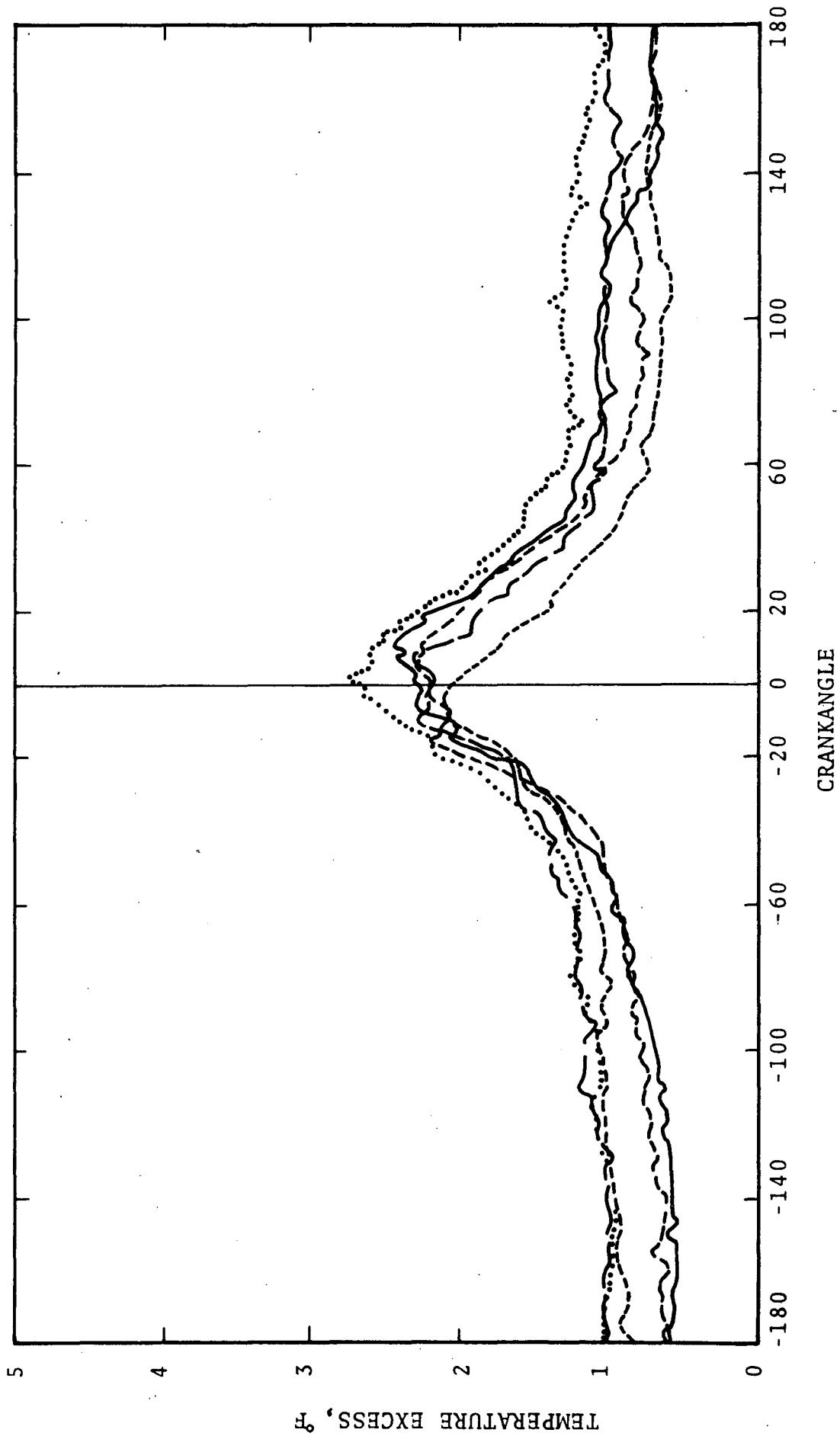


Figure 25. Variation of wall surface temperature above the base temperature of 276°F vs. crankangle for various cycles of the CPD at 3452 RPM (57.53 Hz).

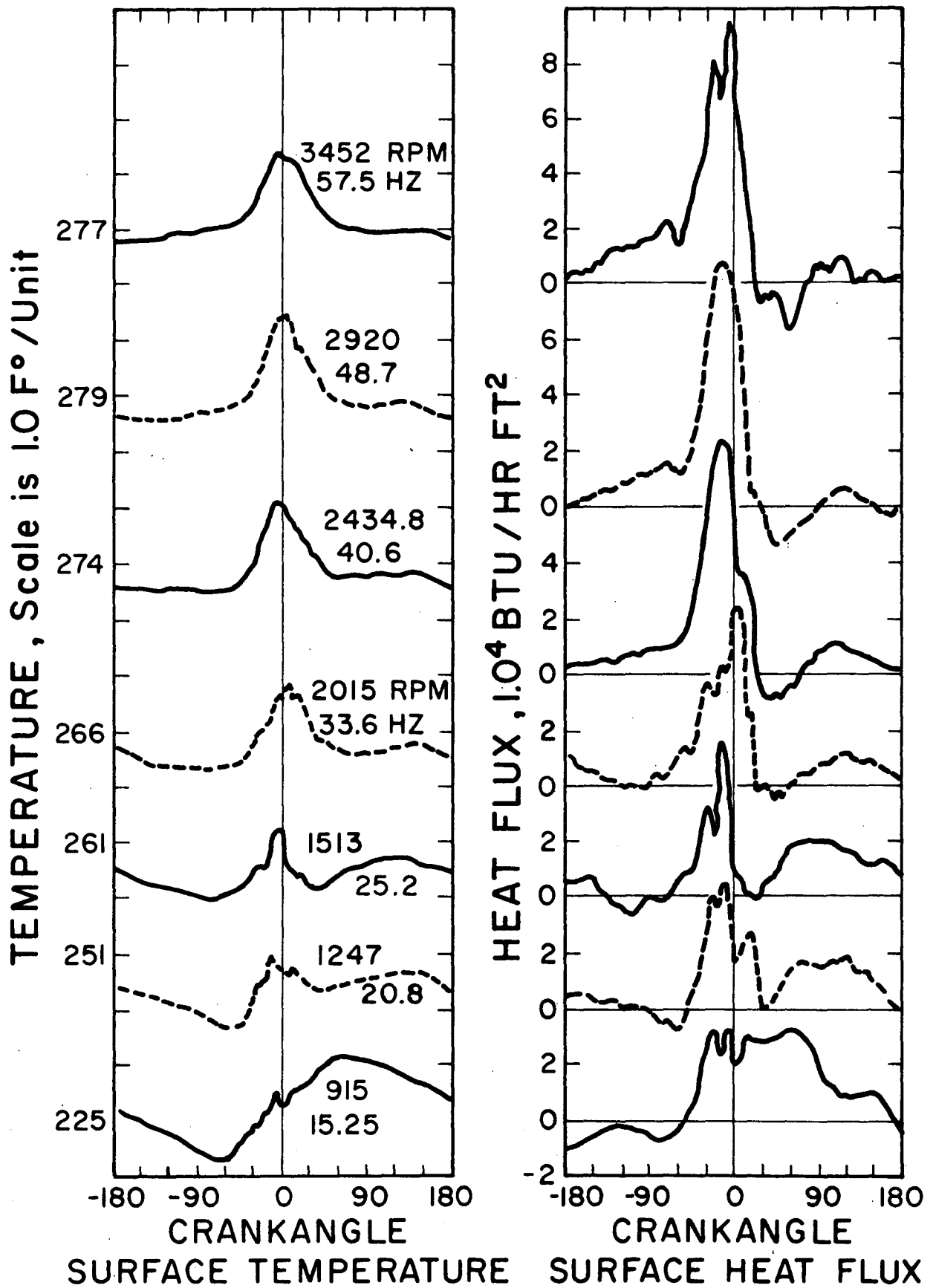


Figure 26. Experimental surface temperature and heat flux histories for various cyclic speeds of the CPD.

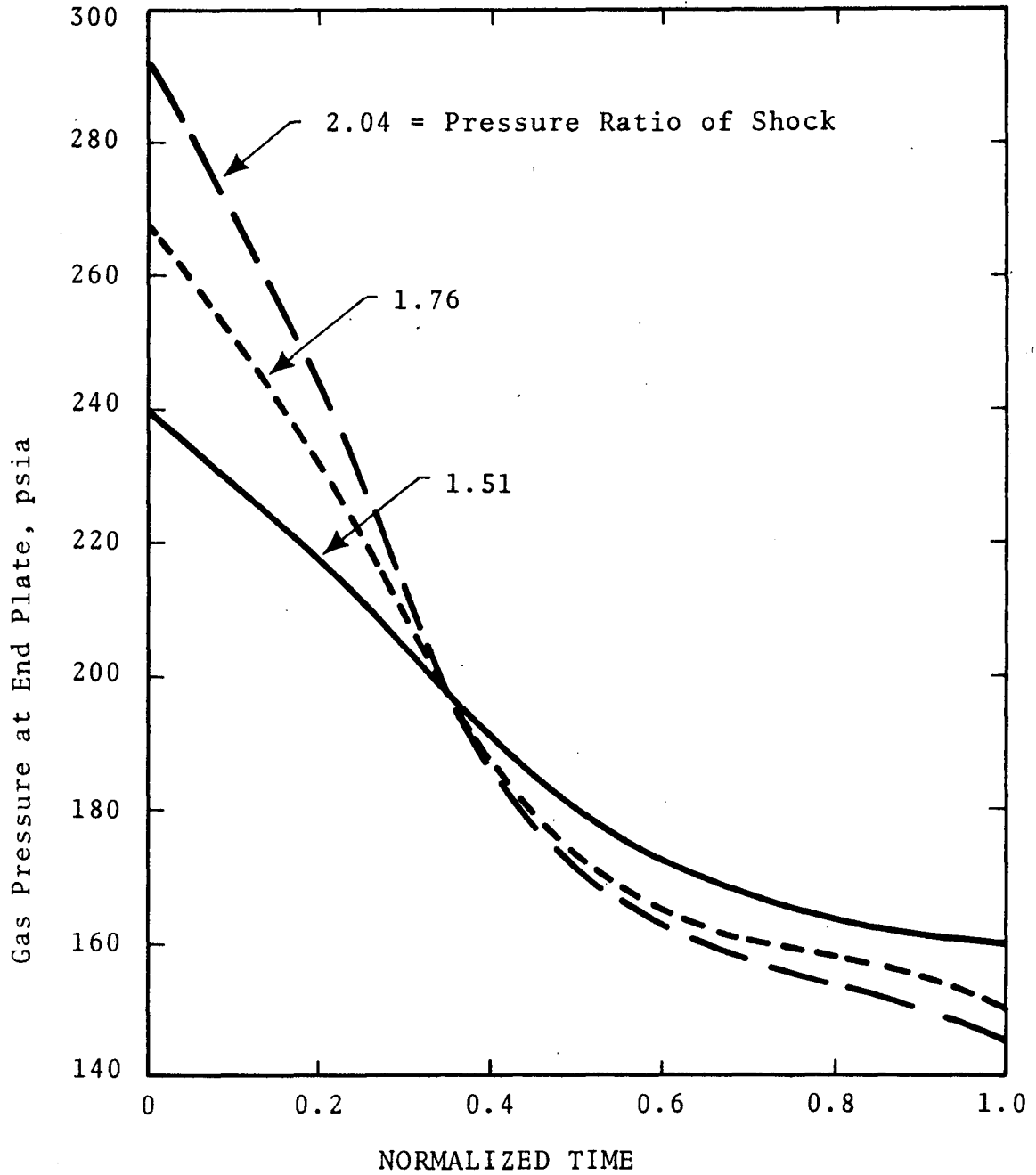


Figure 27. Experimental gas pressure oscillations PST. Frequency = 479 Hz; average tube pressure = 190 psia; tube mass flow rate = 0.133 lbm/sec.

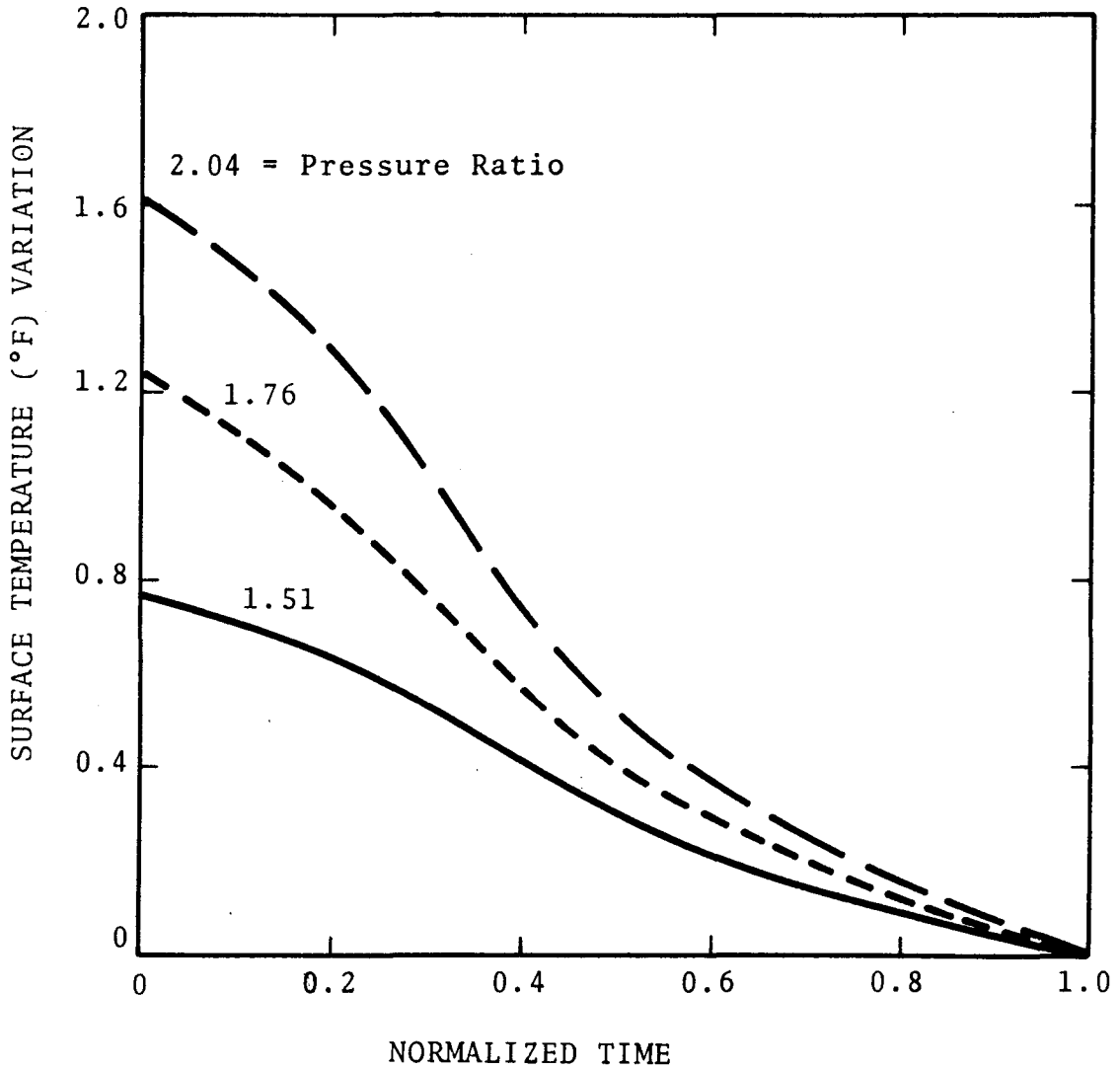


Figure 28. Experimental Surface Temperature Oscillations-PST. Same conditions as in Figure 27.

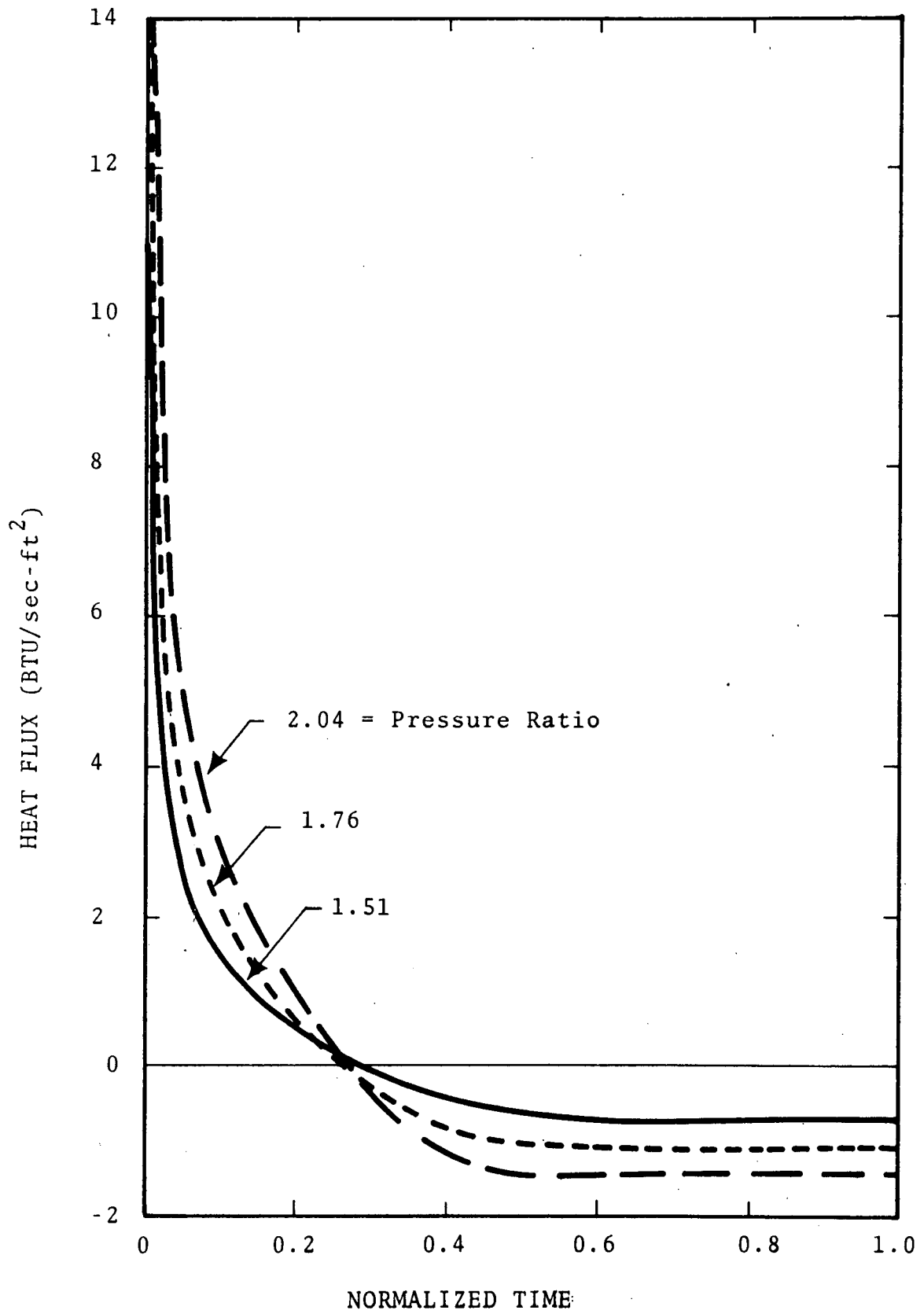


Figure 29. Experimental heat flux variation-PST. Same conditions as in Figure 27.

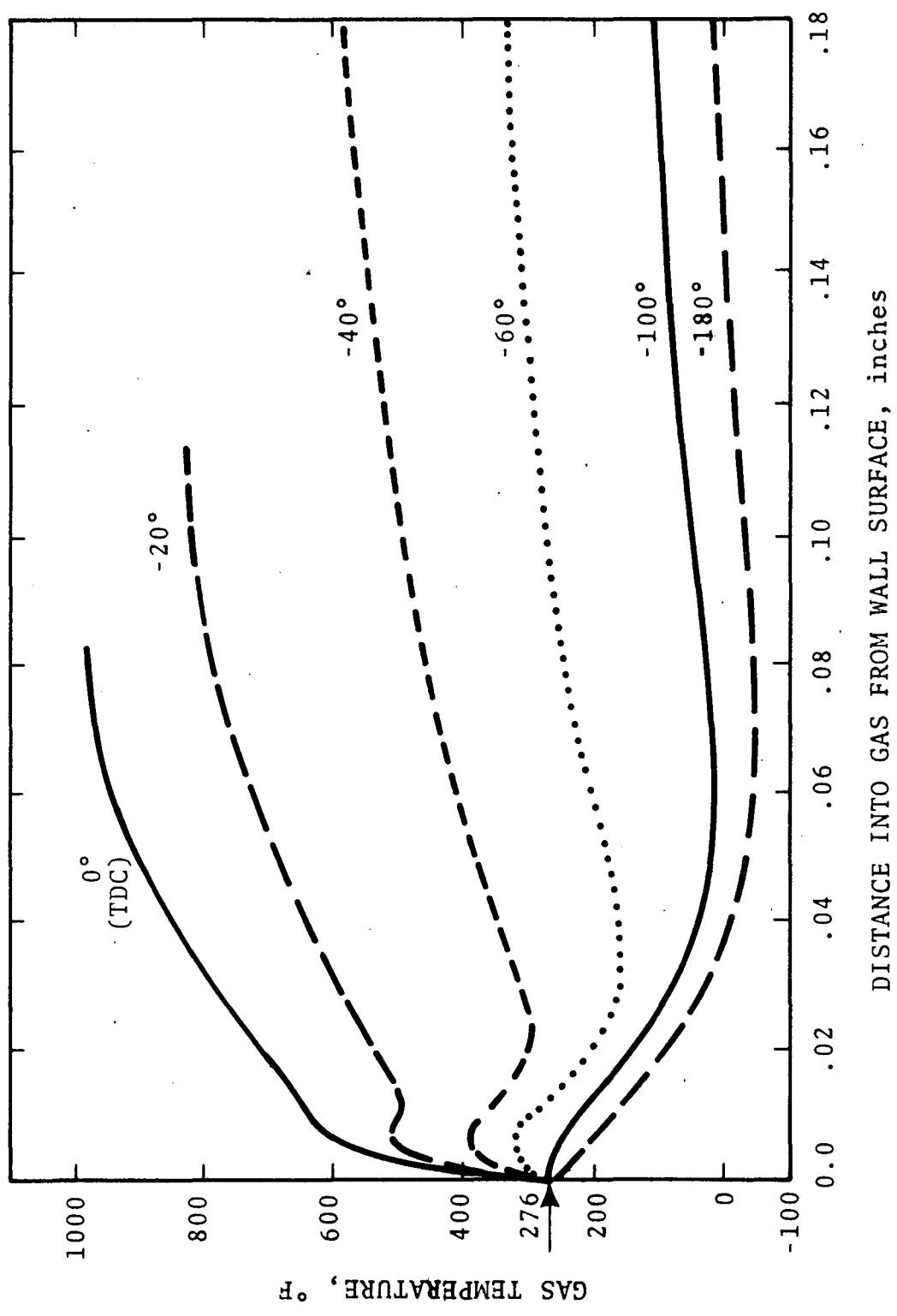


Figure 30. Gas temperature profiles during the compression stroke of the CPD at 400 RPM and 276°F wall temperature.

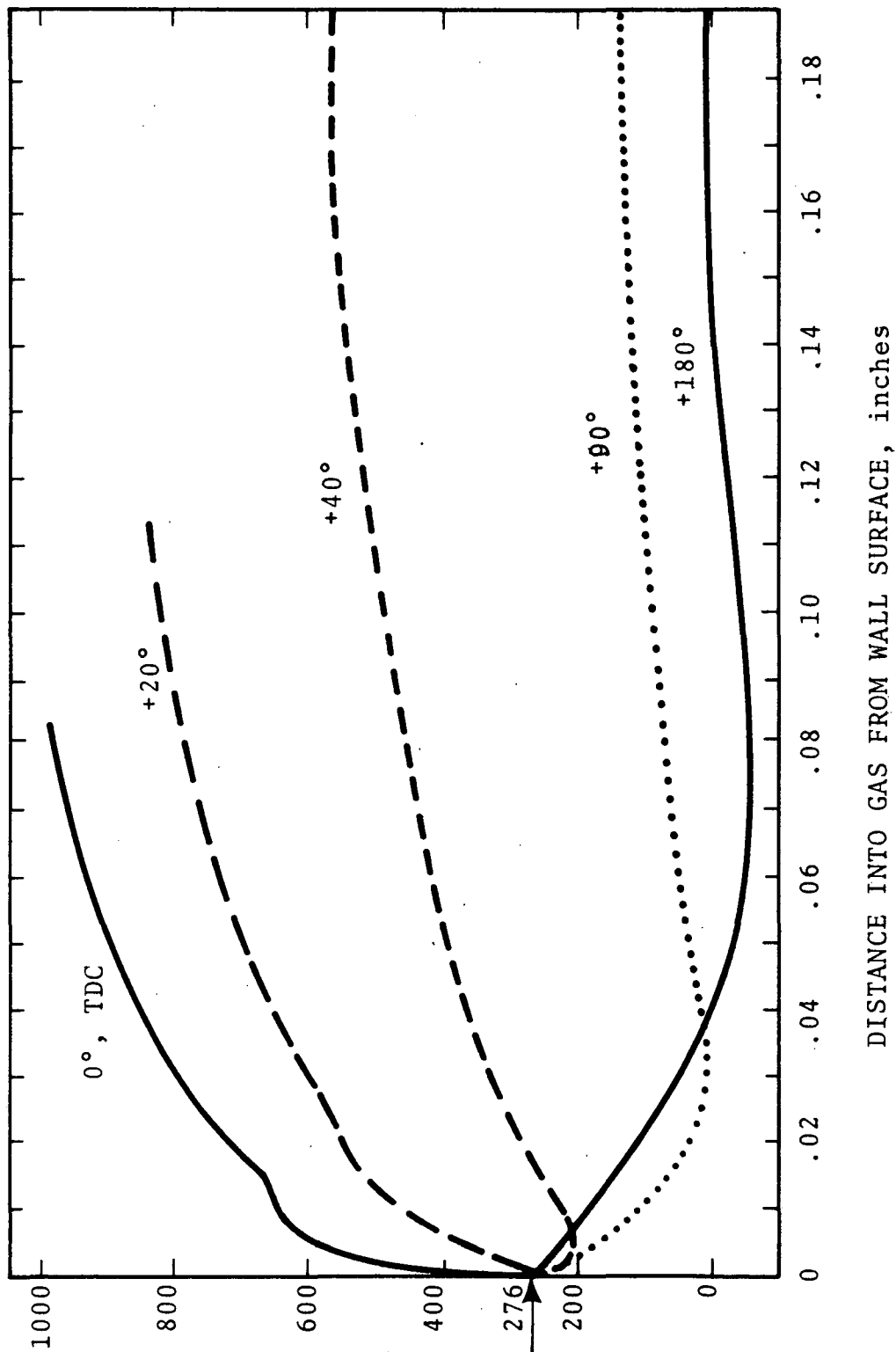


Figure 31. Gas temperature profiles during the expansion stroke of the CPD at 4000 RPM, and 276°F wall temperature.

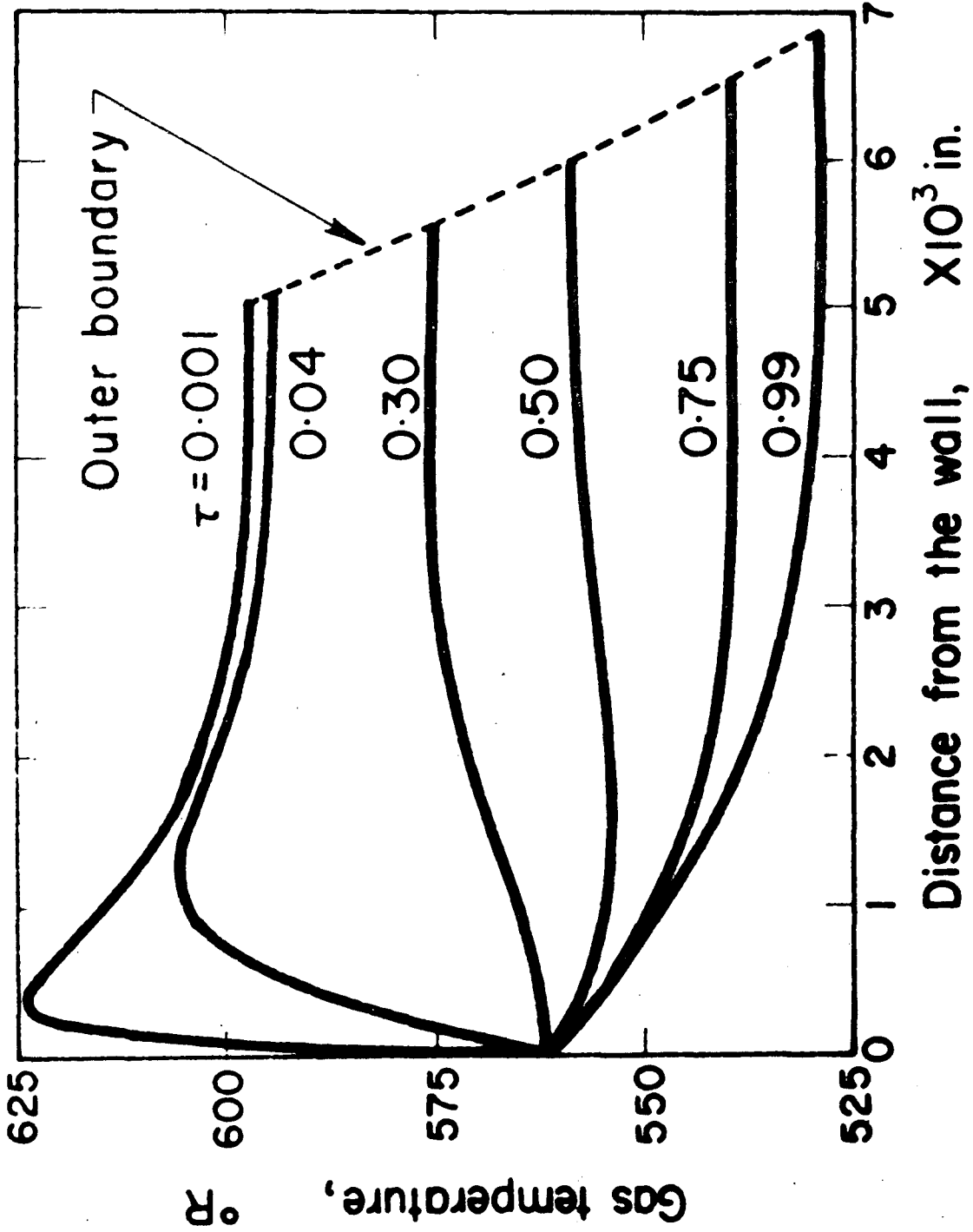


Figure 32. Predicted gas temperature profiles for the PST. Shock arrives at normalized time, $\tau = 0$.

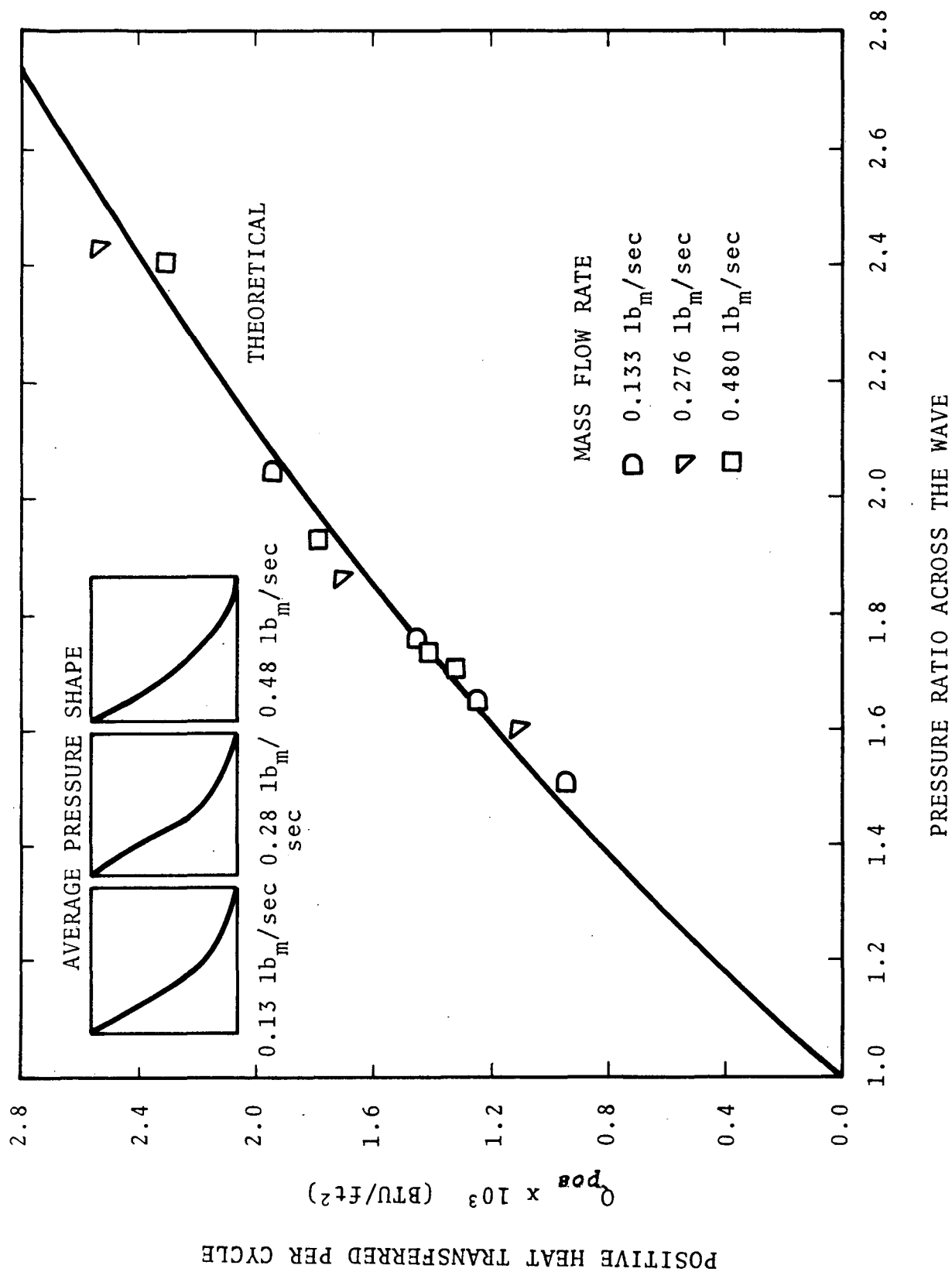


Figure 33. Positive heat transferred per cycle at three different tube mass flow rates of the PST. Frequency = 479 Hz; tube pressure = 188 psia.

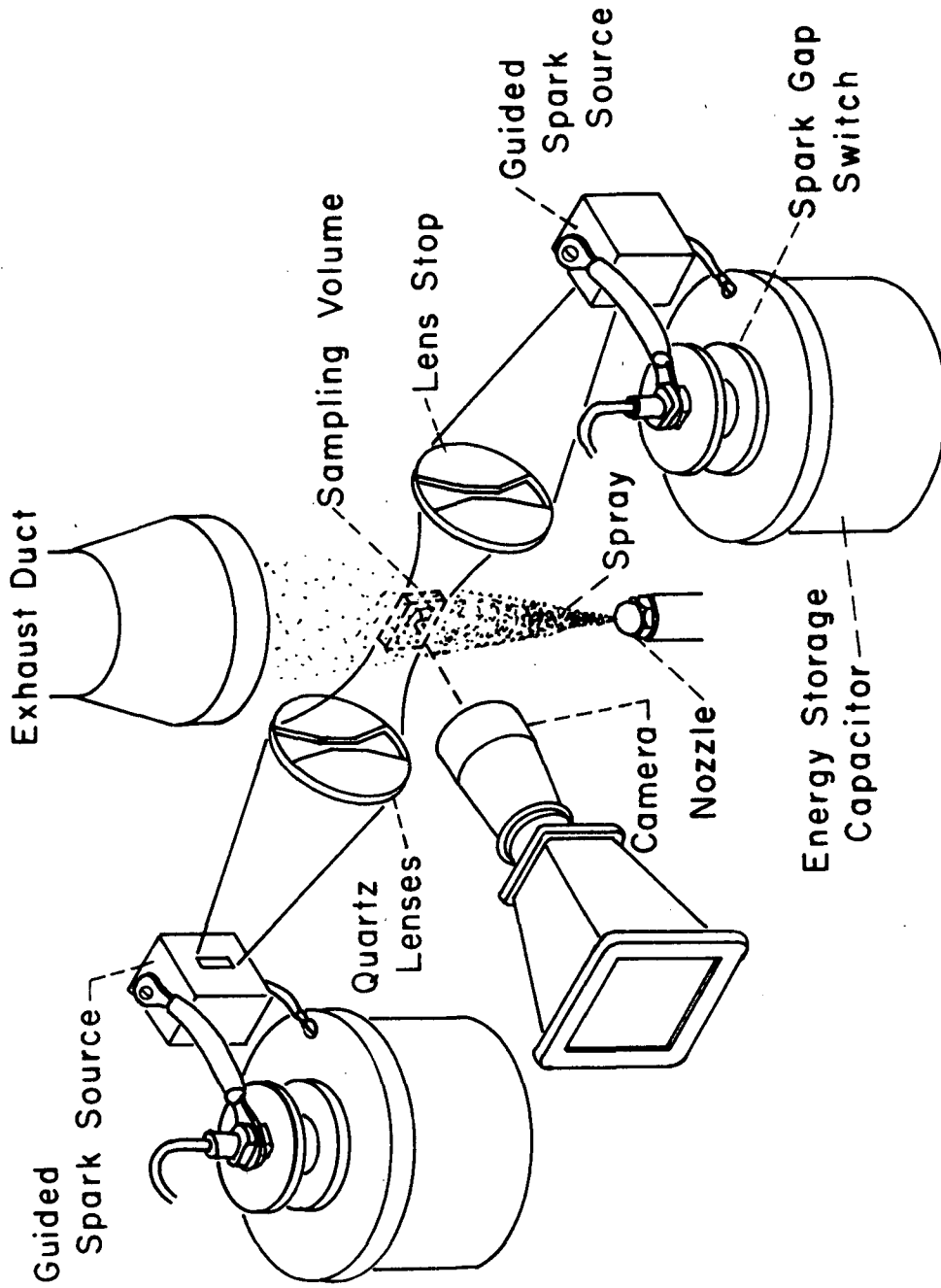
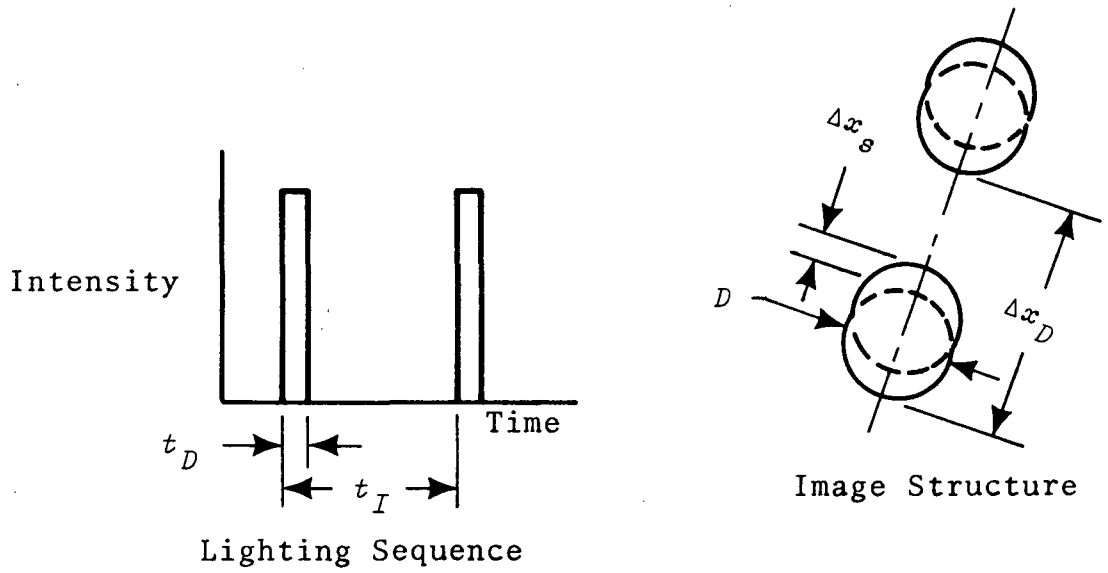


Figure 34. Experimental arrangement for double-exposure fluorescent photography.



Time Interval	Chosen such that:	Limiting value determined by:
Flash duration t_D	$\Delta x_s / D < 0.1$ drop moves less than 0.1 of its diameter	Smallest drops with highest velocities
Flash interval t_I	$\Delta x_D / D > 1$ images of the same drop do not overlap	Largest drops with lowest velocities

Figure 35. Ideal timing criteria for double exposure photography.

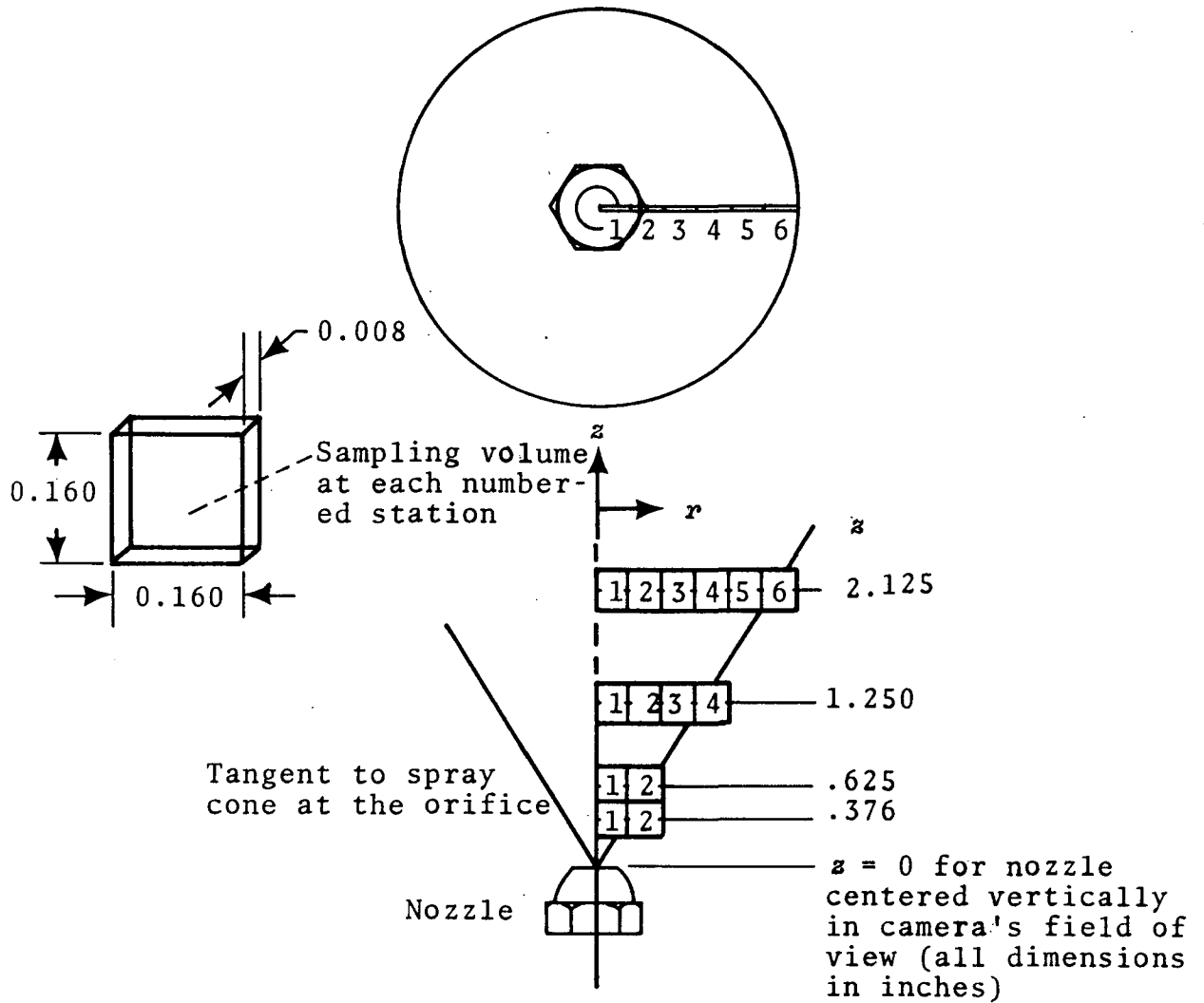
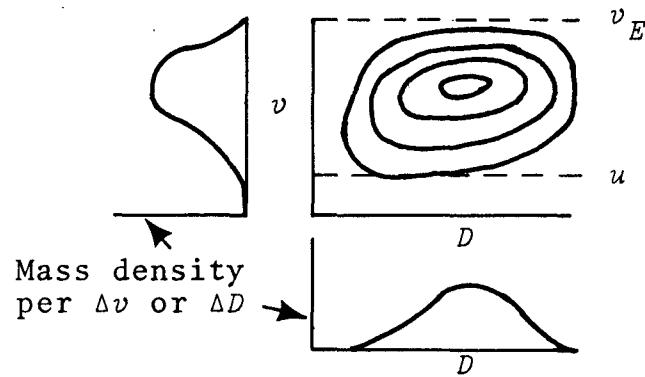


Figure 36. Sampling geometry for spray photography.

Stage of spray development

Contours of
droplet mass density
(Δv) (ΔD)

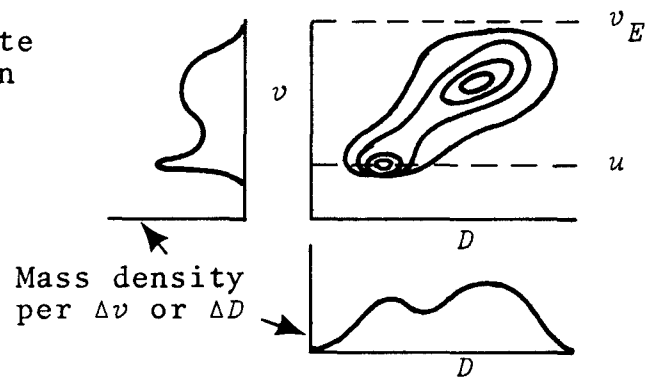
Formation



$$(v|D) \approx \text{constant} = v_0$$

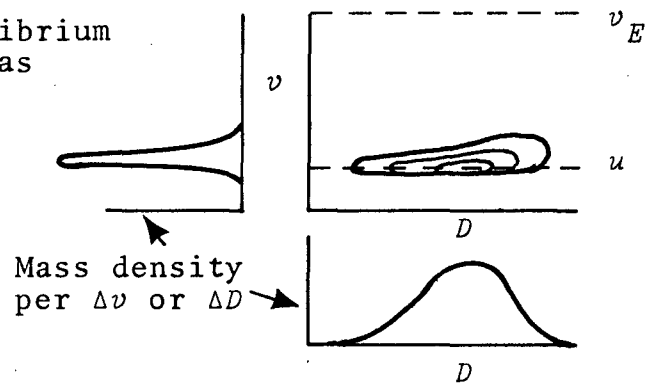
$$f_F \approx v_0 f_S$$

Intermediate propagation



$$f_F = (v|D) f_S$$

Near equilibrium with the gas



$$(v|D) \approx u$$

$$f_F \approx u f_S$$

Figure 37. Schematic formation-propagation characteristics of mass density functions with no vaporization. Injection into a lower velocity gas, $v_E > u$.

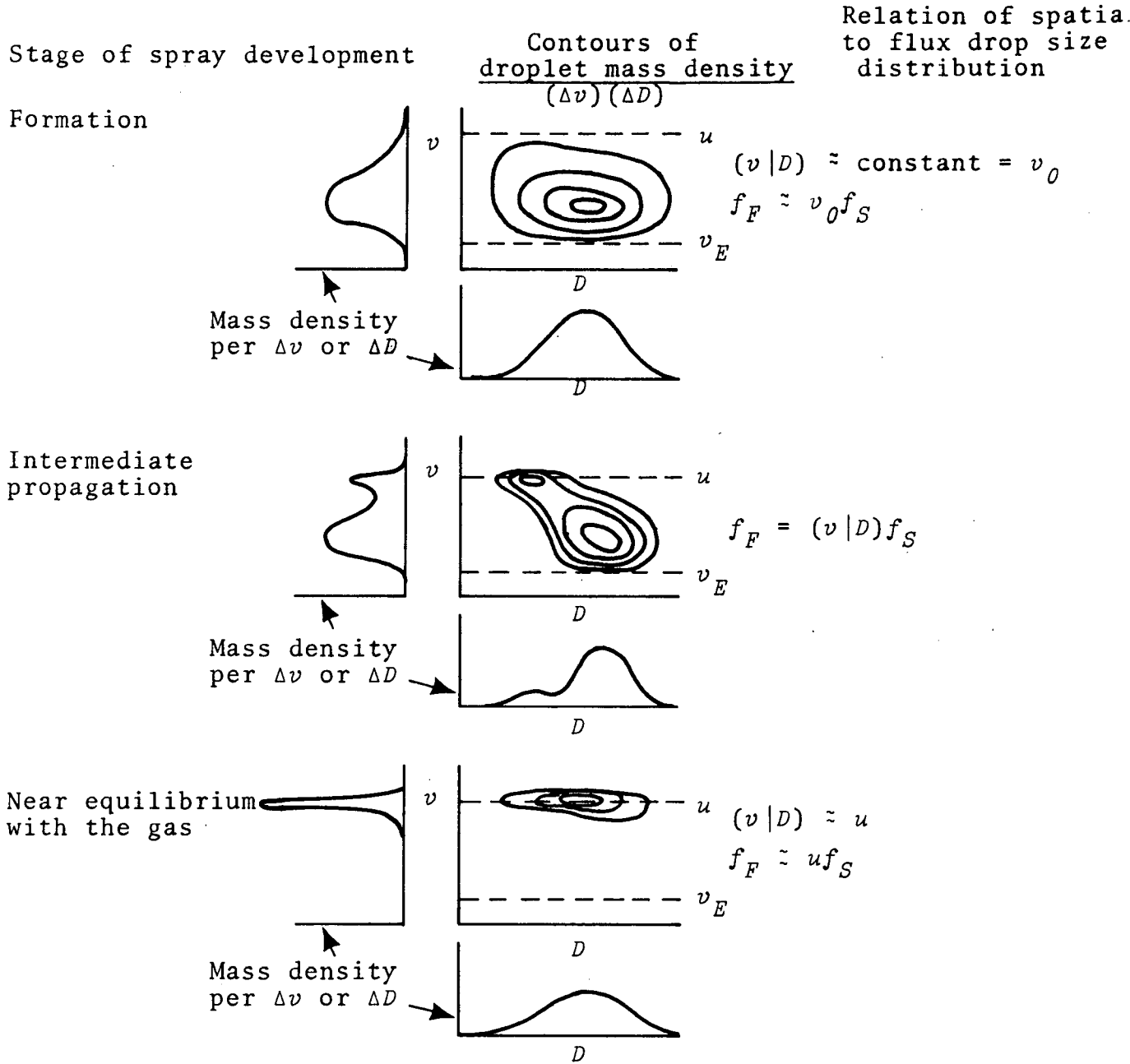


Figure 38. Schematic formation-propagation characteristics of mass density functions with no vaporization. (Injection into a higher velocity gas, $v_E < u$.)

DISTRIBUTION LIST

Dr. R. J. Priem MS 500-209
NASA Lewis Research Center
21000 Brookpark Road
Cleveland, Ohio

Norman T. Musial
NASA Lewis Research Center
21000 Brookpark Road
Cleveland, Ohio 44135

Library (2)
NASA Lewis Research Center
21000 Brookpark Road
Cleveland, Ohio 44135

Brooklyn Polytechnic Institute
Attn: V. D. Agosta
Long Island Graduate Center
Route 110
Farmingdale, New York 11735

Chemical Propulsion Information Agency
Johns Hopkins University/APL
Attn: T. W. Christian
8621 Georgia Avenue
Silver Spring, Maryland 20910

NASA
Lewis Research Center
Attn: E. W. Conrad, MS 500-204
21000 Brookpark Road
Cleveland, Ohio 44135
North American Rockwell Corporation
Rocketdyne Division
Attn: L. P. Combs, D/991-350
Zone 11
6633 Canoga Avenue
Canoga Park, California 91304

National Technical Information Service
Springfield, Virginia 22151
(40 copies)

NASA Representative
NASA Scientific and Technical
Information Facility
P. O. Box 33
College Park, Maryland 20740
(2 copies with Document Release
Authorization Form)

Aerospace Corporation
Attn: O. W. Dykema
Post Office Box 95085
Los Angeles, California 90045

Ohio State University
Department of Aeronautical and Astronautical
Engineering
Attn: R. Edse
Columbus, Ohio 43210

TRW Systems
Attn: G. W. ELverum
One Space Park
Redondo Beach, California 90278

Bell Aerospace Company
Attn: T. F. Ferger
Post Office Box 1
Mail Zone J-81
Buffalo, New York 14205

Pratt & Whitney Aircraft
Florida Research & Development Center
Attn: G. D. Garrison
Post Office Box 710
West Palm Beach, Florida 33402

NASA
Lewis Research Center
Attn: L. Gordon, MS 500-209
21000 Brookpark Road
Cleveland, Ohio 44135

Purdue University
School of Mechanical Engineering
Attn: R. Goulard
Lafayette, Indiana 47907

Air Force Office of Scientific Research
Chief Propulsion Division
Attn: Lt. Col. R. W. Haffner (NAE)
1400 Wilson Boulevard
Arlington, Virginia 22209

Pennsylvania State University
Mechanical Engineering Department
Attn: G. M. Faeth
207 Mechanical Engineering Building
University Park, Pennsylvania 16802

University of Illinois
Aeronautics/Astronautic Engineering Department
Attn: R. A. Strehlow
Transportation Building, Room 101
Urbana, Illinois 61801

NASA
Manned Spacecraft Center
Attn: J. G. Thibadaux
Houston, Texas 77058

Massachusetts Institute of Technology
Department of Mechanical Engineering
Attn: T. Y. Toong
77 Massachusetts Avenue
Cambridge, Massachusetts 02139

Illinois Institute of Technology
Attn: T. P. Torda
Room 200 M. H.
3300 S. Federal Street
Chicago, Illinois 60616

AFRPL
Attn: R. R. Weiss
Edwards, California 93523

U. S. Army Missile Command
AMSMI-RKL, Attn: W. W. Wharton
Redstone Arsenal, Alabama 35808

University of California
Aerospace Engineering Department
Attn: F. A. Williams
Post Office Box 109
LaJolla, California 92037

Georgia Institute of Technology
Aerospace School
Attn: B. T. Zinn
Atlanta, Georgia 30332

Marshall Industries
Dynamic Science Division
2400 Michelson Drive
Irvine, California 92664

Mr. Donald H. Dahlene
U. S. Army Missile Command
Research, Development, Engineering and Missile Systems Laboratory
Attn: AMSMI-RK
Redstone Arsenal, Alabama 35809

TISIA
Defense Documentation Center
Cameron Station
Building 5
5010 Duke Street
Alexandria, Virginia 22314

Office of Assistant Director
(Chemical Technician)
Office of the Director of Defense Research and Engineering
Washington, D. C. 20301

D. E. Mock
Advanced Research Projects Agency
Washington, D. C. 20525

Dr. H. K. Doetsch
Arnold Engineering Development Center
Air Force Systems Command
Tullahoma, Tennessee 37389

Library
Air Force Rocket Propulsion Laboratory (RPR)
Edwards, California 93523

Library
Bureau of Naval Weapons
Department of the Navy
Washington, D. C.

Library
Director (Code 6180)
U. S. Naval Research Laboratory
Washington, D. C. 20390

APRP (Library)
Air Force Aero Propulsion Laboratory
Research and Technology Division
Air Force Systems Command
United States Air Force
Wright-Patterson AFB, Ohio 45433

Technical Information Department
Aeronutronic Division of Philco Ford Corporation
Ford Road
Newport Beach, California 92663

Library-Documents
Aerospace Corporation
2400 E. El Segundo Boulevard
Los Angeles, California 90045

Princeton University
James Forrestal Campus Library
Attn: D. Harrje
Post Office Box 710
Princeton, New Jersey 08540

U. S. Naval Weapons Center
Attn: T. Inouye, Code 4581
China Lake, California 93555

Office of Naval Research
Navy Department
Attn: R. D. Jackel, 473
Washington, D. C. 20360

Air Force Aero Propulsion Laboratory
Attn: APTC Lt. M. Johnson
Wright Patterson AFB, Ohio 45433

Naval Underwater Systems Center
Energy Conversion Department
Attn: Dr. R. S. Lazar, Code TB 131
Newport, Rhode Island 02840

NASA
Langley Research Center
Attn: R. S. Levine, MS 213
Hampton, Virginia 23365

Aerojet General Corporation
Attn: David A. Fairchild, Mech. Design
Post Office Box 15847 (Sect. 9732)
Sacramento, California 95809

Colorado State University
Mechanical Engineering Department
Attn: C. E. Mitchell
Fort Collins, Colorado 80521

North American Rockwell Corporation
Rocketdyne Division
Attn: J. A. Nestlerode,
AC46 D/596-121
6633 Canoga Avenue
Canoga Park, California 91304

University of Michigan
Aerospace Engineering
Attn: J. A. Nicholls
Ann Arbor, Michigan 48104

Tulane University
Attn: J. C. O'Hara
6823 St. Charles Avenue
New Orleans, Louisiana 70118

University of California
Department of Chemical Engineering
Attn: A. K. Oppenheim
6161 Etcheverry Hall
Berkeley, California 94720

Army Ballistics Laboratories
Attn: J. R. Osborn
Aberdeen Proving Ground, Maryland 21005

Sacramento State College
School of Engineering
Attn: F. H. Reardon
6000 J. Street
Sacramento, California 95819

Purdue University
School of Mechanical Engineering
Attn: B. Z. Reese
Lafayette, Indiana 47907

NASA
George C. Marshall Space Flight Center
Attn: R. J. Richmond, SNE-ASTN-PP
Huntsville, Alabama 35812

Jet Propulsion Laboratory
California Institute of Technology
Attn: J. H. Rupe
4800 Oak Grove Drive
Pasadena, California 91103

University of California
Mechanical Engineering Thermal Systems
Attn: Prof. R. Sawyer
Berkeley, California 94720

ARL (ARC)
Attn: K. Scheller
Wright Patterson AFB, Ohio 45433

Library
Bell Aerosystems, Inc.
Box 1
Buffalo, New York 14205

Report Library, Room 6A
Battelle Memorial Institute
505 King Avenue
Columbus, Ohio 43201

D. Suichu
General Electric Company
Flight Propulsion Laboratory Department
Cincinnati, Ohio 45215

Library
Ling-Temco-Vought Corporation
Post Office Box 5907
Dallas, Texas 75222

Marquardt Corporation
16555 Saticoy Street
Box 2013 - South Annex
Van Nuys, California 91409

P. F. Winternitz
New York University
University Heights
New York, New York

R. Stiff
Propulsion Division
Aerojet-General Corporation
Post Office Box 15847
Sacramento, California 95803

Library, Department 596-306
Rocketdyne Division of Rockwell
North American Rockwell Inc.
6633 Canoga Avenue
Canoga Park, California 91304

Library
Stanford Research Institute
333 Ravenswood Avenue
Menlo Park, California 94025

Library
Susquehanna Corporation
Atlantic Research Division
Shirley Highway and Edsall Road
Alexandria, Virginia 22314

STL Tech. Lib. Doc. Acquisitions
TRW System Group
1 Space Park
Redondo Beach, California 90278

Dr. David Altman
United Aircraft Corporation
United Technology Center
Post Office Box 358
Sunnyvale, California 94088

Library
United Aircraft Corporation
Pratt and Whitney Division
Florida Research and Development Center
Post Office Box 2691
West Palm Beach, Florida 33402

Library
Air Force Rocket Propulsion Laboratory (RPM)
Edwards, California 93523

Allan Hribar, Assistant Professor
Post Office Box 5014
Tennessee Technological University
Cookeville, Tennessee 38501

NASA
Lewis Research Center
Attn: E. O. Bourke MS 500-209
21000 Brookpark Road
Cleveland, Ohio 44135

NASA
Lewis Research Center
Attn: D. L. Nored 500-203
21000 Brookpark Road
Cleveland, Ohio 44135

NASA
Lewis Research Center MS 500-313
Rockets & Spacecraft Procurement Section
21000 Brookpark Road
Cleveland, Ohio 44135

Paul Weiber MS-6-1
NASA
Lewis Research Center
2100 Brookpark Road
Cleveland, Ohio 44135

Lee D. Alexander
2712 Southern Avenue
Baltimore, Maryland 21214

R. W. Goluba
Lawrence Radiation Labs
P.O. Box 808
Livermore, California 94550

John Groeneweg
Lewis Research Center
NASA
21000 Brookpark Road
Cleveland, Ohio 44135

Jaime A. Ricart
%Central Romana By-Products Co.
LaRomana
Dominican Republic

Daniel Wendland
Propulsion Research Unit
Propulsion/Mechanical Staff
MS 27-51
The Boeing Co.
Seattle, Washington

Richard Sowls
Mechanical Engineering Department
The University of Wisconsin
Madison, Wisconsin

C. W. Savery
Mechanical Engineering Dept.
Drexel University
Philadelphia, Pa.

D. L. Juedes
Esso Research & Engineering Co.
P.O. Box 101
Florham Park, New Jersey

Dr. Jose A. Manrique
Department of Thermal Engineering
Instituto Tecnológico Y De Estudios
Superiores De Monterrey
Sucursal de Correos "J"
Monterrey, N. L.
Mexico